Design and Realization of ALD Grown Al_2O_3 Waveguides for Applications in Silicon Based Photonics

Mustafa DEMİRTAŞ

Master of Science Thesis

Electrical and Electronics Engineering Program

August 2014

ANADOLU ÜNİVERSİTESİ

JÜRİ VE ENSTİTÜ ONAYI

Mustafa Demirtaş'ın "Design and Realization of ALD Grown Al_2O_3 Waveguides for Applications in Silicon Based Photonics" başlıklı **Elektrik ve Elektronik Mühendisliği** Anabilim Dalındaki, Yüksek Lisans Tezi 27.08.2014 tarihinde, aşağıdaki jüri tarafından Anadolu Üniversitesi Lisansüstü Eğitim-Öğretim ve Sınav Yönetmeliğinin ilgili maddeleri uyarınca değerlendirilerek kabul edilmiştir.

		Adı Soyadı	İmza
Üye (Tez Danışmanı)	**:**	**Doç. Dr. Feridun AY**	**…………..**
Üye	**:**	**Doç. Dr. Cem SEVİK**	**…………..**
Üye	**:**	**Yrd. Doç. Dr. Nihan KOSKU PERKGÖZ**	**…………..**

Anadolu Üniversitesi Fen Bilimleri Enstitüsü Yönetim Kurulu'nun …………….. tarih ve …………….. sayılı kararıyla onaylanmıştır.

Enstitü Müdürü

ANADOLU ÜNİVERSİTESİ

ÖZET

Yüksek Lisans Tezi

SİLİKON TABANLI FOTONİK UYGULAMALARINDA ALD İLE BÜYÜTÜLMÜŞ Al_2O_3 DALGA KILAVUZLARININ TASARIM VE GERÇEKLEMESİ

Mustafa DEMİRTAŞ
Anadolu Üniversitesi
Fen Bilimleri Enstitüsü
Elektrik ve Elektronik Mühendisliği Anabilim Dalı

Danışman: Doç. Dr. Feridun AY

2014, 105 Sayfa

Bu tezde silisyum tabanlı fotonik uygulamalarında Atomik Katman Kaplama (AKK-ALD) ile büyütülmüş Al_2O_3 dalga kılavuzlarının tasarım ve gerçeklemesi ele alınmıştır. Al_2O_3 büyütme işlemi ALD kullanılarak yapılmıştır. Farklı büyütme koşulları incelenerek aktif ve pasif dalga kılavuzlarının silikon temelli fotonik uygulamalarındaki en uygun büyütme koşulları belirlenmiştir. Büyütülen örneklerin ellipsometre ile kalınlıkları ve kırılma indisleri ölçülmüştür. X-ışını Kırınımı (XRD) yöntemi kullanılarak amorf yapıya sahip olduğu ortaya konulmuştur. Buna ek olarak, Mikro-Raman Spektroskopisi ve Fourier Dönüşüm Kızılötesi Spektroskopisi (FTIR) kullanılarak katmanlar içerisindeki maddelerin ve bağ yapıları belirlenmiştir. X-ışını Fotoelektron Spektroskopisi (XPS) kullanılarak yapı içerisinde yer alan elementlerin yüzde oranlarını belirlenmiştir. Karakterizasyon işlemlerinden sonra, polarizasyondan bağımsız tek modu destekleyen Al_2O_3 temelli çatı tip optik dalga kılavuzunun tasarım işlemi yapılmıştır. Son olarak, Al_2O_3 temelli düzlemsel dalga kılavuzu kullanarak optik kayıplar hakkında bir fikir edinilmiştir.

Anahtar Kelimeler: Dalga Kılavuzları, amorf Al_2O_3, tümleşik optik, fotonik, karakterizasyon, XRD, FTIR, XPS, Mikro-Raman, optik kayıp

ANADOLU ÜNİVERSİTESİ

ABSTRACT

Master of Science Thesis

DESIGN AND REALIZATION OF ALD GROWN AL_2O_3 WAVEGUIDES FOR APPLICATIONS IN SILICON BASED PHOTONICS

Mustafa DEMİRTAŞ

Anadolu University
Graduate School of Sciences
Electrical and Electronics Engineering Program

Supervisor: Assoc. Prof. Dr. Feridun AY
2014, 105 pages

In this thesis, design and realization of Atomic Layer Deposition (ALD) grown Al_2O_3 waveguides application in silicon based photonics has been considered. Al_2O_3 was grown using ALD technique. Different samples were grown using different growth recipes and optimal growth parameters were determined for active and passive optical waveguides. Ellipsometer was used to determine of sample thicknesses and refractive index. X-ray Diffraction (XRD) was used in order to confirm the amorphous structure of the grown samples. Moreover, complementary approach to determine the bond structures in the layers was implemented using both Micro-Raman and Fourier Transform Infrared Spectroscopy (FTIR). X-ray Photoelectron Spectroscopy (XPS) was used to determine the percentages of constituting elements in the Al_2O_3 layers. After the characterization process, ridge type single mode polarization independent optical waveguides were designed using beam propagation method. Finally, Al_2O_3-based planar waveguide was realized and optical propagation had been demonstrated.

Keywords: Optical waveguides, amorphous Al_2O_3, integrated optics, photonics, XRD, FTIR, XPS, Micro-Raman, optical loss.

ANADOLU ÜNİVERSİTESİ

ACKNOWLEDGEMENTS

First and foremost I would like to thank my supervisor Assoc. Prof. Dr. Feridun Ay for providing me with the opportunity to study in this field and complete my Master of Science work. I am extremely grateful for many discussions which helped guided me in the right direction, his motivating attitude, his availability as a supervisor and his many insightful suggestions. I would also like to thank Ayberk for his help and encouragement.

I would also like to thank Gonca, Aydınlı and Kocabaş Research Group members for their help.

Most importantly I would also like to thank my family for their encouragement and support.

Last but not the least, I would also like to thank Gökben for her love that has been invaluable for me.

Mustafa Demirtaş
August 2014

ANADOLU ÜNİVERSİTESİ

TABLE OF CONTENTS

ÖZET i
ABSTRACT ii
ACKNOWLEDGEMENTS iii
TABLE OF CONTENTS iv
LIST OF FIGURES vii
LIST OF TABLES xi
1. INTRODUCTION 1
1.1. Integrated Optics 1
1.2. Waveguides, Signal Amplification and Optical Losses 2
1.2.1. Polymer-based Optical Waveguides 3
1.2.2. Semiconductor Optical Waveguides 4
1.2.3. Dielectric Optical Waveguides 6
1.3. Rare Earth Doped Optical Waveguides 7
1.3.1. Erbium Doped Optical Amplifiers 8
1.3.2. Erbium Doping and Host Materials 8
1.3.3. Optical Amplifiers based on $Al_2O_3:Er^{3+}$ 11
1.4. Contribution of this thesis 11

2. THIN FILM GROWTH TECNIQUES 13
2.1. DC/RF Sputtering 13
2.2. E-beam Evaporation 14
2.3. Pulsed Laser Deposition 15
2.4. Molecular Beam Epitaxy 16
2.5. Chemical Vapor Deposition 17
2.6. Atomic Layer Deposition (ALD) 19
2.7. Overall Comparison of Thin Film Growth Techniques 21

3. FABRICATION AND CHARACTERIZATION OF AL_2O_3 LAYERS 24
3.1. ALD Growth of Al_2O_3 Layers 24
3.1.1. ALD Growth Parameters 24
3.1.2. Deposition Procedure and Growth Matrix 26

ANADOLU ÜNİVERSİTESİ

3.1.3. Wafer preparation 27
3.2. Spectroscopic Ellipsometer Measurement 27
3.2.1. The effect of temperature on Al_2O_3 layers 31
3.2.2. The effect of purge time on Al_2O_3 layers 33
3.3. X-Ray Diffraction Measurement (XRD) 36
3.3.1. Basic Concepts 37
3.3.2. XRD Results 38
3.4. Micro-Raman Investigation 39
3.4.1. Basic Theory of Raman Spectroscopy 39
3.4.2. Micro-Raman System Hardware 40
3.4.3. Experimental Results 42
3.5. Fourier Transform Infrared Spectroscopy (FTIR) 49
3.5.1. Background Theory and Molecular Vibrations 49
3.5.2. Hardware Setup 52
3.5.3. Experimental Results 53
3.6. X-Ray Photoelectron Spectroscopy Results (XPS) 62
3.6.1. Basic Theory 62
3.6.2. Experimental Setup and Method 63
3.6.3. Experimental Results and Discussion 64

4. POLARIZATION INSENSITIVE SINGLE MODE AL_2O_3 RIB/RIDGE WAVEGUIDE DESIGN 67
4.1. Simulation Structure and Parameters 67
4.2. Simulation Results 69
4.2.1. a-Al_2O_3 Slab Waveguide 69
4.2.2. Mode Analysis of Rib/Ridge Waveguide 70
4.2.3. Mode Size of Rib/Ridge Waveguide 78
4.2.4. Rib/Ridge Waveguide Birefringence 82
4.3. Discussion 84

5. OPTICAL LOSS CHARACTERIZATION 85
5.1. Method and Experimental Setup 85
5.2. Linear Response Test of CMOS Camera 87

ANADOLU ÜNİVERSİTESİ

5.3. Results 89

6. CONCLUSION **92**

6.1. Future Prospects and Suggestion 93

REFERENCES **94**

ANADOLU ÜNİVERSİTESİ

LIST OF FIGURES

Figure 1.1 Comparative chronological development of Electronics and Photonics Technology [1] 1
Figure 1.2 Use of polymer-based optical waveguides in optical communication [9] 3
Figure 1.3 Energy level diagram of the Er^{3+} ion, and some common transitions [46] 9
Figure 2.1 Basic schematic of DC and RF sputtering systems [84] 14
Figure 2.2 Schematic diagram of the electron beam evaporation process [80] 14
Figure 2.3 Schematic diagram of the pulsed electron deposition process [87] 16
Figure 2.4 Simplified schematic of an MBE 17
Figure 2.5 Basic growth procedure of CVD. 18
Figure 2.6 Schematic diagram of the ALD reactor 19
Figure 2.7 Material based schematic representation of per cycle of ALD [100] 21
Figure 3.1 Schematic illustration of Savannah-100 ALD system [111] 25
Figure 3.2 Geometry of Ellipsometric Measurement [113] 28
Figure 3.3 Measurement Procedure of Spectroscopic Ellipsometer 29
Figure 3.4 The effect of growth temperature on growth rate 31
Figure 3.5 The effect of the growth temperature on the refractive index of Al_2O_3 at λ=1550 nm 32
Figure 3.6 Refractive Index vs.Wavelength of different temp. growth 33
Figure 3.7 Refractive Index vs. Wavelength of Sample 1&2 34
Figure 3.8 Refractive Index vs. Wavelength of Sample 7&8 35
Figure 3.9 Refractive Index vs. Wavelength of Sample 1&8 36
Figure 3.10 Schematic illustration of Bragg's law 37
Figure 3.11 XRD pattern of selected samples 39
Figure 3.12 Diagram of the Raman and Rayleigh scattering processes 40
Figure 3.13 Typical Components of a micro-Raman System 41
Figure 3.14 Schematic representation of Micro-Raman spectrometer [125] 42

ANADOLU ÜNİVERSİTESİ

Figure 3.15 Micro Raman results of selected samples 43
Figure 3.16 Micro-Raman results of Al_2O_3 layers and fitted peaks of Sample 1 45
Figure 3.17 Micro-Raman results of Al_2O_3 layers and fitted peaks of Sample 5 46
Figure 3.18 Micro-Raman results of Al_2O_3 layers and fitted peaks of Sample 7 47
Figure 3.19 Schematics of major vibrational types [141] 50
Figure 3.20 Illustration of norma modes for (a) nonlinear and (b) linear polyatomic molecule [141] 51
Figure 3.21 Schematic of FTIR setup with Michelson interferometer 52
Figure 3.22 FTIR absorbance results of 300 ºC with purge time of 4 seconds (Sample 1), 200 ºC with purge time of 4 seconds (Sample 5) and 150 ºC with purge time of 4 seconds (Sample 7) 54
Figure 3.23 FTIR absorbance results of Al_2O_3 layers and fitted peaks of Sample 1 56
Figure 3.24 FTIR absorbance results of Al_2O_3 layers and fitted peaks of Sample 5 57
Figure 3.25 FTIR absorbance results of Al_2O_3 layers and fitted peaks of Sample 7 58
Figure 3.26 The integrated area of O-H (strecthing) vibration of selected samples 59
Figure 3.27 The integrated area of Al-O vibrations common to selected samples 60
Figure 3.28 Basic Diagram of typical photoelectron instrument used in XPS . 62
Figure 3.29 Al 2p peak position of Sample 7 for surface and after 10 seconds etching 64
Figure 3.30 The atomic concentration variation of O, Al, and Si as a function of etch time for three samples grown at 300 ºC with 4 seconds purge time, 200 ºC with 4 seconds purge time and 150 ºC with 4 seconds purge time. 66

ANADOLU ÜNİVERSİTESİ

Figure 4.1 Simulated rib waveguide on SiO_2 substrate. D, W and SH represents etch depth, waveguide width and slab height, respectively. 68

Figure 4.2 Change of effective index (n_{eff}) with respect to slab height of the waveguide at λ = 1.48 μm Fundamental and higher order modes were represented by open and filled circles, respectively. Red indicates TE polarization, and blue represents TM polarization. Dashed line indicates effective index value equal to substrate's (SiO_2) refractive index. 70

Figure 4.3 Mode regions for the third optical communication window at a) λ=1.48 μm b) λ=1.53 μm c) λ=1.55 μm d) λ=1.61 μm . DgfhfghfhgfgS.Z.M. in the legends is acronym for "Single Mode Zone" 74

Figure 4.4 (a) Single mode region at different polarization and wavelengths as λ=1.48, 1.55 and sdfsdfsdfsdfs 1.61 μm (b) Gray filled area demonstrates the region where indicated wavelengths are sdfsdfsdfsfgfgsingle mode without any polarization dependence. Solid lines are to guide the eye. 77

Figure 4.5 Selected width and etch depth dimensions for mode size investigation at 1.55 μm 78

Figure 4.6 Mode areas of the wavelength of 1.55 μm as a function of rib geometries a) TE polarization b) TM polarization 80

Figure 4.7 Single mode confinement of the rib waveguide with respect to W and D at λ=1.55 μm. a) Confinement factor for different geometries, b) TE mode field profile at W=3 μm D=0.2 μm, c) TE mode field profile at W=4 μm and D=0.45 μm, d) TM mode field profile at same dimension with c 81

Figure 4.8 Δn_{eff} and Δn_g calculated for the shaded area in Figure 4.4 as a function of etch depth. 83

Figure 5.1 $Si/SiO_2/Al_2O_3$ planar waveguide cut off analysis for different polarization 85

Figure 5.2 Schematic mechanism of Waveguide loss measurement setup 86

ANADOLU ÜNİVERSİTESİ

Figure 5.3 A photograph of experimental waveguide loss measurement setup.. 87
Figure 5.4 Different filter responses of CMOS camera (a) filter 0 (no filter), (b) filter 1 (c) filter 2 (d) filter 3 88
Figure 5.5 The comparison of normalized optic power and camera response for different filters 89
Figure 5.6 The captured image from CMOS camera of highly multimode planar waveguide.. 90

ANADOLU ÜNİVERSİTESİ

LIST OF TABLES

Table 1.1 Optical properties of selected polymer-based optical waveguides .. 4
Table 1.2 Optical properties of selected semiconductor crystalline-based optical waveguides 5
Table 1.3 Optical properties of selected amorphous dielectric optical waveguides 6
Table 1.4 Luminescence wavelengths of all rare-earth ions [41] 8
Table 2.1 Comparison of different CVD reactors 18
Table 2.2 Comparison of growth methods [101] 22
Table 3.1 Growth-Parameter Matrix 26
Table 3.2 Cauchy Equation's Coefficients of samples 30
Table 3.3 The film thicknesses and growth rates of samples 30
Table 3.4 M/NA for different objectives 41
Table 3.5 Raman vibrations observed in the grown Al_2O_3 44
Table 3.6 Fitting results of selected samples 48
Table 3.7 The degrees of freedom for polyatomic nonlinear and linear molecules [141] 50
Table 3.8 FTIR absorbance vibrations observed in the selected samples...... 55
Table 3.9 Fitting results of selected samples 61
Table 3.10 Detailed acquisition parameters 63
Table 3.11 Stoichiometry of Al_2O_3 for selected samples 65
Table 4.1 Combination of mode profiles of TE and TM polarizations designate nine different regions that demonstrate "character" of the waveguide of which two of them (number 2 and 3) are technologically important. Please note that region number 3 in bold is the single mode region for both polarizations. 72

ANADOLU ÜNİVERSİTESİ

1. INTRODUCTION

1.1. Integrated Optics

It is now approximately 45 years since the name “integrated optics” was first used [1]. Today, the research field of integrated optics has become a major topic of interest for research activities in both industry and university laboratories [1]. In addition, a new study reports that the European optics sector grew by 12% in 2006, and predicts that the world photonics market will grow by 7.6% annually to 2014 [2]. The global photonics market was around 350 billion euros in 2011 compared with 228 billion euros for 2005, it is and predicted that the global photonics market will increase to about 615 billion euros by 2020 [2].

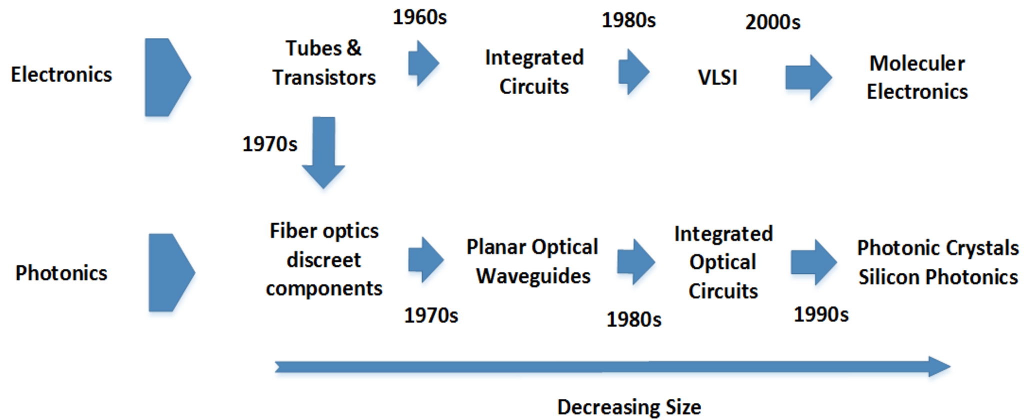

Figure 1.1 Comparative chronological development of Electronics and Photonics Technology [1]

Comparative chronological development of both electronics and photonics technology is illustrated in Figure 1.1. In 1970s, photonics and electronics technologies were separated and have continued to evolve in parallel. Moreover, it is clear that device size of both technologies has continued to decrease over the years. In integrated optics the fundamental elements can be viewed as optical beams (signals) transmitted and routed in waveguides with thicknesses ranging from nanometers up to bulk sizes, similar to signal transmission and processing in electrical circuits [1]. Two significant improvements have guided the integrated optics. First, rapid progress of laser sources. Second, the improvement and widespread use of optical fiber for information transmission [3]. Therefore, we witness a trend in which wire and radio links are replaced by light wave-guiding

ANADOLU ÜNİVERSİTESİ

optical fibers and electrical integrated circuits are replaced by miniaturized optical integrated circuits (OIC).

OIC have many advantages. Some of the advantages are increased bandwidth, reduced size and weight, low loss signal and high speed signal transmission [3]. The most important configuration parameters of OIC systems are design, mechanism, material type and functionality. The material used for realization of an integrated optical device is of utmost importance. Low material absorption ensures a potentially improved device performance [4].

Fundamental components of OIC systems are source, detector and waveguide. These components can all be integrated on a single substrate (GaAs, InP, etc.), in which case it is called a monolithic OIC. When all or some of the components are made of different materials, it is called as a hybrid OIC. According to the functionality optical circuits can be divided into two categories, passive or active. Passive devices are used for guiding and directing the light. Active devices are used for emitting or amplifying light or converting light energy into electrical energy, or vice versa [3].

1.2. Waveguides, Signal Amplification and Optical Losses

The basic component of any optical circuit is the optical waveguide which permits connecting different devices optically, just as a metallic strip does in an electrical integrated circuits. To build integrated optical circuits that substitute micro-electronic circuits, integrated optical waveguides with light confinement with size of the order of the wavelength is compulsory [5].

An optical signal will be degraded by attenuation and dispersion while it propagates through a material. Attenuation of an optical signal is called as optical loss. Dispersion depends on the device structure and it can be reduced by using appropriate design. On the other hand, attenuation which raises from several different physical effects leads to a signal loss [6]. Optical losses are usually measured in units of decibel per length of medium (dB/cm, dB/km, etc.).

Therefore, low loss optical waveguides need to be developed to make the amplification process the signal as efficient as possible. In a functional optical amplifier device, the signal amplification must be more than the optical losses. This difference between signal amplification and optical losses, is referred to as optical

ANADOLU ÜNİVERSİTESİ

gain. Different material types are used to provide optical gain in optical waveguides such as polymers, crystalline or amorphous materials [7].

1.2.1. Polymer-based Optical Waveguides

Polymer optical waveguides are being investigated owing to their ease of fabrication and low cost. [8]. Figure 1.2 summarizes use of polymer waveguides in optical communication.

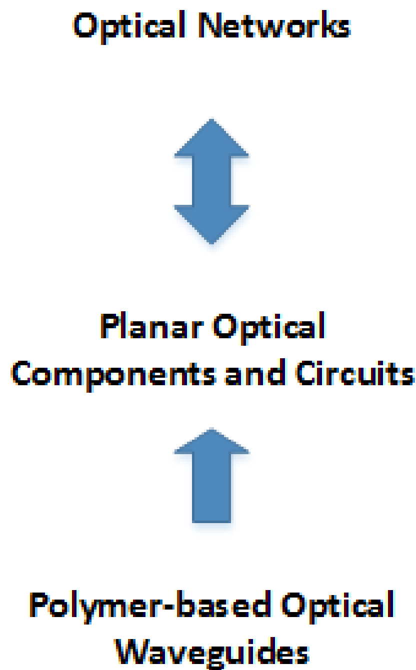

Figure 1.2 Use of polymer-based optical waveguides in optical communication [9]

Planar optical components and circuits play key role in rapidly developing optical networks. One of important planar optical components is planar polymer-based optical waveguides due to their easier processibility and integration over inorganic counterparts. Important optical parameters of selected polymer-based optical waveguide components are summarized in Table 1.1.

In Table 1.1, we tabulated optical transmission losses, refractive indexes at a range of wavelengths for different geometries of active and passive waveguide devices. First six devices of Table 1.1 related to dating back from 2000. With development of material science and technology in recent years, other polymers have emerged with refractive indices extending up to about 1.54 and having optical losses around 0.25 dB/ cm at the third optical communication window.

ANADOLU ÜNİVERSİTESİ

Table 1.1 Optical properties of selected polymer-based optical waveguides

Material	Wavelength (μm)	Optical Losses (dB/cm)	Refractive Index	Ref.
Polyurethane	0.633	0.8	1.555	[10]
Polyimide mixture	0.83	1.5	1.651-1.642	[11]
Polyetherimide	0.83	0.23	1.61-1.65	[12]
Deuterated Polysiloxane	1.31 – 1.55	0.17 – 0.43	1.5365-1.5345	[13]
Polycarbonate	1.3	0.8 – 1.4	1.539 – 1.537	[14]
Poly(norbornene)	0.82	0.14	Core 1.54 Clad 1.51	[15]
PFCB	1.515 to 1.565	< 0.25	1.487 to 1.49	[16]
PMMA	0.85	0.2	1.49	[9]
Epoxy Resin	0.633	0.3	1.58	[9]
Epoxy Resin	1.064	0.8	1.58	[9]
Polysiloxane	1.31	0.19	1.472 to 1.532	[17]
Deuterated Polysiloxane	1.31	0.12	1.472 to 1.532	[17]
Fluorinated acrylates	1.55	0.25	1.3 to 1.52	[17]

Polymer-based waveguide applications have certain disadvantages. Optical and physical properties of an optical waveguide must not change under a variety of environmental conditions including high temperature and high humidity. However, polymer materials do not have sufficient reliability and thermal stability [18].

1.2.2. Semiconductor Optical Waveguides

One of the other widely used material platforms for waveguide realization is the semiconductor material that is mostly crystalline. High confinement and low optical loss has been demonstrated both theoretically and experimentally for different semiconductors [19, 20]. However, they are mostly anisotropic, i.e., they have different optical and electrical properties in different directions. For example,

ANADOLU ÜNİVERSİTESİ

refractive indices of these materials depend on direction. Optical properties of selected crystalline optical waveguide materials are given in Table 1.2.

Table 1.2 Optical properties of selected semiconductor crystalline-based optical waveguides

Material	Wavelength (µm)	Optical Losses (dB/cm)	Refractive Index	Ref.
Glass/ZnO (polycrystalline)	0.632	60 After polishing: 20	1.97	[21]
Glass/ZnS (nano-polycrystalline)	0.632	5	2.34	[22]
AlGaAs / AlGaAs	0.83	0.1	2.5	[7]
GaAs / AlGaAs	1.52	0.2	3.4	[23]
Potassium niobate	0.86	0.2	2.1-2.35	[24]
(Pb, La) TiO_3	0.633	> 10	1.87 – 2.4	[25]
GaAs/AlGaAs	1.66	0.6	-	[26]
GaAs/AlGaAs	1.55	0.2 Insertion ≤ 3.5	3.37	[27]
GaAs/AIGaAs	1.31	0.19	3.41	[28]
InP/lnGaAsP	~1.55	0.4 for TE 0.65 for TM	-	[29]

Table 1.2 into crystal optical waveguide materials that have been deposited onto a variety of substrate. First two of them have been extensively studied in 1970s and are polycrystalline materials in planar structure. The most popular crystal materials of early 1990s are GaAs and AlGaAs. However, semiconductor waveguides also have some important disadvantages which limit their use. First, the optical propagation losses at the communication wavelengths are relatively high compared to other materials. Moreover, it has highly birefringence and loss because of its crystalline structure. Furthermore, they are highly sensitive to temperature

ANADOLU ÜNİVERSİTESİ

[30]. Finally, fabrication costs of these materials is the main limitation of the technology.

1.2.3. Dielectric Optical Waveguides

Amorphous thin films play a motivating role in the development of integrated optical circuits due to their potential functionality, low cost and easy reachability. In addition, they are isotropic, i.e., they have same electrical and optical properties in all directions. Thus, the most widely used in today's communication technology, are optical elements selected from amorphous materials such as a-silicon, a-silica, a-alumina, etc. Optical properties of selected amorphous optical waveguides are summarized in Table 1.3.

Table 1.3 Optical properties of selected amorphous dielectric optical waveguides

Material	Wavelength (μm)	Optical Losses (dB/cm)	Refractive Index	Ref.
a-SiO_2 / a-SiO_2:Zr	0.632 (HeNe)	-	1.48 – 1.52	[34]
a-SiO_2 / a-SiO_2:Al	0.632 (HeNe)	-	1.48 – 1.49	[34]
SiON	0.632	0.48	1.48 – 1.68	[35]
SiON	1.55	1.8	1.48 – 1.68	[35]
a-SiO_2 / a-SiO_2:Ge	1.55	0.07 0.04 0.02 < 0.01	1.44 – 1.47	[36]
a-SiO2/ a-SiO2:B:P	1.55	< 0.01	1.44 – 1.47	[37]
SiO2/a-Si:H	~ 1.55	1.34	-	[38]
SiO2/a-Si:H	~ 1.55	3.46	-	[38]
Al_2O_3	0.83	< 2	1.7	[39]
Al_2O_3	1.55	0.11	-	[33]

ANADOLU ÜNİVERSİTESİ

Selected materials are tabulated in Table 1.3 with different dopants, designs and growth techniques. The first two of them have silica core with same geometries but different dopants. The third and fourth of them have a-SiON core material with slab channel design, however, applied wavelength is different. Hence, the effect of applied wavelength can be easily recognized. The next two devices have a-SiO_2 core and same design with different dopants. The seventh and eighth devices have a-Si: H^+ core. These devices have different designs which are ridge and photonic wire, respectively. The last of two devices have a-Al_2O_3 core layer which is known to be excellent hosts for rare-earth ions for active and passive integrated optical applications [31, 32]. By now, obtained minimum loss of a-Al_2O_3 is 0.11 dB/cm at 1550 nm [33].

1.3. Rare Earth Doped Optical Waveguides

Optical losses call for the integration of optical amplifiers with waveguides and other components in optical integrated circuit. One simple and efficient technique to increase the optical gain in waveguides is doping the guiding layer with an active elements which generates light when pumping it properly.

Rare earth elements (REEs) are a group of the 15 transition metals from the periodic table of the elements with atomic numbers 57 (lanthanum) through 71 (lutetium) known as lanthanides or lanthanoids. Apart from these elements, the two elements which have similar physiochemistry to the lanthanides in the periodic table are scandium and yttrium. They are commonly found in the same mineral assemblages, and are often referred to as REEs. These elements constitute critical components of many important technologies and products, such as hybrid vehicles, wind turbines, cell phones and optical communications. In particular, well known REEs in OIC applications are erbium, ytterbium and neodymium [40].

In recent years, some of these earth ions have been applied in optical waveguide amplifier and lasers. Trivalent rare-earth ions such as Er^{3+}, $Yb^{3+}$are some of the most suitable dopant ions for optical waveguide applications. Major luminescence wavelengths of these ions are at 1550 nm and 980 nm, respectively. Another suitable host ions is $Nd^{3+}$and it has several luminescence wavelengths at 880, 1060 and 1330 nm. Additional rare earth ions are given in Table1.4. In fact,

ANADOLU ÜNİVERSİTESİ

there are several luminescence wavelength for all rare-earth ions however, the highest gain is usually achieved at these given wavelengths [41].

Table 1.4 Luminescence wavelengths of all rare-earth ions [41]

Rare-earth ion	Luminescence Wavelength
Er^{3+}	1550 nm
Nd^{3+}	880, 1060, 1330 nm
Yb^{3+}	980 nm
Eu^{3+}	615 nm
Ho^{3+}	2100 nm
Tm^{3+}	1900 nm

1.3.1. Erbium Doped Optical Amplifiers

In optical communication technology, thin film IO systems are getting increasing attention following the success of optical fibers. Optical fibers use an optical transition of Er^{3+} because it provides emission around 1550 nm in the low-loss dispersion range. On the other hand, erbium-doped waveguides amplifiers (EDWA) have advantages in terms of size and cost compared to erbium-doped optical fibers. For these devices, silicon is often used as a substrate. Since 1990s, there has been and extensive research in the area of integrated optical amplifiers [42, 43].

1.3.2. Erbium Doping and Host Materials

Erbium is a REE belonging to Lanthanides group. Generally, erbium assumes the trivalent Er^{3+} state when embedded in a solid which has $Xe - 4f^{11}$ electron configuration [44]. The Er^{3+} ion has a partially filled 4f shell allowing for various electron configurations with different energy. The different energy levels occur from spin-spin and spin-orbit interactions. Radiative transitions between many of these energy levels are restricted for free Er^{3+} ions [44, 45].

ANADOLU ÜNİVERSİTESİ

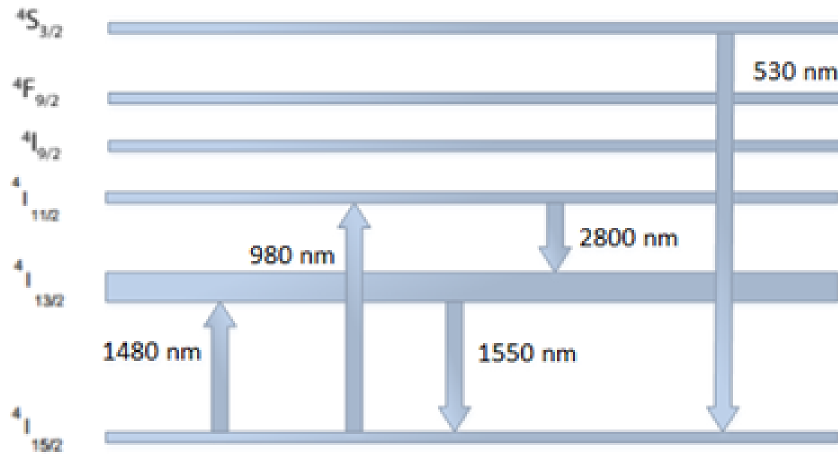

Figure 1.3 Energy level diagram of the Er^{3+} ion, and some common transitions [46].

In a solid, the host material perturbs the 4f energy function. The host material causes Stark-splitting of these energy levels. A schematic energy level diagram is shown in Figure 1.3 for illustrating common energy level transition of an Er^{3+} ion.

As we mentioned in the previous section, the main optical transition of interest of Er^{3+} ion is around 1550 nm [43]. The Er^{3+} ion has additional absorption and ground-state emission lines, including absorption lines centered at 530 nm, 650 nm, 800 nm, 980 nm and 1480 nm [44, 47]. Additionally, emission transitions into excited state at 850 nm, 1200 nm and 2800 nm are possible [48]. Generally, 980nm and 1480 nm pump wavelengths are used to excite the erbium ion [44, 49].

The host material properties for optical waveguide amplifier devices are of utmost importance. Because the up conversion quenching processes depend on the host material and is caused by ion-ion interactions (the interaction between ions). The ion-ion interaction effects relate to the issue of energy transfer between rare earth ions. When the local concentration of rare ions becomes high enough, it is no longer valid to assume that each ion is an isolated ion that acts independently of its neighbors. This can have a negative impact on amplifiers performance when the upper state of an amplifying transition is being depleted by energy transfer. A good host material for Er^{3+} has to fulfill the following requirements; high erbium solubility without clustering, suitable Er^{3+} bonding sites and a high $I_{13/2}$ level radiative lifetime. In addition to these properties, the host material propagation losses should be low [45].

ANADOLU ÜNİVERSİTESİ

One of the most crucial of all these properties is high erbium solubility because the optical path length is short thus the Er concentrations has to be approximately 100 times higher than for the fiber amplifiers [50]. Atomic layer deposition (ALD) has a unique potential that can allow for unprecedented doping concentrations of the host material.

In literature, amorphous, crystalline and polymer materials have been reported as host materials for Er doped waveguide amplifiers and lasers. The main examples are lithium niobate [51], phosphate glass [52], fluoride glass [53], tellurite glass [54], Al_2O_3 [55] and Y_2O_3 [56].

In [51], erbium-doped lithium niobate waveguide lasers is presented. By optical pumping at 1480 nm, a wavelength dependent gain of up to 2 dB/cm is reported at the range of 1530 to 1610 nm. Moreover, the concept of ring lasers in Er^{3+}:$LiNbO_3$ is introduced with their potential to be used as optical gyroscope devices. First experimental results are reported; by pumping with 1480 nm lasing at 1603 nm has been achieved with an output power up to 150 µW. In [52], erbium-doped phosphate glass waveguide which is fabricated with rf sputtering is reported. By pumping the waveguide at 980 nm with a power of ~21 mW, a net optical gain of 4.1 dB for 10 mm long waveguide at 1.535 µm was achieved. The Er concentration was also reported as 5.3×10^{20} cm^{-3}. In [53], erbium-doped fluoride glass waveguides which is fabricated using spin-coating is presented. The waveguides were doped with up to 3 mol % erbium. Scattering losses of 0.2 dB/cm at 975 nm and strong green emission at 520 – 550 nm is observed in erbium-doped waveguides 50 µm in thickness. In [54], Er-doped Tellurite glasses planar waveguide which obtained by a conventional melt quenching method for power amplifier is reported. 0.9 dB/cm gain is observed at a wavelength of 1535 nm, by pumping wavelength at 974 nm. In [55], Al_2O_3: Er^{3+} channel waveguide is reported. A maximum net gain of 5.4 dB/cm was reported at wavelength of 1533 nm by pumping at wavelength of 977 nm. Moreover, optical losses of Al_2O_3 waveguide layers to 0.1 dB/cm is measured. In [56], a signal enhancement of 10 dB at 1535 nm with a low launched pump power of 1mW at 1480 nm is reported for Y_2O_3: Er^{3+}. The gain of Al_2O_3:Er^{3+} can be increased by increasing erbium concentration. By using different growth technique such as atomic layer deposition, erbium

ANADOLU ÜNİVERSİTESİ

concentration can be increased. In future prospects of this study we will focus on to fulfill this objective.

1.3.3. Optical Amplifiers based on $Al_2O_3:Er^{3+}$

The research on Al_2O_3 as a material for use in OC has started in mid-1980s. Compared to other amorphous materials, it has high refractive index, low propagation losses, better thermal stability and high transparency over wide wavelength range [57, 58]. Due to its high refractive index, it has better integration potential for both active and passive optical waveguide devices. Amorphous Al_2O_3 is also excellent host for REEs because it allows the radiative transitions of rare-earth ions [59]. The quality of the waveguide can be affected the particular growth techniques, such as sputtering or atomic layer deposition (ALD). Based on all these properties of Al_2O_3 and the studies of the known Er-doped materials, our ultimate goal is to obtain nanostructured active devices with superior performance based on ALD grown Al_2O_3. In this study, we report optimization of ALD growth parameters for fabrication of amorphous Al_2O_3 host material, potentially suitable for high concentration rare-earth ion doping.

$Al_2O_3:Er^{3+}$ waveguide amplifiers have been researched and many devices reported by several research groups [60, 61, 62, 63, 64, 65, 55]. 5.4 dB/cm optical net gain is demonstrated at 1553 nm [55], lossless power splitters with loss compensation were achieved [66, 67, 68, 69]. Pumping at 977 nm as opposed to 1480 nm total internal net gain of up to 9.3 dB has been measured and an internal net gain was obtained over a wavelength range of 80 nm (1500–1580 nm), and a peak gain of 2.0 dB/cm was measured at 1533 nm [63]. Integrated continuous wave laser was demonstrated [70, 71, 72, 73]. These results show that Al_2O_3 is well suited as a host materials for rare-earth ions.

1.4. Contribution of this thesis

The work presented in this thesis contributes to optimizing the ALD grown Al_2O_3 layers and designing the ridge type waveguide structure through building low loss optical waveguides.

ANADOLU ÜNİVERSİTESİ

Chorological development of integrated optics and comparison of different waveguide materials in the form of a short literature survey are presented in Chapter 1. This chapter also reports on rare-earth doped optical amplifiers used in integrated optics. The second chapter is devoted to the fabrication methods of Al_2O_3 layers. These fabrication methods are compared according to needs of waveguide applications. In chapter 3, the growth optimization study of Al_2O_3 layers by Atomic Layer Deposition (ALD) is presented. This investigation aims at high refractive index, low impurity and high quality layers suitable for applications in active and passive devices. Moreover, the structural and material properties of the resulting layers are investigated. To this end, several characterization results are reported such as X-Ray Diffraction (XRD), Micro-Raman Spectroscopy, Fourier Transform Infrared Spectroscopy (FTIR) and X-Ray Photoelectron Spectroscopy (XPS) investigations. In Chapter 4, the design of the ridge type waveguide is presented. Waveguide design including polarization independent region and single mode operation is presented for telecommunication wavelength range (1.48 to 1.61 μm). In the final chapter, Al_2O_3-based planar waveguide is realized and optical propagation is demonstrated.

ANADOLU ÜNİVERSİTESİ

2. THIN FILM GROWTH TECNIQUES

There are many different techniques used for the deposition of thin film structures for device applications. These are physical methods such as sputtering [74], e-beam evaporation (EBPVD) [75] , pulsed laser deposition (PLD) [76], molecular beam epitaxy (MBE) [77] and also chemical methods such as sol-gel [78], liquid phase epitaxy [73], spin coating [80], chemical vapor deposition (CVD) [81] and atomic layer deposition (ALD) [82, 83]. In this section, several of these growth methods are discussed and their advantages and disadvantages are presented.

2.1. DC/RF Sputtering

Sputtering is based on the breakout of the atoms from the sputtering target surface and growth on the substrate by using the ejected atoms in an ultra-high vacuum (UHV) or high vacuum (HV) chamber. Ar+ ion is generally used as sputtering gas and is usually generated by an ion gun. Basic schematic of DC and RF sputtering systems are shown in Figure 2.1. Firstly, ions are pulsed into the reaction chamber towards the sputtering target. Electric field is used to increase the speed and to affect the direction of the ions to the target. Ions which have high speed and energy are bombarding the target. Next, ions strike the target and eject atoms from its surface. Finally, these atoms move towards to the substrate and deposition of the film is achieved. The substrate may rotate during the growth process depending on the design.

Depending on the target material, RF or DC power may be used. If the target material is a conductor, DC power can be used to effect ions and prevent any charge buildup due to freely moving charges. On the other hand, if the target material is an insulator, the conduction bands will not allow free charge movement. As the ions strike the surface, their charge will remain localized and over time the charge will build up, making it impossible to further bombard the surface. In order to prevent this RF power should be used. When DC power is used in the process called as DC sputtering, when RF power is used it is called as RF sputtering [74, 84].

ANADOLU ÜNİVERSİTESİ

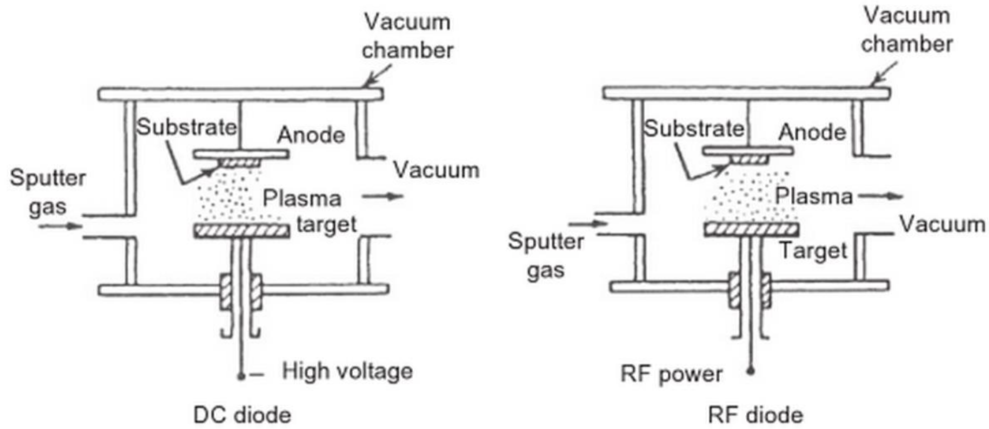

Figure 2.1 Basic schematic of DC and RF sputtering systems [84]

2.2. E-beam Evaporation

This process involves a focused beam of electrons for deposition of the materials in UHV. The electron beam is used to heat the target material and cause evaporation. Then these evaporated atoms transform into solid form on the low temperature substrate. However, the evaporated atoms are not coated only the on the substrate but are also deposited on the reaction chamber. This method has high deposition rate in the range of 0.1 to 100 µm /min [75, 85]. The basic schematic diagram is shown in Figure 2.2.

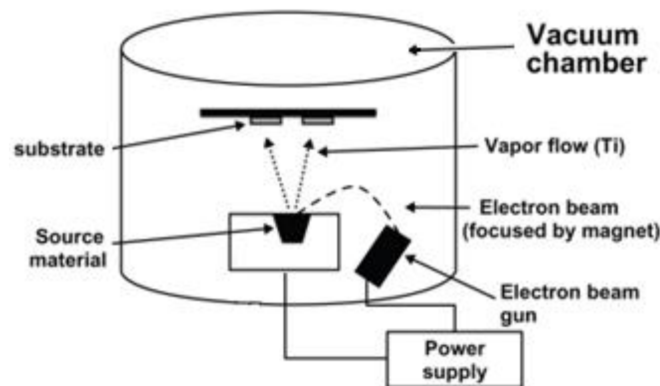

Figure 2.2 Schematic diagram of the electron beam evaporation process [80]

The components of the electron beam evaporation process;

- Electron Beam gun
- A System Controller
- Holder for the target material

ANADOLU ÜNİVERSİTESİ

- Target material
- Substrate
- Power Supply

Generally, this process is used for insulator coating and fabrication of resistor films. It is possible to grow multilayer structures in one duty cycle. Moreover, the layer deposited has high purity and less surface damage. Electron gun degradation causes non-uniformity on the film. In addition, this method is not suitable for coating the complex geometries and also film density, thickness uniformity and step coverage is not sufficient for optoelectronic devices. This method is more suitable for industrial application in particular semiconductor industries [85].

2.3. Pulsed Laser Deposition

In pulsed laser deposition (PLD) method, high power laser is used to evaporate the target and the substrate is directly placed in front of the target. The target surface which is appropriately placed upon the substrate can be ablated by the pulsed laser. The target surface is condensed and collected on the substrate. Thus the thin film is deposited on substrate as shown schematically on Figure 2.3. Application range of this technique is widespread from fabrication of circuit components to medical applications.

PLD technique has significant benefits over other film deposition methods such as the capability for stoichiometric transfer of material from target to substrate, relatively high deposition rates, absence of bombard effect on film growth like sputtering, possibility of low temperature deposition and high film density. In spite of these advantages, industrial uptake of PLD has been slow, creation of small droplets and significantly low film uniformity. Particularly, in optoelectronic application, uniformity of the film and existence of different particulates are main reasons of optical loss [87].

ANADOLU ÜNİVERSİTESİ

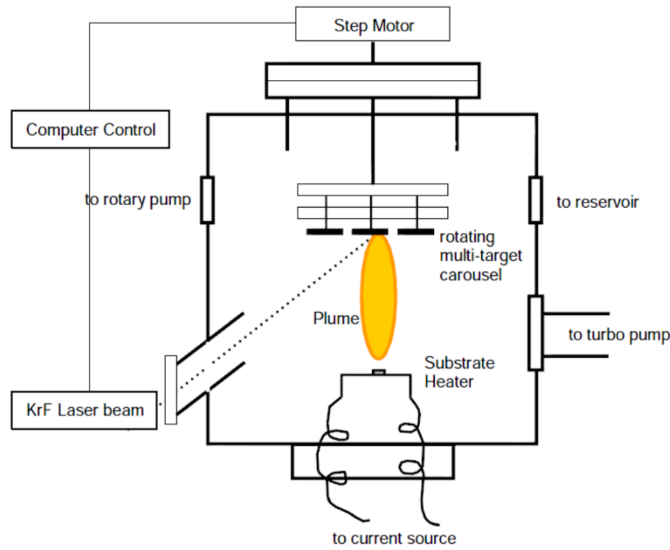

Figure 2.3 Schematic diagram of the pulsed electron deposition process [87]

2.4. Molecular Beam Epitaxy

Molecular beam epitaxy (MBE) technique is needed when films of extremely high purity with almost ideal crystal structure and also capable of producing precise control over composition, doping and interfaces with precise lateral uniformity is required. These factors make MBE a highly controllable and well-rounded technique allowing the growth process itself and hence, optimized and controlled on a monolayer scale. MBE is widely use to grow semiconductor, metal and insulator structures. Principle of MBE is almost the same with classical evaporation and based on reaction of molecular or atomic beams with heated crystalline substrate in an ultra-high vacuum (UHV) condition, as shown in Figure 2.4. The reflecting high energy election diffraction (RHEED) checks the crystal structure [88].

ANADOLU ÜNİVERSİTESİ

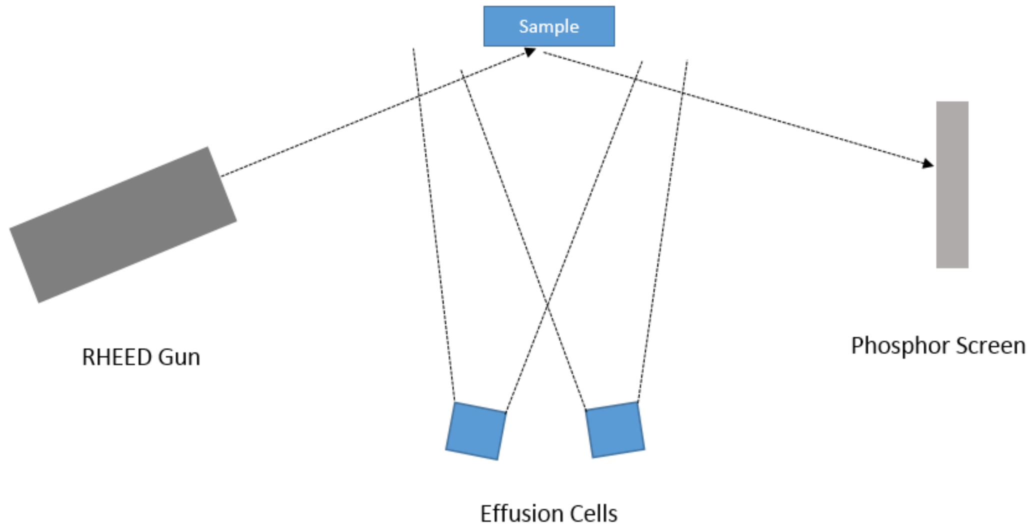

Figure 2.4 Simplified schematic of an MBE

There are several critical parameters affecting the quality of the film. These are flux rate (the number of atoms arriving at the substrate surface), temperature of the substrate (affects diffusive properties of impinging atoms) and temperature of the source (speed of atomic arrival and flux rate). In addition to this, high and low temperatures have own advantages and disadvantages. At high temperature, while mobile surface atoms and highly ordered materials increases, interfaces become smoothed because of diffusion of atoms. At low temperatures, while abrupt interfaces and point defects into layer increases, mobility of atoms decreases. The biggest disadvantage of the method comes from its cost and the limited number of materials that can be grown using this technique [88].

2.5. Chemical Vapor Deposition

Chemical vapor deposition (CVD) has widespread usage in material growth technology. It has been used for deposition of a very wide range of materials. Particularly, it is used for semiconductor wafer fabrication, amorphous and polycrystalline silicon thin films, high purity bulk materials, single crystal silicon layer, deposition of SiO_2 and Si_3N_4 [89].

Basic Growth procedure of CVD is given in Figure 2.5. Firstly, precursor gas/gases are introduced into the reaction chamber containing one or more heated objects. Next, the chemical reactions happen between precursor gasses and heated substrate. As a result, the thin film is coated on the substrate. Finally, the by-

ANADOLU ÜNİVERSİTESİ

products gases of the reaction and unreacted precursor gases are evacuated out of the chamber.

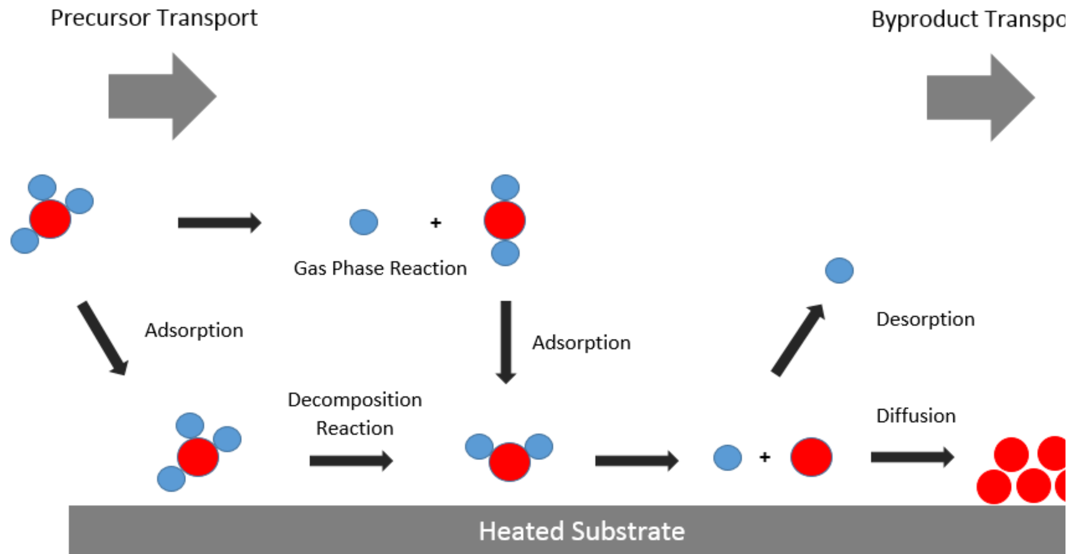

Figure 2.5 Basic growth procedure of CVD.

Compared to other growth methods, CVD has fast recycle time, high deposition rate, and controllable stoichiometry of deposited film. However, CVD has disadvantages such as difficult to control impurity of film, too dangerous

Table 2.1 Comparison of different CVD reactors

Process	***Advantages***	***Disadvantages***	***Application***
LPCVD	- High deposition rate - Low temperature	- Impurity - Poor step coverage	- Deposition of low temperature oxide films
APCVD	- High purity and uniformity - Good step coverage	- Low deposition rate - High temperature	-Deposition of high temperature polycrystalline silicon, SiN and WSi_2
PECVD	- Good step coverage - Low temperature	-Different contamination	-Deposition of low temperature passivation layers and insulators

ANADOLU ÜNİVERSİTESİ

reactive gasses used for deposition and complex reaction and hard to optimize deposition parameters [89]. In addition, there are different reactor modification of CVD such as low pressure chemical vapor deposition (LPCVD), atmospheric pressure chemical vapor deposition (APCVD) and plasma enhanced chemical vapor deposition (PECVD). All these different type of CVDs have their own advantages and disadvantages. Comparison table of different CVD processes is given in Table 2.1.

2.6. Atomic Layer Deposition (ALD)

Another method for making uniform layers is atomic layer deposition (ALD) [90, 91]. This technique was developed in the early 1970's by Tuomo Suntola and co-workers [92]. Because of epitaxial nature of the growth, the process was firstly called atomic layer epitaxy (ALE). This method is based on using two or more precursor reactants for depositing layer by layer solid thin films. ALD process consists of cyclic reaction of precursors. In the growth process, different precursor reactants are pulsed into the reaction chamber sequentially. In every reaction cycle a monolayer film is grown. As it is possible to control every reaction cycle, it enables control of the layer by layer growth of multilayer thin films. The critical parameters of the growth process are pulse time of each precursors, reaction wait

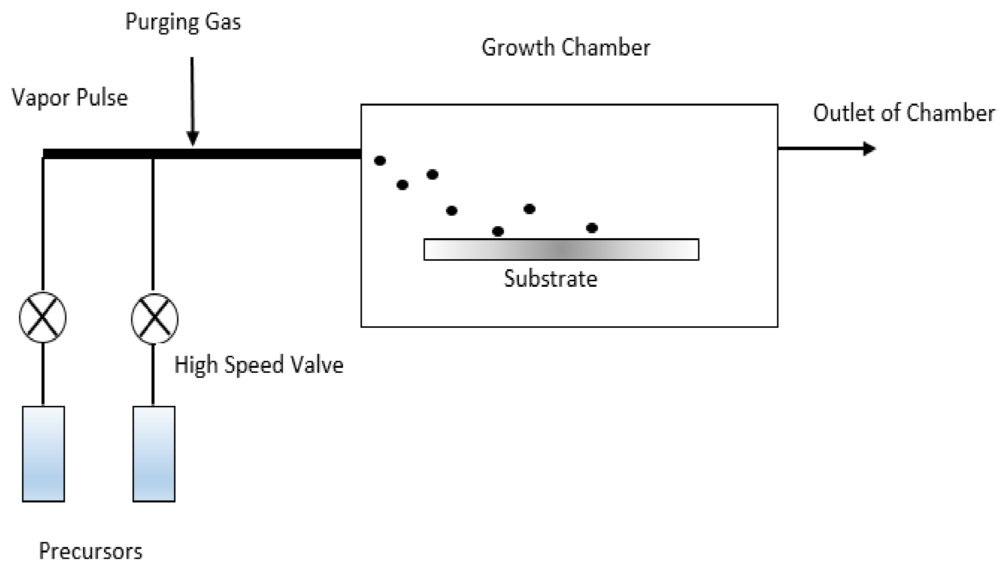

Figure 2.6 Schematic diagram of the ALD reactor

ANADOLU ÜNİVERSİTESİ

time, purge time, process temperature and process pressure. The critical parameters can be optimized according to final device or application. Several different optimization studies are reported in [93, 94, 95, 96, 97, 98] . Basic schematic diagram of ALD process is given in Figure 2.6.

Per cycle growth steps of ALD can be listed as follows;

- First precursor gas which is typically non-metal is pulsed
- Evacuation of by-products of reaction and unreacted precursors, called as purge
- Second precursor which is typically metal is pulsed
- Evacuation of by-products of reaction and unreacted precursors, called as second purge

The above steps are repeated until the desired thickness is reached. Accessible thickness of per cycle can be experimentally determined for different temperature, however, may vary for each different reactor. Accessible thickness may vary from 0.1 to 100 Å. Determination of number of cycles depends on required thickness and type of reactor. Per cycle time can be changed according to the material to be grown and growth temperature and may vary between 0.5 sec. to minutes [90, 99]. An illustration of per cycle growth mechanism is given in Figure 2.7. In Figure 2.7(a), first precursor is pulsed into chamber and placed on the substrate. Then purging of the chamber for evacuating unreacted precursors is shown in Figure 2.7(b). Second precursor is pulsed into the chamber as depicted in Figure 2.7(c), then maintained for a time for the all chemical reaction to complete. In Figure 2.7(d), purge process is repeated for irrelevant molecules evacuation so that cycle is completed. Afterwards the process continues with first precursor pulsed until the desired thickness is obtained.

The advantages of ALD can be summarized as follows,

- Accurate and easy thickness control
- Different multilayer growth capability
- Low impurity level
- Good thickness uniformity due to self-limiting characteristic
- Reproducibility
- Good film density
- Low temperature growth

ANADOLU ÜNİVERSİTESİ

-High performance at high aspect ratio 3D structures

All the above advantages show that ALD is a suitable method for integrated optical circuit and nano-structured optoelectronic devices.

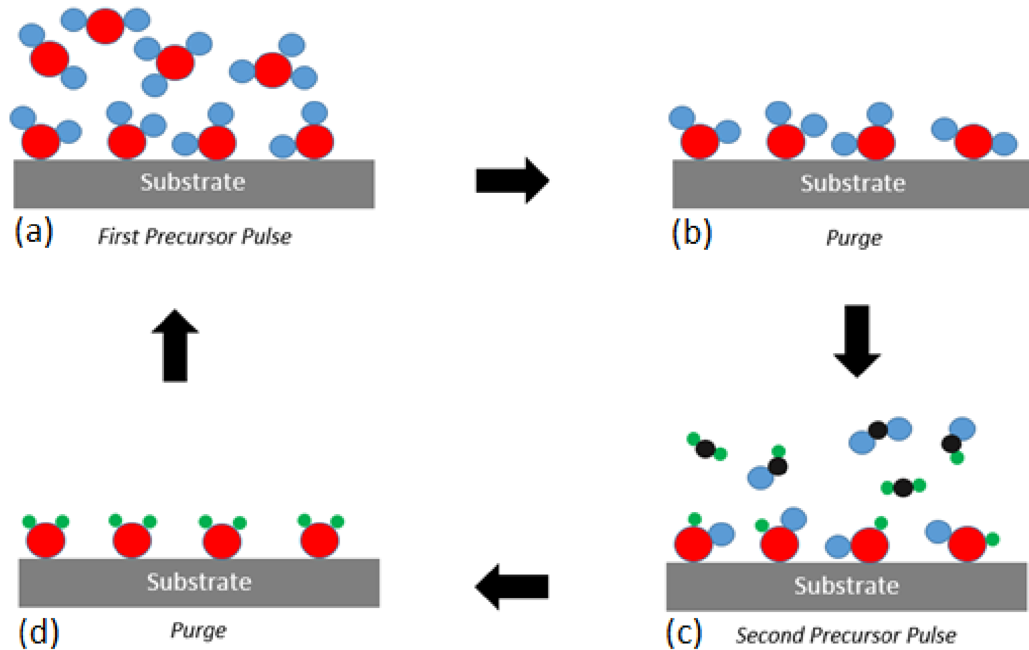

Figure 2.7 Material based schematic representation of per cycle of ALD [100]

2.7. Overall Comparison of Thin Film Growth Techniques

The most widely used method of thin film growth have been discussed in this chapter. Determination of the growth method which according to used area of the device and the material is critical to the success of the application. Because of that the aforementioned growth techniques were compared with each other. Comparison of ALD and traditional counterparts is given in Table 2.2.

According to Table 2.2, all growth techniques have their own advantages and disadvantages. Choice of the growth method depends on the final device. In optoelectronic devices such as waveguides optical losses are critically important. Generally, the main reason of optical loss are non-uniformity, roughness, birefringence and interface reaction for multilayer structure [102, 103].

ANADOLU ÜNİVERSİTESİ

Table 2.2 Comparison of growth methods [101]

Method	*ALD*	*CVD*	*Sputter*	*EBPVD*	*PLD*	*MBE*
Thick. Uniformity	good	good	good	fair	fair	fair
Film Density	good	good	good	fair	good	good
Step Coverage	good	varies	poor	poor	poor	varies
Interface Quality	good	varies	poor	good	varies	good
Low Temp. Dep.	good	varies	good	good	good	good
Deposition Rate	fair	good	good	good	good	fair
Industrial App.	varies	good	good	good	poor	varies

For example, thickness uniformity contributes to optical losses, because of that EBPVD, PLD and MBE growth methods are less desired. Sputtering does not give sufficient interface quality, particularly for multilayer structures it can have negative effects [84]. As for CVD, step coverage, interface quality and low temperature deposition are varies. Particularly, low temperature growth is important for optical devices. Reduction of these several undesired properties of optoelectronic device can be obtained by using ALD. Moreover, ALD has a superior potential for rare-earth ion doping. The weak point of ALD is its slow growth rate, resulting in extended growth time that cause high fabrication cost. This problem can be tolerated by using a large chamber that contains many substrates [104]. As a result, ALD is an interesting growth method with a very high potential for waveguide applications.

Due to high refractive index, high transparency and dielectric properties, Al_2O_3 is a natural candidate for low loss optical waveguides. Even though there are several research on the deposition of Al_2O_3 thin-films by the ALD [105], most of them do not provide the information about optical properties of Al_2O_3 for optoelectronic device design.

Al_2O_3 thin films growth are reported in the literature thoroughly. High quality Al_2O_3 are reported with different deposition methods such as sputtering [106, 58] , CVD [107], PLD [108], ALD [109]. Propagation loss of Al_2O_3 film is about 1

ANADOLU ÜNİVERSİTESİ

dB/cm at 633 nm was reported in [106] by using DC sputtering. Deposition of Al_2O_3 film on oxidized silicon substrate with RF sputtering technique was investigated in [58]. Effect of annealing process at 800 C is also reported for both refractive index and propagation loss of Al_2O_3 film. After annealing, the refractive index increased about from 1.54 to 1.7 and propagation loss decreased about from 25 to 1 dB/cm at 633 nm. Propagation loss was founded in [107], and [108] 0.2 dB/cm at near IR region after annealing at 800 C and 2.5 dB/cm at 633 nm, respectively. ALD Al_2O_3 waveguide onto glass and fused silica substrate was reported in [109] that consist of 1.1 ± 0.3 dB/cm at 633 nm.

ANADOLU ÜNİVERSİTESİ

3. FABRICATION AND CHARACTERIZATION OF AL_2O_3 LAYERS

3.1. ALD Growth of Al_2O_3 Layers

In this section, ALD growth parameters will be mentioned then the growth parameter variation used in this study will be presented and wafer preparation procedure will be described for the ALD grown Al_2O_3 layers.

3.1.1. ALD Growth Parameters

The Cambridge Nanotech Savannah-100 ALD system was used to deposit Al_2O_3 layers. Trimethylaluminum (TMA) and de-ionized water (H_2O) were used as precursors of Al and O, respectively. TMA which is chemical compound with a chemical formula $Al(CH_3)_3$ which is a colorless liquid organoaluminium compound [110]. Continuously flowing N_2 gas was used as carrier and purge gas while adding precursor and pumping continuously. Nitrogen (or argon) flow is used for several reasons. The first reason is to prevent flow of precursor from one pulse valve into the other. It is important that the pulse valves only see their own precursor, thus each valve has a constant nitrogen flow. The constant nitrogen flow out of each valve prevents other precursors to enter, and thus prevents deposition on each valve. A recommended nitrogen flow value is 20 Standard Cubic Centimeters per Minute (sccm). During venting this is increased to 100 sccm, and also while the reactor is open, this should be the maximum flow value (100 sccm) to prevent air from entering the valve regions.

The second and major reason for using nitrogen in the ALD system is to quickly purge the system between each pulse (called as purge time). It is important that between the precursor pulses, there is no residue (except for the monolayer chemically bonded to the substrate) of precursor in the reactor. The presence of two precursors at the same time would cause immediate reaction in vapor phase, which can lead to CVD (described in the previous chapter) mode deposition (non-uniformity, thick coating and powder formation are to be expected). Therefore, the combination of temperature, nitrogen flow and purge time between pulses prevents two precursors from interacting with each other in a vapor phase. It means that the impurity level can be controlled by changing purge time at a constant temperature.

ANADOLU ÜNİVERSİTESİ

Moreover, at low reactor temperatures (e.g. 150 °C), the purge time needs to be higher (e.g. 20 sec) than at high temperatures (>150 °C, purge time e.g. 8 sec, for TMA) [111]. The higher the temperature, thus the faster the cycles.

Properties of Al_2O_3 layers using different experimental parameters which are chamber/substrate temperature, pressure inside the chamber and pulse and purge time duration can be varied in order to optimize the grown layer. Thus, the desired film properties can be achieved by optimizing these parameters, particularly chamber/substrate temperature and purge time.

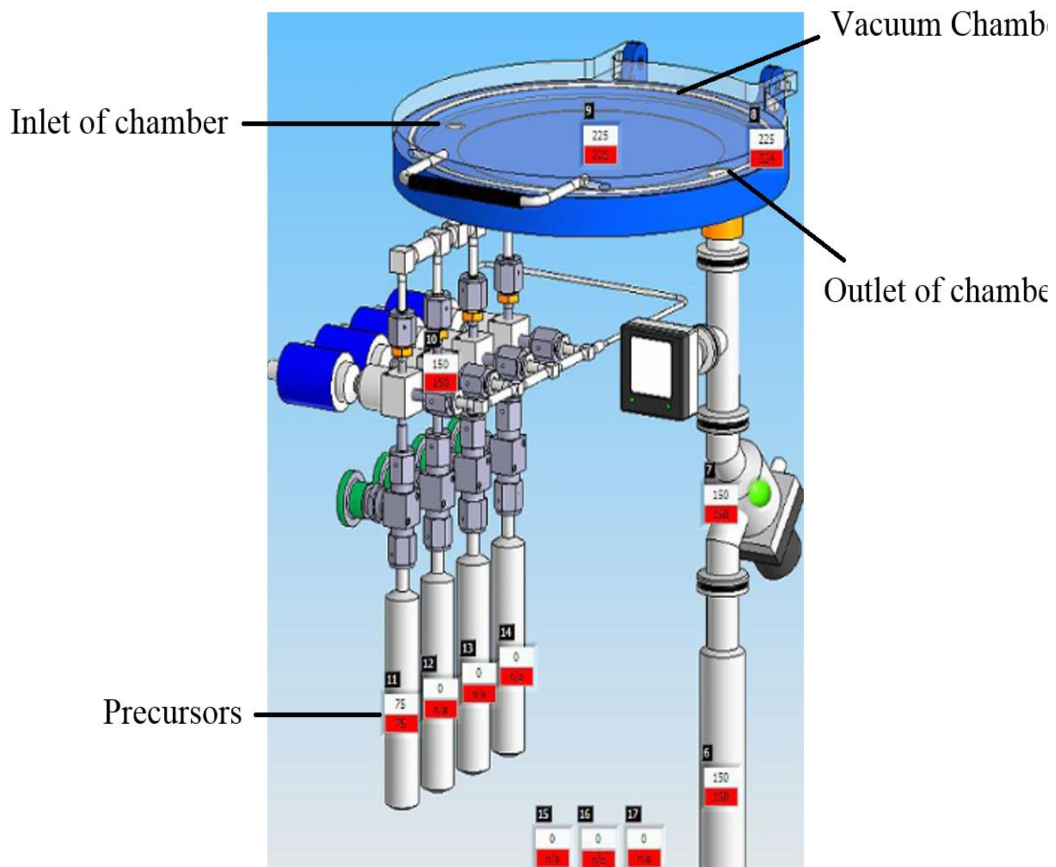

Figure 3.1 Schematic illustration of Savannah-100 ALD system [111]

A schematic illustration of ALD system is displayed in Figure 3.1. The system consists the following components: a gas cabinet that houses the ALD precursors, a reaction (vacuum) chamber where the precursor gases interact with the sample and a control computer. The base pressure of this setup is ~400 mtorr with 5 s.c.c.m of N_2 flowing into the reaction chamber.

ANADOLU ÜNİVERSİTESİ

3.1.2. Deposition Procedure and Growth Matrix

List of the growth parameters that we have studied are given in detail in Table 3.1. There are eight different samples. The average size of the each sample was ~3 cm and the sample shapes were rectangular due to the crystal orientation of the silicon substrate. The growth temperature was varied from 150 to 300 °C in order to observe the temperature effect on the grown Al_2O_3 such as the refractive index, thickness, etc.

Table 3.1 Growth-Parameter Matrix

	Sample 1	*Sample 2*	*Sample 3*	*Sample 4*
Temperature	300 °C	300 °C	250 °C	250 °C
Pulse Time	0.015 seconds	0.015 seconds	0.015 seconds	0.015 seconds
Purge Time	4 seconds	20 seconds	4 seconds	5 seconds
Pressure	20 sccm ~ 600-700 mTorr	20 sccm ~ 600-700 mTorr	20 sccm ~ 600-700 mTorr	20 sccm . ~ 600-700 mTorr
Cycle	500	500	500	500
	Sample 5	***Sample 6***	***Sample 7***	***Sample 8***
Temperature	200 °C	200 °C	150 °C	150 °C
Pulse Time	0.015 seconds	0.015 seconds	0.015 seconds	0.015 seconds
Purge Time	4 seconds	8 seconds	4 seconds	20 seconds
Pressure	20 sccm ~ 600-700 mTorr	20 sccm ~ 600-700 mTorr	20 sccm ~ 600-700 mTorr	20 sccm ~ 600-700 mTorr
Cycle	500	500	500	500

The purge time was chosen 4 seconds and 20 seconds for each temperature. Thus, the purge time effect on the each sample will be observed. The other variables which are the pulse time of each precursors and continuous flow of N_2 gas were kept constant at 0.015 seconds, 20 sccm, respectively. Each deposition cycle consists of the following steps. The TMA precursor is pulsed into the reactor chamber for 0.015 seconds, then the reactor chamber is purged with N_2 gas (20 sccm), which is followed by the introduction of the H_2O precursor into the process chamber for 0.015 seconds, and finally the chamber is purged again with N_2 (20 sccm). During purge no precursors was introduced in to the reactor. Those steps complete one full cycle that forms approximately one atomic layer on the substrate

ANADOLU ÜNİVERSİTESİ

surface; by replicating the cycle described above at a certain number of times one can obtain a precise film thickness.

Growth parameter variation was used for optimization of the Al_2O_3 layers. In order to optimize the ALD experiments were repeated at various chamber/substrate temperature, pulse and purge time. Effects of these parameter variations were investigated with a goal to obtain amorphous and high refractive index Al_2O_3 layers with low optical losses.

3.1.3. Wafer preparation

The substrates were 500 µm thick p-type Si (100) wafers with a resistivity of 20-40 ohm/cm. A three-step cleaning process was applied to the substrate before each growth experiment. First, acetone was applied in order to remove organic contaminants from the substrate surface for 5 minutes. Its high evaporation rate, however, requires a subsequent cleaning step in order to avoid striations. As a second step, isopropyl alcohol was used for 1 minutes for rinsing contaminated acetone off as well as removing particles from substrate. Thirdly, water was used for cleaning the isopropyl alcohol. Finally, N_2 gas was used to of dry the surface and the samples were baked for 5 minutes at 120 ºC.

3.2. Spectroscopic Ellipsometer Measurement

Thickness and refractive index of Al_2O_3 layers were characterized by J.A. Woollam Co., Inc. WVASE Spectroscopic Ellipsometer. The Variable Angle Spectroscopic Ellipsometer (VASE) technique measures the polarization state change for light reflected from or transmitted through a material structure. The electrical field of linearly polarized incident light can be projected into two orthogonal polarization components, as shown in Figure 3.2.

E_p, p-polarized electric field component, is parallel to the incidence plane, defined by the incident beam and the direction normal to the surface. E_s, s-polarized electric field component, is perpendicular to the incidence plane. Different polarized waves behave differently when they are reflected from the sample. The sample can be a bulk material where reflection happens at the air/bulk interface [112]. Moreover, the sample can have complex structure which has several different

ANADOLU ÜNİVERSİTESİ

material layers, with reflections at each interface between different material layers. The ratio of the amplitude of the reflected wave to that of the incident wave is defined as the reflection coefficient, which is denoted as R_p and R_s for p- and s-polarized light, respectively.

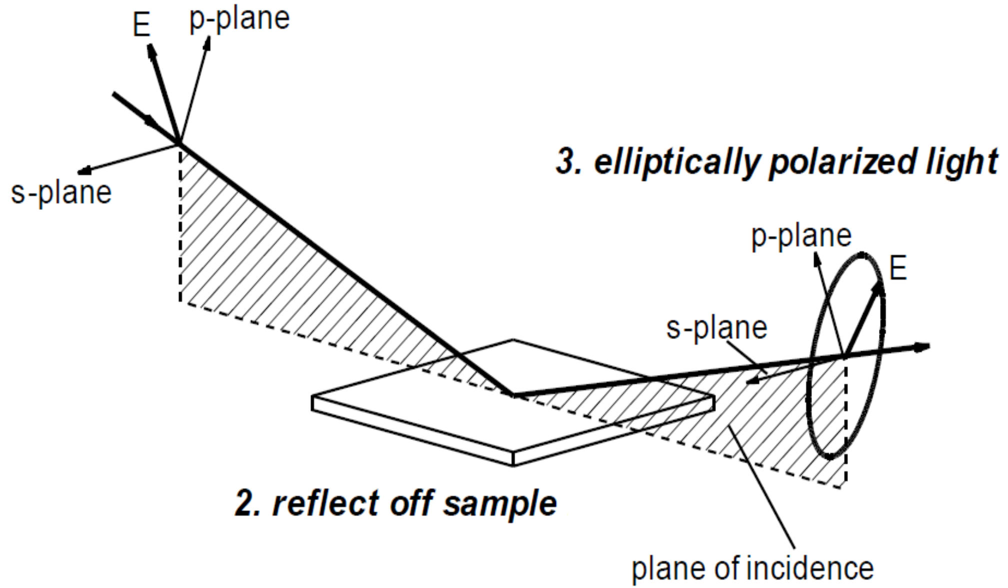

Figure 3.2 Geometry of Ellipsometric Measurement [113]

The complex reflection coefficient contains information about both the amplitude and the phase change upon reflection. Typically, the amplitude of R_p and R_s are not identical, and they are not in phase either. Their amplitude ratio and the phase difference denote the polarization state change [112, 114]. Equation (3.1) is used to describe the polarization state change, we define two parameters Ψ and Δ as:

$$\rho = \tan\psi e^{i\Delta} = \frac{R_p}{R_s} \tag{3.1}$$

Ψ and Δ, which are the data we obtain from a VASE measurement, describe the amplitude ratio and the phase difference, respectively, for a range of photon energies and incidence angles [112]. After mentioned the theory of VASE measurement procedure, the general steps to analyze the data from a VASE measurement are shown in Figure 3.3.

ANADOLU ÜNİVERSİTESİ

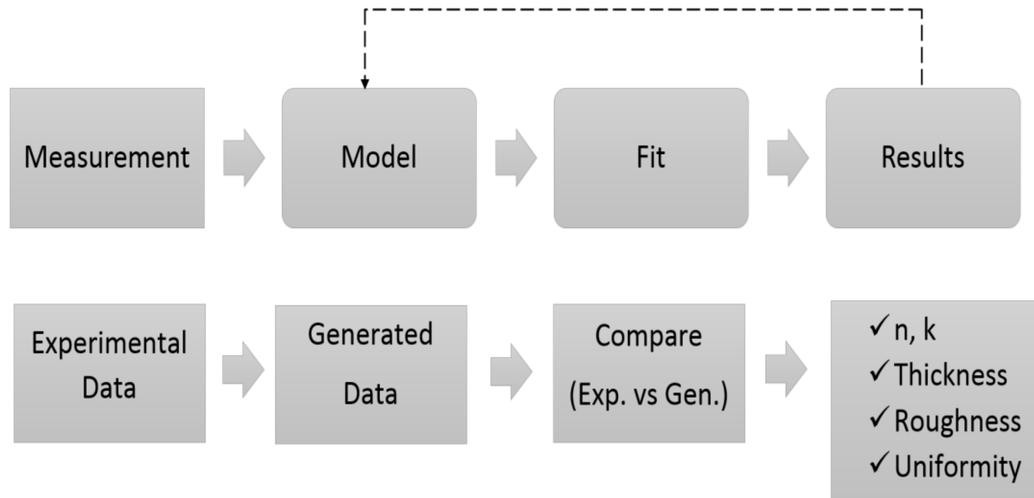

Figure 3.3 Measurement Procedure of Spectroscopic Ellipsometer

The spectroscopic measures the beam intensities (reflectance and transmittance) or polarization states (ellipsometric ψ and Δ), usually as functions of the light beam wavelength, angle of incidence and polarization state [112].There are eight samples grown with different parameters given in Table 3.1. Cauchy coefficients of all samples are given in Table 3.2. As a common trend, the refractive index of Al_2O_3 was observed to show a steady decrease in accordance with the Cauchy equation which is described in Equation (3.2):

$$n(\lambda) = B + \frac{C}{\lambda^2} + \frac{D}{\lambda^4} + \cdots \tag{3.2}$$

n and λ is the refractive index and wavelength values, respectively. The constants B, C, D, etc. are determined by fitting the equation.

ANADOLU ÜNİVERSİTESİ

Table 3.2 Cauchy Equation's Coefficients of samples

	B	***C***	***D***
Sample 1	1.639	2.434×10^{-15}	6.444×10^{-28}
Sample 2	1.625	4.267×10^{-15}	2.264×10^{-28}
Sample 3	1.636	4.272×10^{-15}	2.847×10^{-28}
Sample 4	1.628	3.711×10^{-15}	4.390×10^{-28}
Sample 5	1.634	5.783×10^{-15}	-6.200×10^{-29}
Sample 6	1.629	5.405×10^{-15}	1.928×10^{-28}
Sample 7	1.623	4.267×10^{-15}	2.264×10^{-28}
Sample 8	1.637	2.410×10^{-15}	6.579×10^{-28}

Table 3.3 The film thicknesses and growth rates of samples

	Thickness (nm)	***Growth rate (Å/cycle)***
Sample 1	54.52 ± 0.34	1.09
Sample 2	52.92 ± 0.11	1.06
Sample 3	58.43 ± 0.13	1.17
Sample 4	57.77 ± 0.34	1.15
Sample 5	60.77 ± 0.13	1.22
Sample 6	57.51 ± 0.42	1.18
Sample 7	59.47 ± 0.11	1.19
Sample 8	56.49 ± 0.38	1.13

We have also observed a measurable dependence of the growth rate on the different recipes. 500 ALD cycle-growth process was applied to all samples. The film thicknesses and growth rates of samples are given in Table 3.3. The samples grown at the same temperature were evaluated together. The film thicknesses of "Sample 1" and "Sample 2" were measured 54.52 ± 0.34 nm and 52.92 ± 0.11 nm and growth rates were calculated 1.09 and 1.06 Å/cycle at a temperature of 300 °C, respectively. The film thicknesses of "Sample 3" and "Sample 4" were measured 58.43 ± 0.13 nm to 57.77 ± 0.34 nm and growth rates were calculated as 1.17 and 1.15 Å/cycle at a temperature of 250 °C, respectively. The film thicknesses of "Sample 5" and "Sample 6" were measured 60.77 ± 0.13 nm to 57.51 ± 0.42 nm

ANADOLU ÜNİVERSİTESİ

and growth rates were calculated 1.22 and 1.18 Å/cycle at temperature of 200 °C, respectively. The film thicknesses of “Sample 7” and “Sample 8” were measured 59.47 ± 0.11 nm to 56.49 ± 0.38 nm and growth rates were calculated 1.19 and 1.13 Å/cycle at temperature of 150 °C, respectively. As a common trend, the thickness of the samples grown at same temperature decreased with increasing purge time.

3.2.1. The effect of temperature on Al_2O_3 layers

In order to observe the effect of the growth temperature on the layer properties, the pulse time, purge time and the chamber pressure were kept constant and only the temperature was varied 300 °C to 150 °C, in steps of 50 ºC. These samples named as “Sample 1”, Sample 3, “Sample 5” and Sample7 were selected for the investigation.

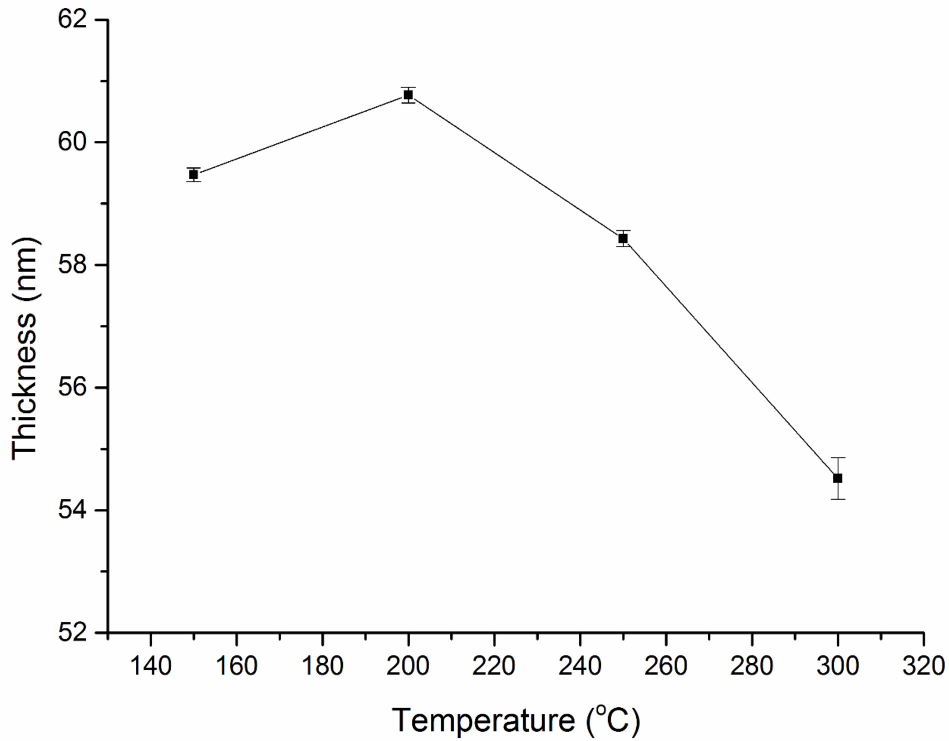

Figure 3.4 The effect of growth temperature on growth rate

Firstly, the Al_2O_3 growth rate versus temperature determined by measuring the film thickness after 500 cycles at various temperature is given in Figure 3.4. In agreement with literature, the lower Al_2O_3 growth rates are consistent with half-reactions that do not go to completion at 150 °C [115, 116]. Moreover, the growth

ANADOLU ÜNİVERSİTESİ

rate increases with temperature up to 200 °C. Then, the growth rate decreases with increasing the temperature. The decrease of the growth rate is most likely caused by dehydroxylation of the surface which begins at 180 °C, possibly resulting in a denser film and low impurities [117].

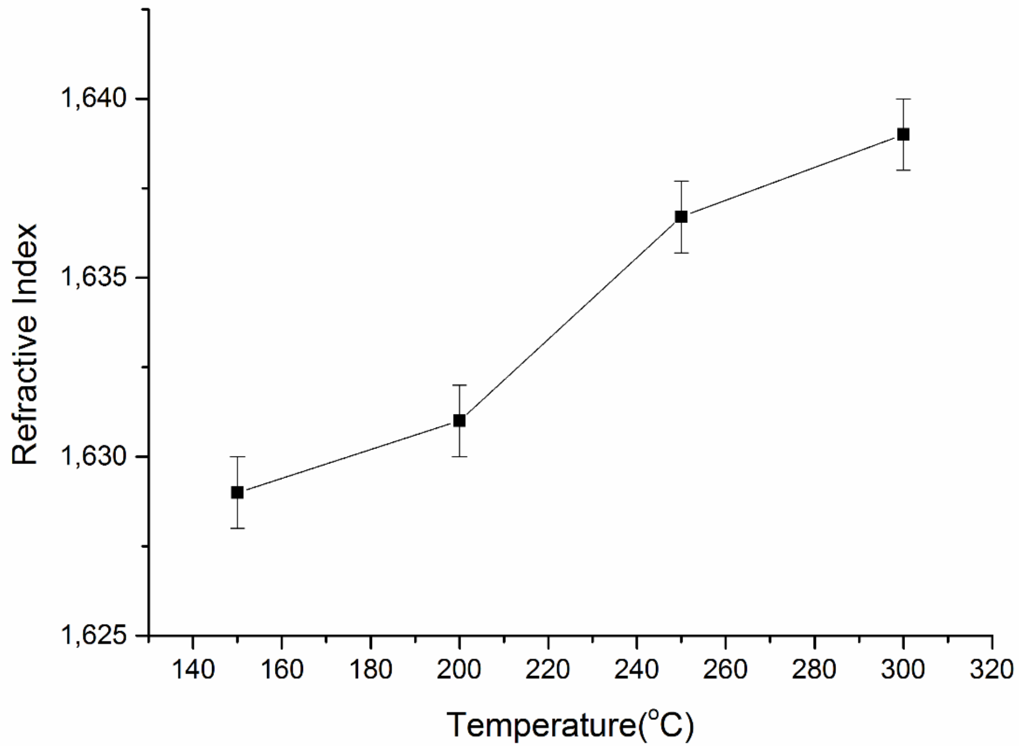

Figure 3.5 The effect of the growth temperature on the refractive index of Al_2O_3 at λ=1550 nm

Next, Figure 3.5 shows the Al_2O_3 refractive index at 1550 nm versus surface temperature determined by measuring the film refractive index after 500 cycle at various substrate temperatures. The refractive index of Al_2O_3 at 1550 nm were measured to be 1.629±0.001, 1.631±0.001, 1.636±0.001 and 1.639±0.001 at temperatures of 150, 200, 250 and 300°C, respectively. Steady increase of the refractive index was observed with increasing the temperature. The low refractive index at low temperature is possibly correlated with the AlOH and CH_2-CH_3 surface species [113]. This statement will be supported with FTIR results at the later stage of the study.

ANADOLU ÜNİVERSİTESİ

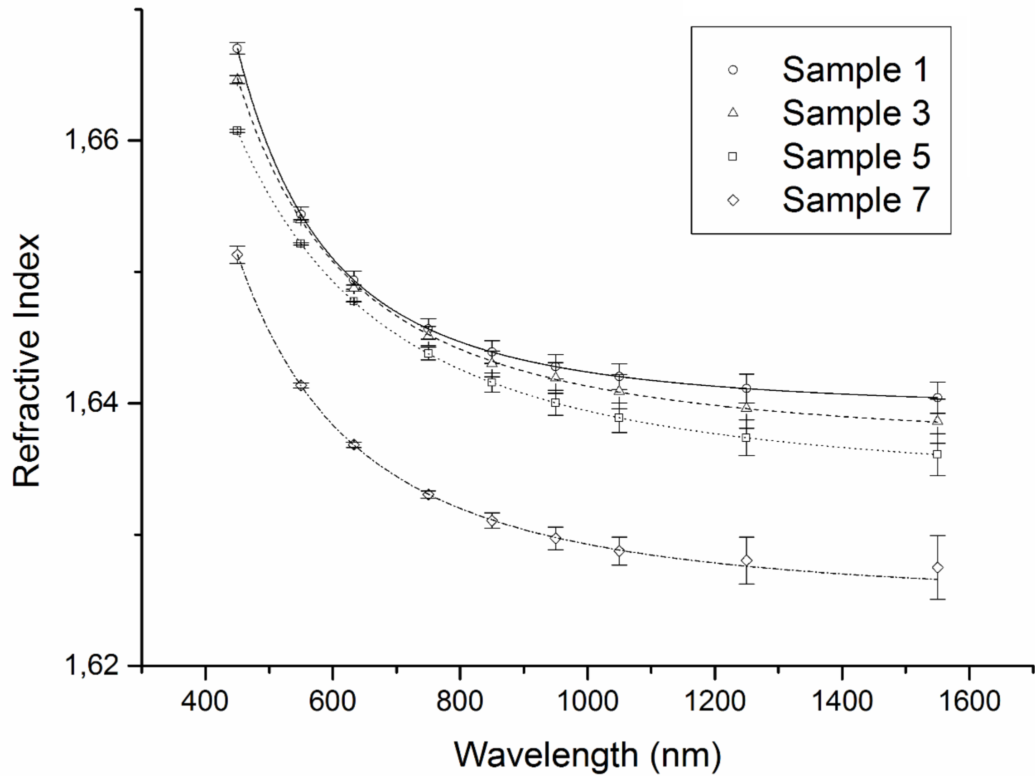

Figure 3.6 Refractive Index vs. Wavelength of different temperature growth

Finally, the refractive index versus wavelength is given in Figure 3.6. It is clear that the process/substrate temperature is critical for optical properties of Al_2O_3 layers. In agreement with the Figure 3.5, the refractive index increases with increasing temperature.

3.2.2. The effect of purge time on Al_2O_3 layers

Figure 3.7 shows the refractive index as a function of wavelength by varying purge time from 4 to 20 seconds at 300 °C which named as "Sample 1" and "Sample 2", respectively. The refractive index of the "Sample 1" varied from 1.67 to 1.64 and "Sample 2", from 1.66 to 1.64 at a wavelength range of 450 to 1550 nm, respectively. The refractive indices of the two layers at λ=1550 nm were measured to be 1.639±0.004 and 1.640±0.004, for the "Sample 1" and "Sample 2", respectively.

ANADOLU ÜNİVERSİTESİ

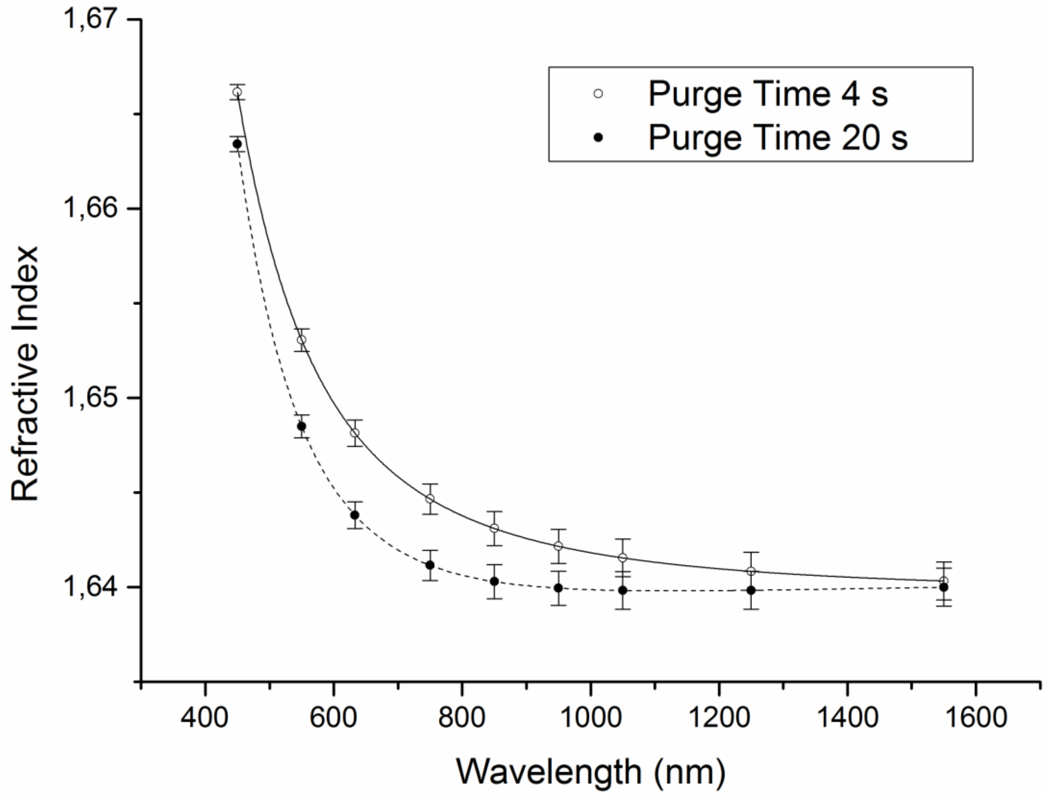

Figure 3.7 Refractive Index vs. Wavelength of Sample 1&2

The refractive of both samples were approximately the same within the detection accuracy, particularly at λ=1550 nm. This event has probably occurred because of the activation energy of TMA, i.e. TMA has more energy for reaction at 300 °C. 4 seconds purge time is enough for putting away the residual molecules from the reaction chamber. Increase of the purge time did not have considerable effect on the refractive index at 300 °C.

The refractive index variation for given "Samples 7" and "Sample 8" in Figure 3.8. These samples were grown at the 150 °C with 4 and 20 seconds purge time, respectively. The refractive index of the "Sample 7" varied from 1.65 to 1.62 and "Sample 8", from 1.67 to 1.63 between the wavelengths of 450 to 1550 nm. The refractive indices of the two layers at λ=1550 nm were measured to be 1.626±0.002 and 1.629±0.001, for the "Sample 7" and "Sample 8", respectively.

ANADOLU ÜNİVERSİTESİ

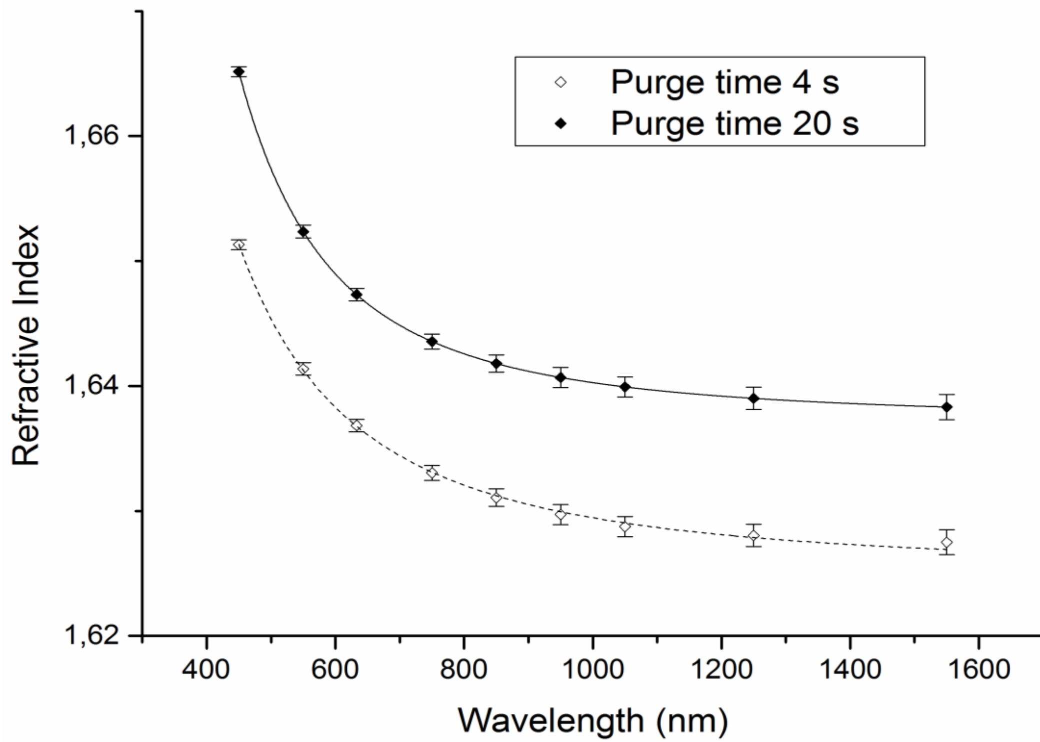

Figure 3.8 Refractive Index vs. Wavelength of Sample 7&8

These results showed that the hydroxylation surface coverage is higher on Al_2O_3 surfaces and the TMA reaction with Al-OH surface species groups does not go to completion at low temperatures because of the activation energy of TMA is higher Additionally, TMA molecules do not have enough activation energy to make a bond with H_2O molecules effectively at less purge times. Due to this reason, the purge time that is necessary in order to make bonds has to be longer than purge time at high temperature values. As a natural consequence of this event, the refractive index decreases at low temperatures. All the experiments and relevant literature support the fact that inclusion of the OH species in Al_2O_3 films increases with decreasing the temperature and vice versa.

ANADOLU ÜNİVERSİTESİ

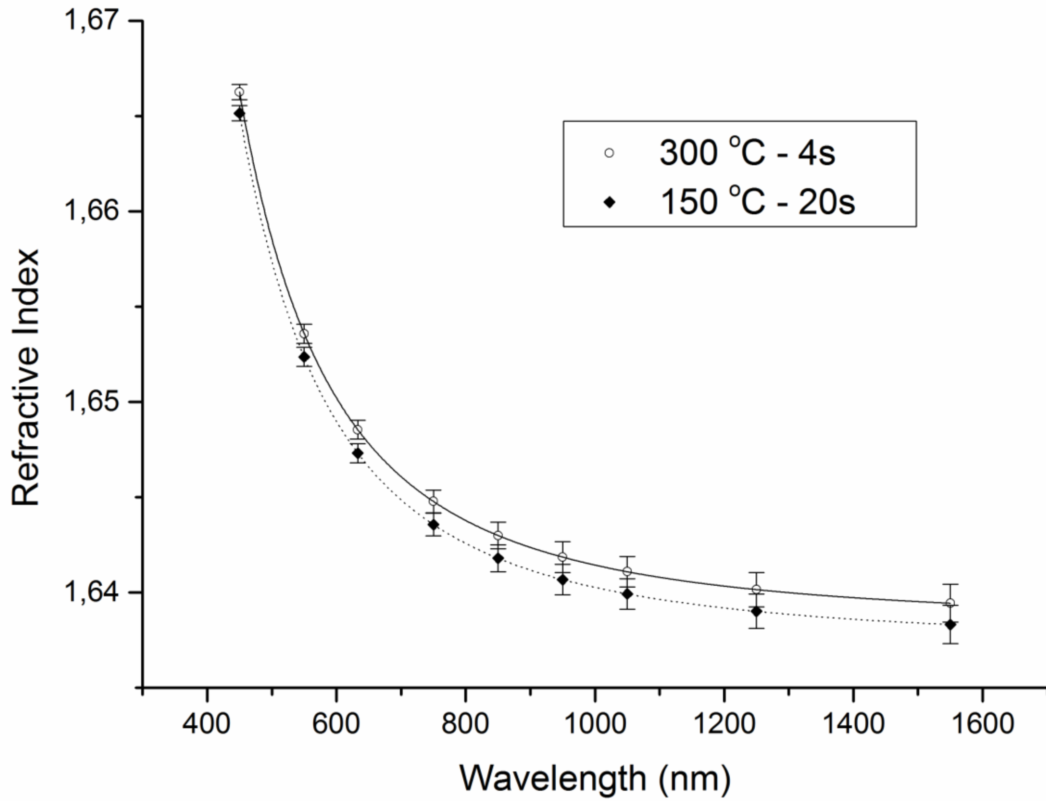

Figure 3.9 Refractive Index vs. Wavelength of Sample 1&8

Comparison of the refractive index at different wavelengths of 300 °C with 4 seconds purge time and 150 °C with 20 seconds purge time are given in Figure 3.9. Due to being a shortest process the growth at 300 ºC with 4 seconds purge time was decided to be used in our study. In order to support this decision, sample's elemental composition, crystalline phases present, optical film quality, physical properties, etc. need to be investigated. To achieve this, three samples which were grown at 300 ºC with purge time of 4 seconds (Sample 1), 200 ºC with purge time of 4 seconds (Sample 5) and 150 ºC with purge time of 4 seconds (Sample 7) were selected for characterization and have been used in this work.

3.3. X-Ray Diffraction Measurement (XRD)

Another important desired property of the targeted Al_2O_3 layers is to achieve amorphous structure. In order to minimize any potential optical losses in waveguides based on ALD Al_2O_3 and to eliminate birefringence we have intentionally targeted amorphous structures. The investigation of the crystallinity

ANADOLU ÜNİVERSİTESİ

was performed using X-Ray diffraction. For this purpose Pananalytical X’pert Pro Material Research Diffractometer was used.

3.3.1. Basic Concepts

When a wave propagates in a film scattering occurs, as a result when a periodic wave is incident on a film, diffraction effects can be observed. So the diffraction from waves with different wavelengths reveals the structure of a film at different length scales [118]. The films can be in amorphous or crystalline state. There is a three dimensional distribution of atoms in a crystalline film structure. These are arranged so that they form a series of parallel planes separated from one another by a distance *d*, which varies according to the material. Every crystal plane has a different orientation with its own specific distance *d*. X-Ray Diffraction (XRD) identifies the phase composition of the analyzed films if they are crystalline, polycrystalline or amorphous. Amorphous films are hard to be analyzed by this method because of their random arrangement of atoms in the film [119].

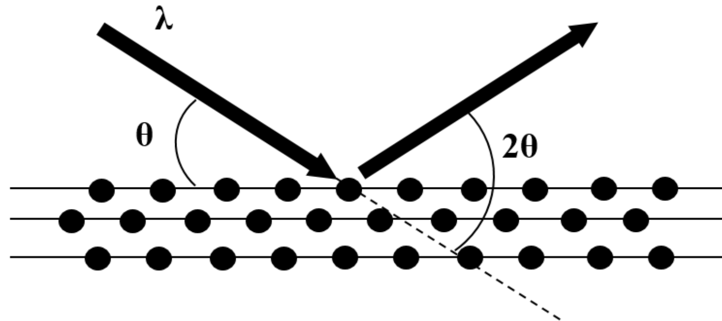

Figure 3.10 Schematic illustration of Bragg’s law

XRD consist of an X-ray generator, a goniometer, holder, and an X-ray detector. X-rays are generated within a sealed tube. For heating the filament current is applied. Then, high voltage is applied within the tube. The electrons which hit a target are accelerated after application of high voltage [119]. X-rays are produced when these electrons hit the target. The emitted wavelength is characteristic for elements of that target. These X-rays are collimated and directed onto the substrate [120]. The X-ray beam hits the sample and the detector records the X-ray intensity diffracted at the substrate. When propagating through a crystal, the X-rays interact

ANADOLU ÜNİVERSİTESİ

with the lattice and are diffracted according to the Bragg's law (Figure 3.10). Bragg Law is described by Equation (3.3) [119, 120]:

$$2d\ (sin\ \theta)\ =\ n\lambda \tag{3.3}$$

θ is the x-ray incidence angle (Bragg angle), n is the order of diffraction, d is lattice interplanar spacing of the crystal, and λ is the wavelength of X-ray. The diffraction angle 2θ is double of the incident angle θ. The goniometer is moves through a range of 2θ angle. The detector measures the intensity of the reflected radiation, the Bragg Law is satisfied for each measurement. An X-Ray detector records the diffracted beam intensity as a function of the angle (2θ). Every crystalline material will give a characteristic diffraction pattern, thus the diffraction pattern acts as a unique "fingerprint". The plot of XRD patterns are identified by comparing them with standard XRD patterns database [119, 120].

3.3.2. XRD Results

Figure 3.11 shows the XRD pattern of deposited three selected samples one under the other. From the bottom to top the graphs refers to the grown samples at 150 ^{o}C and 4 seconds purge time, 200 ^{o}C and 4 seconds purge time and 300 ^{o}C and 4 seconds purge time in sequence. At 150 ^{o}C and 4 seconds purge time and at 200 ^{o}C and 4 seconds purge time, no peak was observed. The two weak and high full width half maximum (FWHM) peaks in the patterns of growth at 300 ^{o}C and 4 seconds purge time was observed at the limit of detection. As a comment, both peaks can be correlated with α-Al_2O_3 and γ-Al_2O_3 in amorphous state [121, 122]. These observations proved that ALD processes reported here have an amorphous structure [123].

ANADOLU ÜNİVERSİTESİ

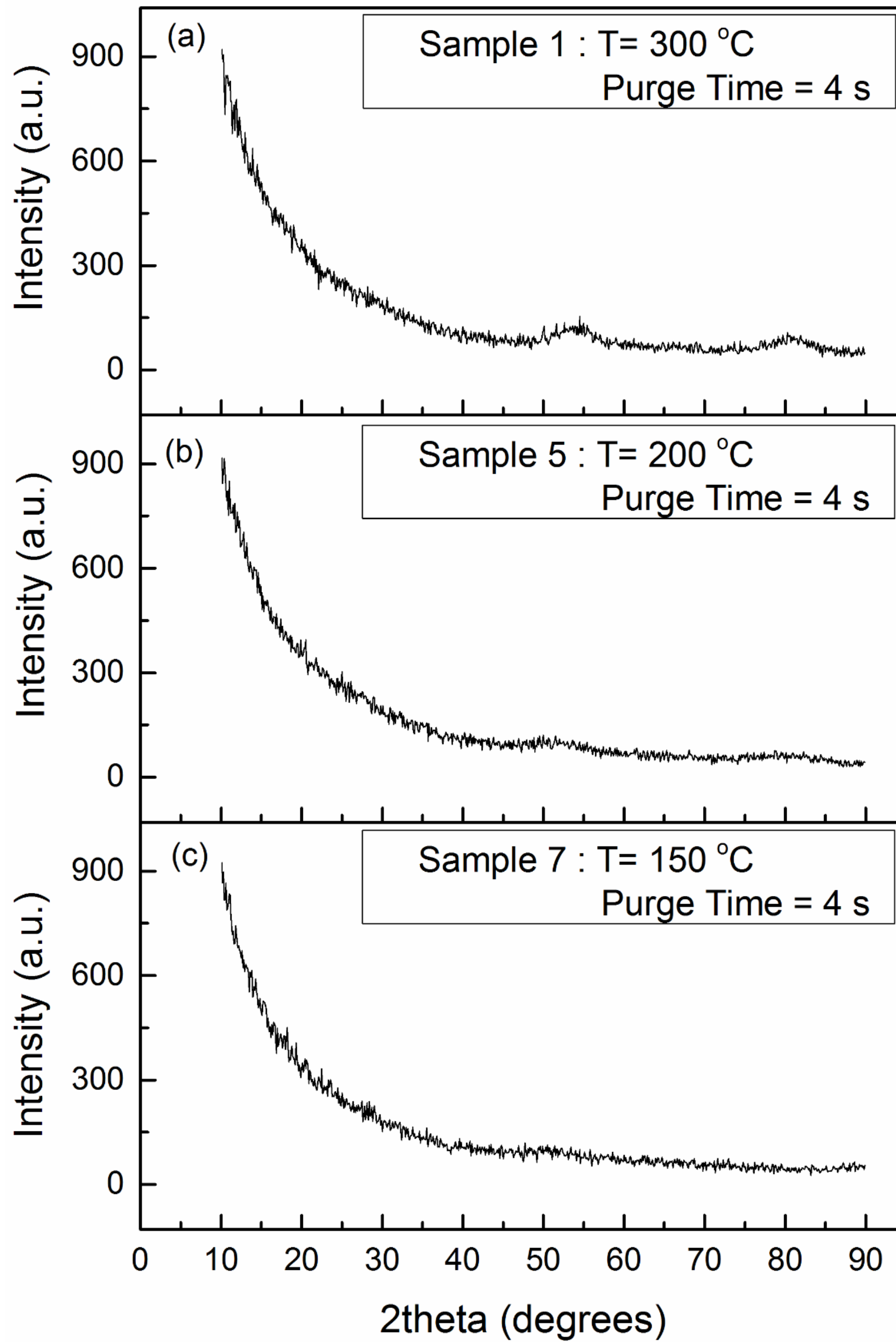

Figure 3.11 XRD pattern of selected samples

3.4. Micro-Raman Investigation

3.4.1. Basic Theory of Raman Spectroscopy

Raman spectroscopy is an optical chemical analysis technique that measures the intensity of inelastically scattered light over a range of frequencies. During the Raman scattering process, a small portion of the incident photons (1 in 10^6-10^7) are

ANADOLU ÜNİVERSİTESİ

scattered inelastically due to their interaction with the vibrations or rotations of atoms or molecules. The inelastic exchange occurs because the photons either loose or gain energy from the material under examination. In the case of the solid state lattice of silicon for example, the photons scatter due to their interaction with lattice vibrations (phonons). The inelastic scattering is a result of a red frequency shift of the scattered photon to longer wavelengths (Stokes scattering) or shorter wavelengths (anti-Stokes scattering) [124].

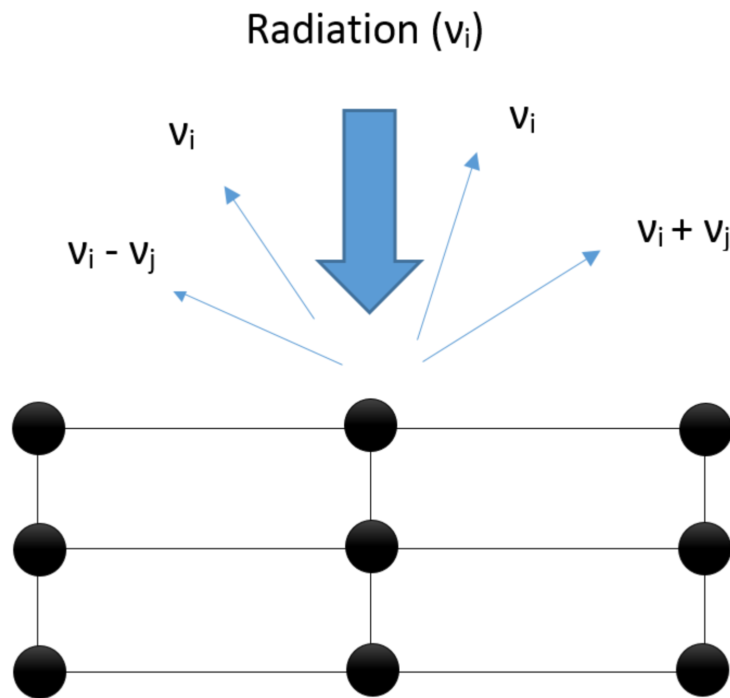

Figure 3.12 Diagram of the Raman and Rayleigh scattering processes

Visualization of Raman light scattering is shown in Figure 3.12. In the case of the Stokes shift, an incident photon at frequency ν_i loses energy to the lattice from which it is scattered (ν_i-ν_j), while a photon gains energy from the lattice during the anti-Stokes instance (ν_i+ν_j).

3.4.2. Micro-Raman System Hardware

A typical micro-Raman system consists of a microscope and stage, excitation laser, filters, slit, diffraction grating, necessary optics, detector, and post-processing software which are shown in Figure 3.13 [124]. Confocal microscopy requires a

ANADOLU ÜNİVERSİTESİ

point source (usually a laser), which is focused onto the sample. The reflected light (Raman, fluorescence) is collected with the same objective and focused through a pinhole at the front of the detector. This ensures that only light from the image focal plane can reach the detector, which greatly increases image contrast and with the proper selection of pinhole size, slightly increases resolution (max. gain in resolution: factor √2).

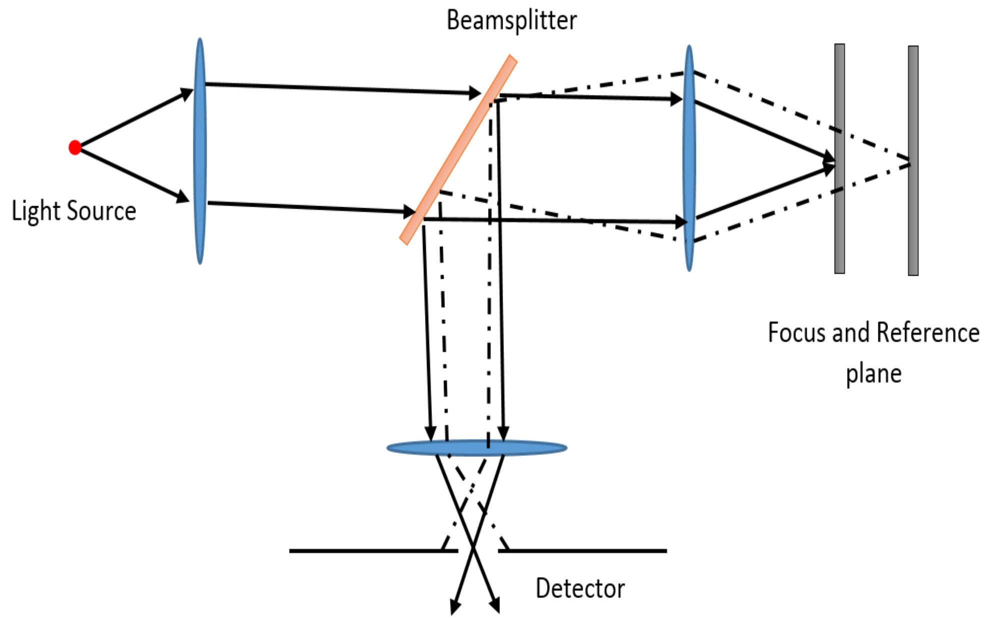

Figure 3.13 Typical Components of a micro-Raman System

The condition given in Equation (3.4):

$$\frac{M}{NA} \geq \frac{\pi d_0}{\lambda\,\vartheta_{Pmax}} \tag{3.4}$$

must be fulfilled, where M is the magnification, d_0 the diameter of the pinhole, ϑ_{Pmax} maximum size of the pinhole and the numerical aperture (NA) of the objective. In Table 3.4, the parameter $\frac{M}{NA}$ is calculated for several typical objectives.

Table 3.4 M/NA for different objectives

Objective	**10/0.25**	**20/0.4**	**40/0.6**	**60/0.8**	**100/0.9**
$\boldsymbol{M/NA}$	53	50	67	75	111

ANADOLU ÜNİVERSİTESİ

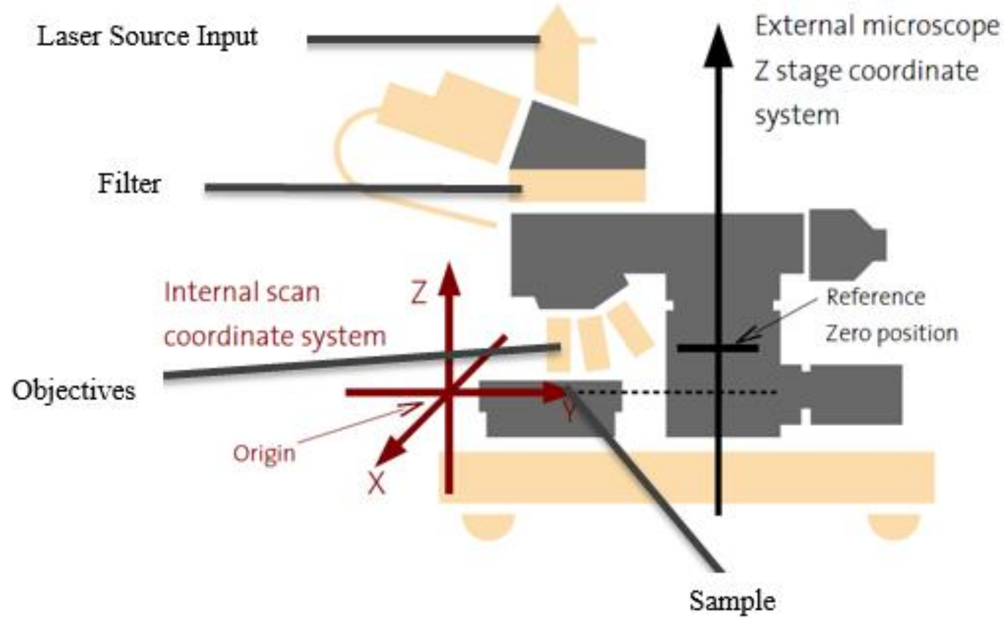

Figure 3.14 Schematic representation of Micro-Raman spectrometer [125]

Schematic illustration of Confocal Raman spectrometer is shown in Figure 3.14. Micro-Raman system was equipped with a Nd-YAG laser source (532 nm). Micro-Raman spectrum was obtained by using a WITEC Alpha 300S Confocal Raman systems. The spectrum resolution was 5 cm^{-1} and recorded over the range of 50 to 3000 cm^{-1}. The intensity was kept at minimum to avoid laser induced heating. Integration time and accumulation were kept at 0.5 seconds and 20 times, respectively.

3.4.3. Experimental Results

The general characteristics of the Raman spectra are very similar for all sample. This occurs because of low polarizability of light atoms and the ionic character of the AI-O bonds (Raman-inactive) [126]. Moreover, the observed Raman intensities were different. These intensity differences occur because of thickness variation of each sample. The focused laser of the Raman system detects radiation also from the substrate due to grown small thickness of the films (~50-60 nm). As a natural result of this, the detected radiation decreased with increasing the thickness of samples or vice versa. In previous section temperature effect was given

ANADOLU ÜNİVERSİTESİ

in Figure 3.4. In agreement with the results in Figure 3.15, “Sample 1” had lowest thickness (~54 nm) and consequently resulted in highest intensity. The same trends were observed for “Sample 5” and “Sample 7”. For example, “Sample 5” (~60 nm) had highest thickness and it had lowest intensity. These intensity difference of each samples were shown in Figure 3.15.

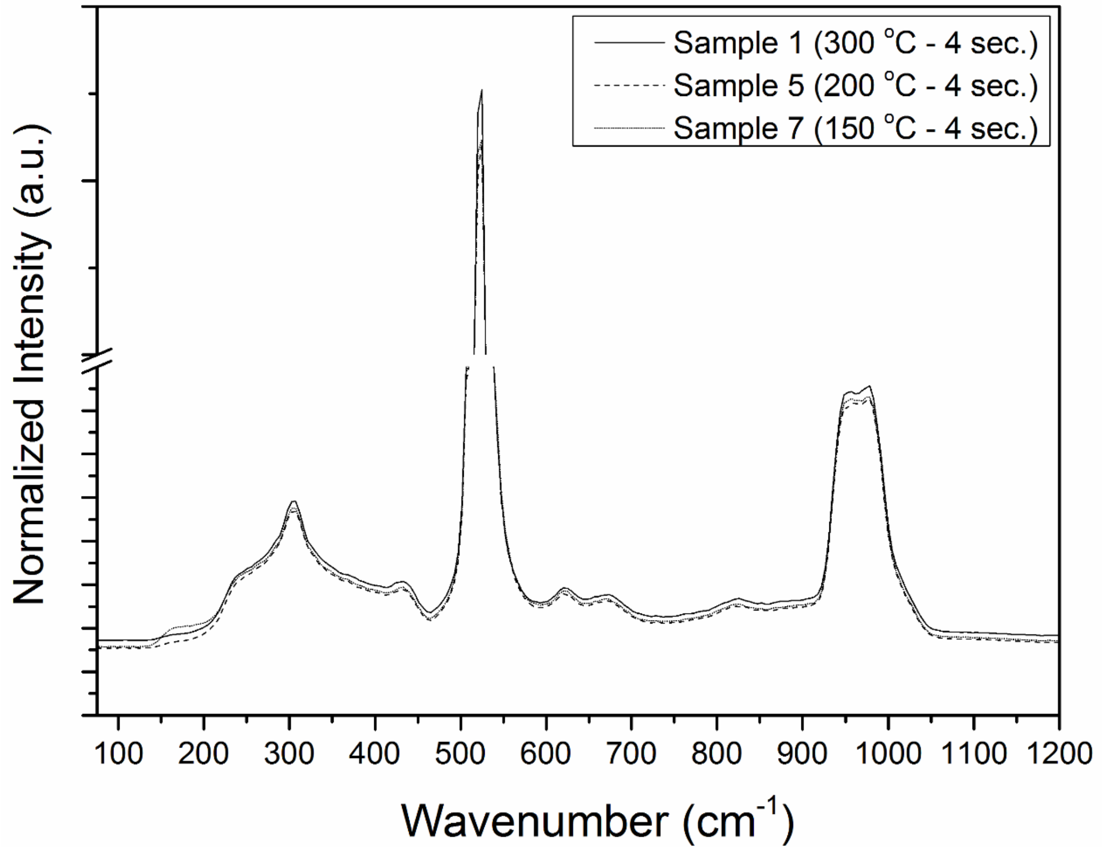

Figure 3.15 Micro Raman results of selected samples

The observed vibrations are identified to be as given in Table 3.5. The absence of Al_2O_3 peaks in Table 3.5 indicates that the material is amorphous. The corresponding X-ray diffraction results showed too broad and weak peaks consistent with Micro-Raman results. Therefore Micro-Raman and XRD results the amorphous structure of the grown Al_2O_3 films [127, 128, 129].

ANADOLU ÜNİVERSİTESİ

Table 3.5 Raman vibrations observed in the grown Al_2O_3

Vibrations	Peak Frequency (cm^{-1})			Ref.
	Sample 1	Sample 5	Sample 7	
(1) c-Si (TA)	165,2	165,7	172,4	[130, 131]
(2) SiO_2	250,2	249,0	249,7	[132]
(3) c-Si (2TA)	303,4	303,2	304,2	[133]
(4) c-Si LO	350,1	354,8	354,9	[134]
(5) Si-Si	434,5	434,7	434,3	[135]
(6) c-Si (TO)	522,7	522,7	522,7	[133]
(7) Si-O-Si	617,8	615,8	616,2	[136]
(8) SiO_2	667,9	668,4	668,0	[132]
(9) SiO_2	820,4	820,5	819,7	[132]
(10) Si-O-Si	873,6	873,2	873,5	[136]
(11) c-Si (2TO)	~908 to 1045	~906 to 1047	~904 to 1048	[133]
(12) c-Si (2TO + TA)	~1040 to1150	~1040 to1150	~1040 to1150	[134]
(13) a-C:H	~1444	~1448	~1445	[137, 138]
(14) c-Si (3TO)	~1400 to1960	~1400 to1960	~1400 to1960	[134]

All spectra show dominant vibration peak at ~520 cm^{-1} which is attributed to the transverse optical (TO) phonon vibrations of c-Si substrate. Two transverse acoustical (2TA) and two transverse optical (2TO) phonon vibrations are also dominant at ~300 and 910 to 1040 cm^{-1}, respectively. Moreover, SiO_2 and Si-O-Si vibrations were observed due to natural oxide layer that is probably present at the Si-Al_2O_3 interface. Broad and weak peaks at frequency of 1040 to 1150 and 1400 to 1960 cm^{-1} can be assigned to 2TA + TO and three transverse optical (3TO) of c-Si, respectively. Furthermore, a-C:H bond vibration is at the limit of detection at the range from ~ 1300 to 1550 cm^{-1}. In the spectra it is barely observable, nonetheless, it shows the presence of a-C:H for all samples. As a comment for a-C:H intensity at all samples, the concentration of a-C:H decreases with increasing

ANADOLU ÜNİVERSİTESİ

the temperature for this study. It will be further investigated using FTIR (Fourier Transform Infrared Spectroscopy) and XPS (X-Ray Photoelectron Spectroscopy) techniques in the later stages of the study.

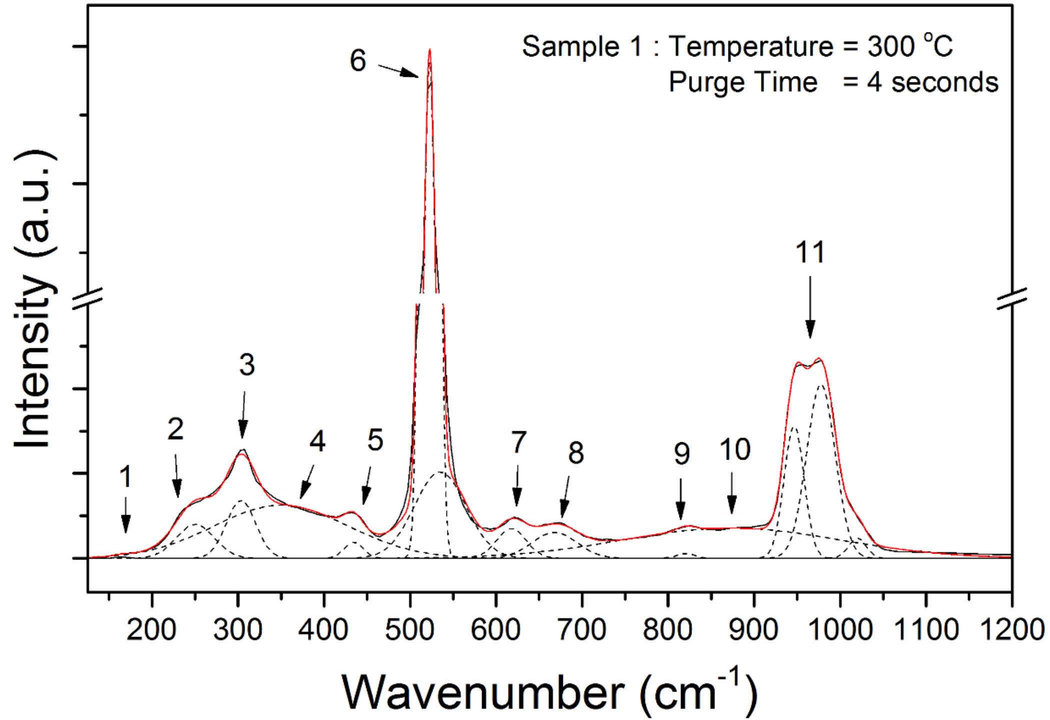

Figure 3.16 Micro-Raman results of Al_2O_3 layers and fitted peaks of Sample 1

Micro-Raman spectroscopy graph of an Al_2O_3 film grown of "Sample 1" and fitted peaks are presented in Figure 3.16. TA, TO, 2TO and 2TA phonon vibration peaks of c-Si are identified to be at 165, 522, 908 to 1045 and 303 cm^{-1}, respectively [133]. Due to p-type doping of c-Si substrate, the asymmetric TO peak was observed [139]. Weak bands at about 250 cm^{-1}, 667 and 820 cm^{-1} indicates presence of SiO_2 [132] and also peak at 434 cm^{-1} can be correlated with Si-Si local bonds [135]. Band with two maxima 617 and 873 cm^{-1} are related to Si-O-Si vibrations [136]. Too board and weak band at limit of detection at 1444 cm^{-1} indicates possibly presence of a-C: H in the film [137, 138]. Moreover, third-order spectrum features; the 1400-1960 cm^{-1} band is ascribed to 3TO scattering and the 1040-1150 cm^{-1} to 2TO + TA [134].

ANADOLU ÜNİVERSİTESİ

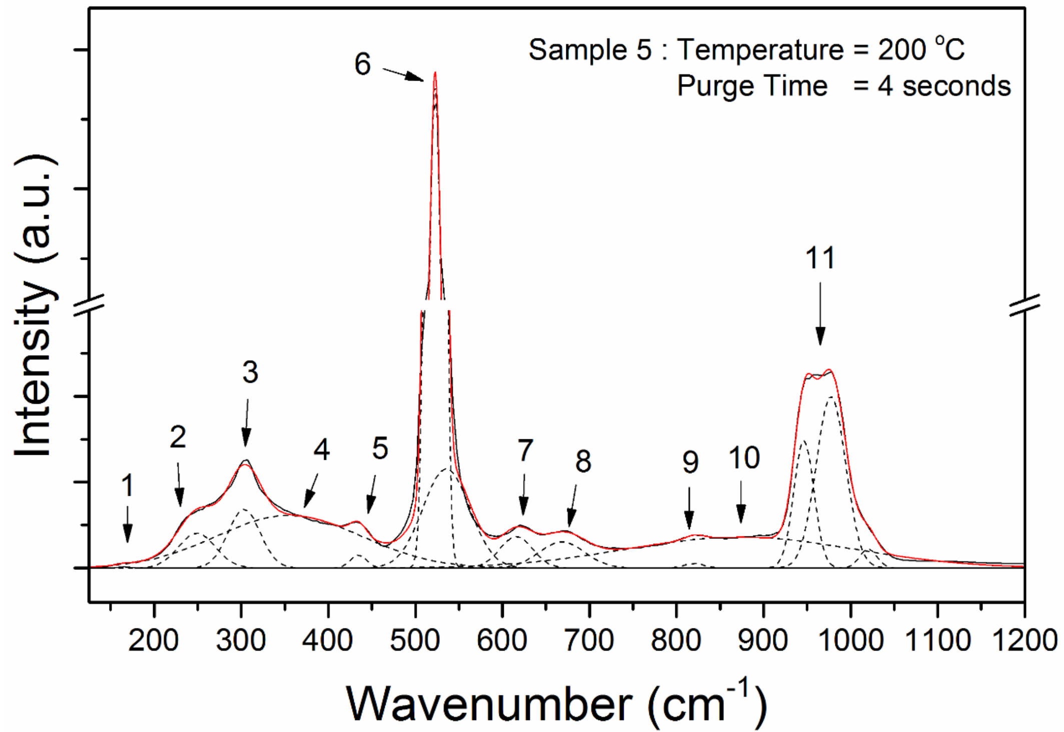

Figure 3.17 Micro-Raman results of Al_2O_3 layers and fitted peaks of Sample 5

Micro-Raman and fitting results of "Sample 5" is shown in Figure 3.17. The all peaks can be correlated with same vibrational modes of "Sample 1", although slightly offset at peaks points. Similarly, TA, TO, 2TO and 2TA phonon vibration peaks of c-Si are identified to be at 165, 522, 906 to 1047 and 303 cm^{-1}, respectively [133]. Weak bands at about 249 cm^{-1}, 668 and 820 cm^{-1} indicates presence of SiO_2 [132] and also peak at 434 cm^{-1} can be correlated with Si-Si local bonds [135]. Band with two maxima 615 and 873 cm^{-1} are related to Si-O-Si vibration [136]. Too board and weak band at limit of detection at 1448 cm^{-1} indicates presence of a-C: H in the film [137, 138]. Again, third-order spectrum features; the 1400-1960 cm^{-1} band is ascribed to 3TO scattering and the 1040-1150 cm^{-1} to 2TO + TA [134].

ANADOLU ÜNİVERSİTESİ

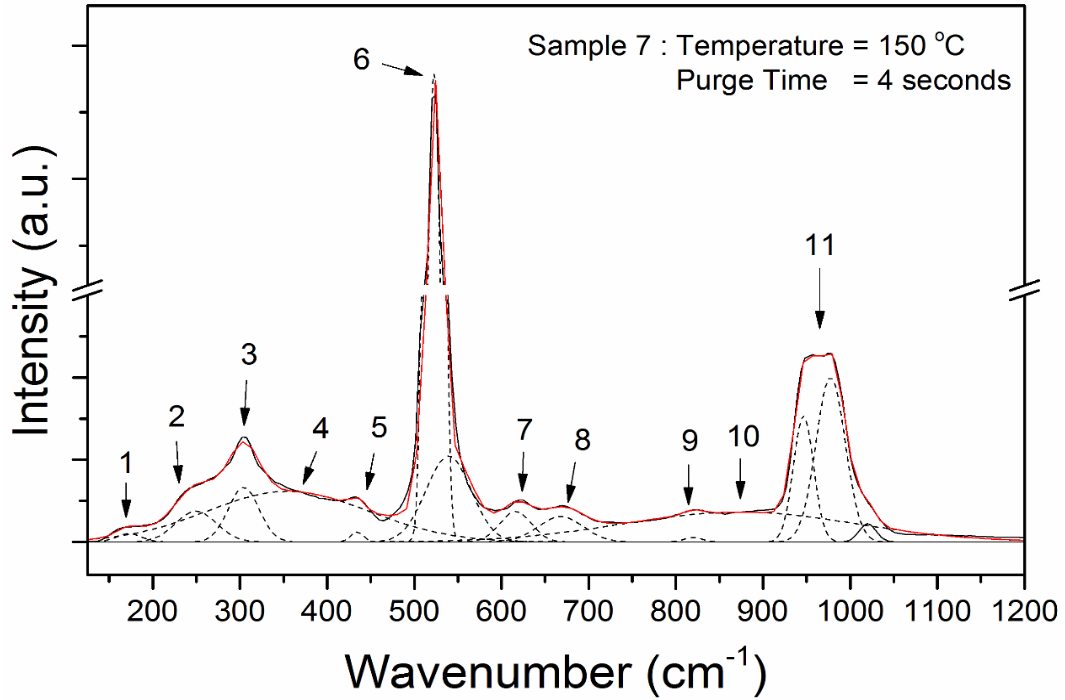

Figure 3.18 Micro-Raman results of Al_2O_3 layers and fitted peaks of Sample 7

In Figure 3.18, Micro-Raman spectrum of "Sample 7" is given. TA, TO, 2TO and 2TA phonon vibration peaks of c-Si are identified to be at 172, 522, 904 to 1048 and 304 cm^{-1}, respectively [133]. Weak bands at about 249 cm^{-1}, 668 and 819 cm^{-1} indicates presence of SiO_2 [132] and also peak at 434 cm^{-1} can be correlated with Si-Si local bonds [135]. Band with two maxima 616 and 873 cm^{-1} are related to Si-O-Si vibrations [136]. Too board and weak band at limit of detection at 1448 cm^{-1} indicates presence of a-C: H in the film [137, 138]. Lastly, third-order spectrum features; the 1400-1960 cm^{-1} band is ascribed to 3TO scattering and the 1040-1150 cm^{-1} to 2TO + TA [134].

In conclusion, the growth of the Al2O3 layers at higher temperatures and low purge time possibly results in denser film and lower a-C:H bond concentrations. It must be noted, that Al-O vibrations are not clearly observable because of the low polarizability of light atoms and the ionic character of the AI-O bonds [126] . Moreover, thickness variation of the samples causes the intensity difference of the each spectrum. Lastly, fitting results which is full width half maximum (FWHM), center gravity and integrated area of each spectrum is tabulated in detail in Table 3.6.

ANADOLU ÜNİVERSİTESİ

Table 3.6 Fitting results of selected samples

Vibration Peaks	Center Gravity			FWHM			Integrated Area		
	Sample 1	Sample 5	Sample 7	Sample 1	Sample 5	Sample 7	Sample 1	Sample 5	Sample 7
Peak (1)	165,2 ± 7,8	165,7 ± 6,6	172,4 ± 3,8	19,2 ± 2,1	16,0 ± 1,7	33,5 ± 6,2	1,5 ± 1,8	1,12 ± 1,3	18,1 ± 5,0
Peak (2)	250,2 ± 9,8	249,0 ± 8,4	249,7 ± 7,4	51,8 ± 3,1	50,3 ± 2,3	55,2 ± 3,8	110,5 ± 10,1	108,4 ± 7,2	110,2 ± 12,7
Peak (3)	303,3 ± 5,1	303,2 ± 4,66	304,2 ± 6,6	40,1 ± 10,9	43,4 ± 9,9	41,6 ± 13,7	157,9 ± 50,7	145,3 ± 59,1	147,2 ± 76,5
Peak (4)	350,0 ± 23,7	354,8 ± 18,2	354,8 ± 33,76	184,7 ± 45,9	196,2 ± 32,8	219,9± 64,4	720,2 ± 40,5	615,1 ± 39,4	639,7 ± 33,3
Peak (5)	434,4 ± 6,9	434,7 ± 6,7	434,3 ± 10,4	25,6 ± 2,2	21,9 ± 1,9	17,2 ± 2,8	25,8 ± 2,9	11,0 ± 1,9	17,5 ± 1,9
Peak (6)	522,67 ± 0,03	522,69 ± 0,02	522,7 ± 0,03	15,88 ± 0,08	15,84 ± 0,07	16,22 ± 0,11	3281,7 ± 23,8	3147,4 ± 21,8	3268,1 ± 30,7
Peak (7)	617,7 ± 11,4	615,8 ± 11,1	616,2 ± 14,3	40,2 ± 24,2	44,3 ± 22,9	42,6 ± 29,7	86,7 ± 7,4	74,8 ± 7,9	84,1 ± 9,7
Peak (8)	667,8 ± 22,1	668,4 ± 20,2	667,9 ± 13,7	61,3 ± 4,3	61,3 ± 3,8	60,8 ± 5,2	100,0 ± 8,9	95,0 ± 8,2	99,2 ± 11,0
Peak (9)	820,3 ± 23,2	820,5 ± 20,2	818,1 ± 26,6	25,1 ± 5,9	26,1 ± 5,2	25,2 ± 6,7	7,48 ± 2,0	7,2 ± 1,7	7,4 ± 1,4
Peak (10)	873,5 ± 22,7	873,2 ± 19,8	873,5 ± 27,7	298,7 ± 45,5	311,7 ± 39,9	316,4 ± 56,2	613,1 ± 9,5	566,1 ± 77,5	596,8 ± 67,4
Peak (12)	946,3 ± 3,5	946,2 ± 3,0	946,4 ± 4,1	27,3 ± 5,0	27,3 ± 4,4	27,3 ± 6,0	227,2 ± 10,9	215,6 ± 9,3	222,3 ± 13,1
	977,5 ± 4,0	977,3 ± 3,6	977,5 ± 5,1	39,2 ± 10,4	39,9 ± 8,9	39,6 ± 12,5	427,4 ± 12,6	422,1 ± 15,3	424,6 ± 10,6
	1019,9 ± 9,1	1020,1 ± 7,65	1020,0 ± 10,8	23,9 ± 1,9	23,0 ± 1,6	23,1 ± 2,3	30,3 ± 3,2	26,9 ± 2,5	27,1 ± 3,6

3.5. Fourier Transform Infrared Spectroscopy (FTIR)

To support our conclusions drawn from XRD and Micro-Raman results of Al_2O_3 films, a systematic IR studies has been carried out. Moreover, is the FTIR method provides additional information about the internal structure and composition of the grown layers. Firstly, background theory will be given, then the experimental setup will be described, and finally the obtained spectra for selected samples will be presented.

3.5.1. Background Theory and Molecular Vibrations

Infrared spectroscopy, or IR, is a characterization technique that makes use the vibrations of atoms of a molecule. The IR spectrum is mainly a graph of infrared absorbance, transmittance or reflectance. The spectrum data collected by having infrared radiation passing through a sample and determining the absorbed, transmitted or reflected features at a particular energy [140]. The energy at which any peak in any type of spectrum appears corresponds to the frequency of a vibration of a part of a molecule in the sample. Therefore, IR spectroscopy is a very powerful technique which provides fingerprint information on the chemical composition of the sample. The vibrations of molecules will be describe shortly, as these are crucial to the interpretation of infrared spectra [140].

There are two types of fundamental molecular vibrations, stretching which is change in inter-atomic distance along bond axis and bending which is change in angle between two bonds. There are also two different stretching vibrations which are symmetric and asymmetric. Moreover, bending vibrations have four different types which are rocking, scissoring, wagging and twisting. Some of these vibrations are illustrated in Figure 3.19.

ANADOLU ÜNİVERSİTESİ

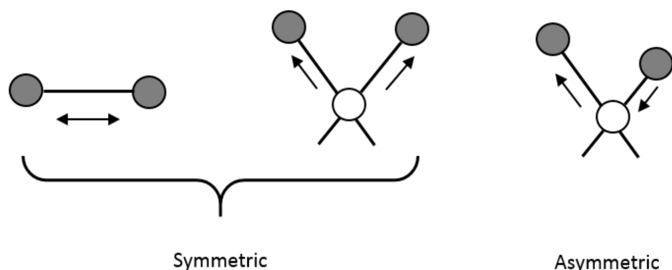

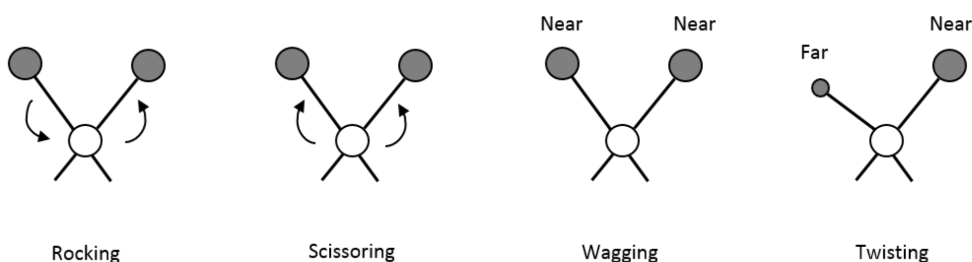

Figure 3.19 Schematics of major vibrational types [141]

A molecule which consist of *n* atoms has total of *3n* degrees of freedom. For a nonlinear molecule, rotational and translational have 3 of these degrees and the remaining correspond to fundamental vibrations, or called as normal modes. In a linear molecule, 2 degrees of freedom are rotational and 3 are translational and again the remaining correspond to normal modes [141]. The degrees of freedom for polyatomic molecules are summarized in Table 3.7.

Table 3.7 The degrees of freedom for polyatomic nonlinear and linear molecules [141]

Type of degrees of freedom	**Nonlinear**	**Linear**
Translation	3	3
Rotational	3	2
Vibrational	3n-6	3n-5
Total	3n	3n

Moreover, a diatomic molecule has only a stretching motion which can be nonlinear or linear. Furthermore, a non-linear triatomic molecule such as X–Y–X type has three normal modes, two of which correspond to stretching vibrations, the

ANADOLU ÜNİVERSİTESİ

other corresponding to a bending vibration. Similar triatomic molecule for linear type has four normal modes, two of which correlated with stretching vibrations, and the other two vibration can be different types of scissoring vibrations [140]. Illustration of normal modes for nonlinear and linear triatomic molecules are shown in Figure 3.20.

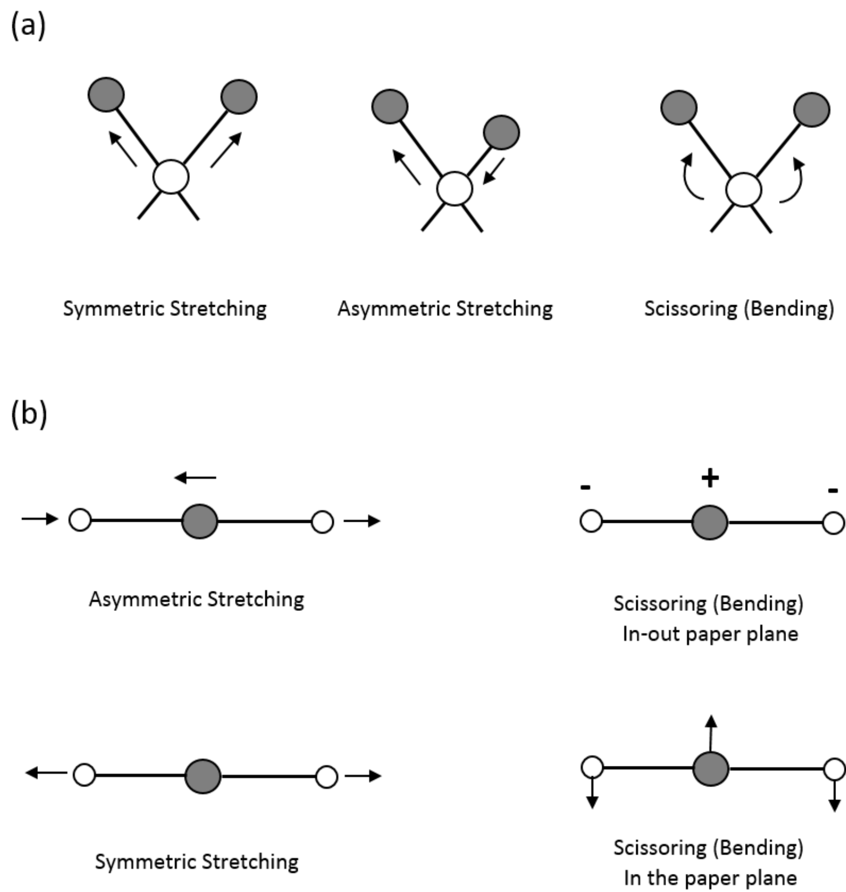

Figure 3.20 Illustration of normal modes for (a) nonlinear and (b) linear polyatomic molecule [141]

The molecule transition occurs between $0 \rightarrow 1$ potential energy levels for harmonic oscillator, called as normal mode vibrational frequency, however, if the molecule transition occurs from $0 \rightarrow x$ ($x > 1$) potential energy levels, it is called as overtone vibration. It must be mentioned that, we can have *overtone vibrations*. In addition, for polyatomic molecules there can be further *combination bands* which come about from two different modes of vibration and add together to show up at higher energy level. That is, in this transition one photon excites two different vibrations simultaneously [142].

ANADOLU ÜNİVERSİTESİ

3.5.2. Hardware Setup

The infrared absorbance measurements reported in this thesis were performed using a Bruker Vertex 70v Fourier transform IR spectrometer. The spectrometer is based on a Michelson interferometer, shown schematically in Figure 3.21. The collimated light from an IR source impinges on a beam-splitter which reflects 50%

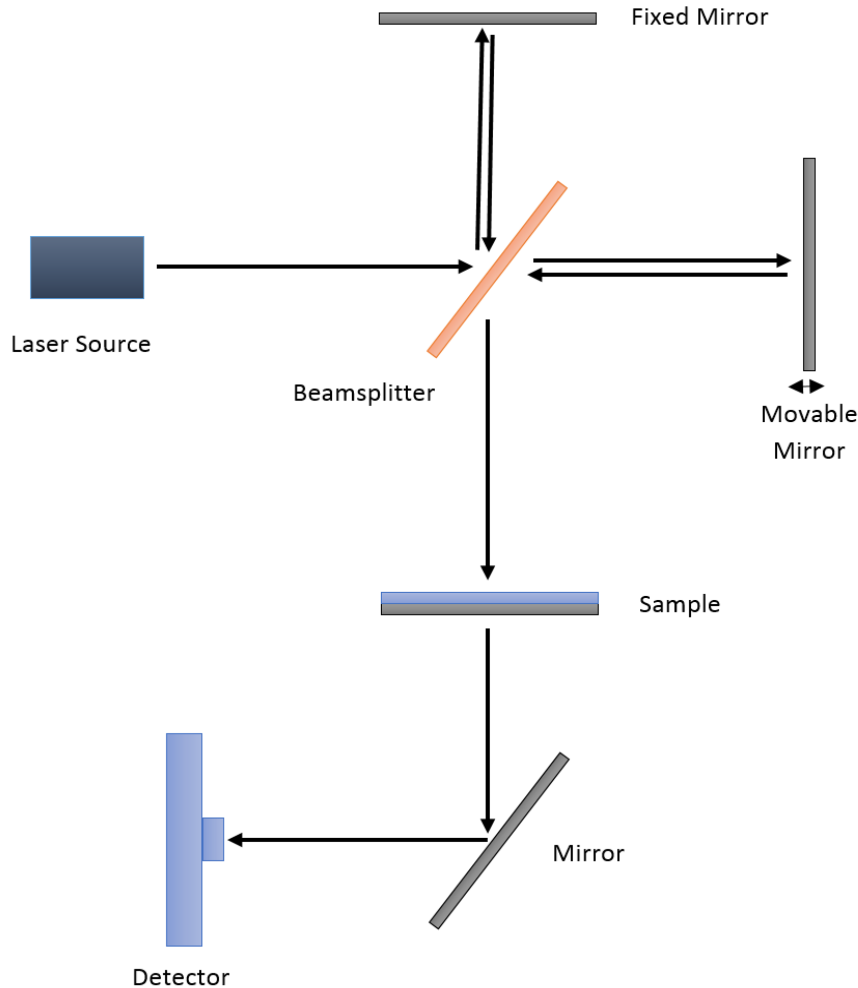

Figure 3.21 Schematic of FTIR setup with Michelson interferometer

of the light and transmits the remaining part. The reflected light hits a fixed mirror where it is reflected again, while the transmitted part of the beam is reflected by a moveable mirror. The reflected beams recombine again at the beamsplitter, which allows half of the light pass through and reflects the other portion of the light to a detector. The resulting pattern of the two superimposed beams is known as an interferogram [143, 144].

ANADOLU ÜNİVERSİTESİ

The IR absorbance data to be presented in the next section, are collected for a spectral range. This range is accessed using a mid-infrared source, potassium bromide (KBr) beam-splitter and liquid nitrogen cooled mercury cadmium telluride (MCT) detector. Background scan was fixed at 16 times and sample scan was fixed at 50 times and the resolution of the spectrum at 4 cm^{-1}. All measurements were performed at room temperature and at atmospheric pressure. A PC with commercial software (OPUS) is used to record the FT-IR spectra collected by the spectrometer.

3.5.3. Experimental Results

After describing the theoretical background and experimental setup, the IR spectra of selected samples are presented in this section. Baseline correction was applied to all the spectra. The second order Savitzkty-Golay algorithm, which is the most typical smoothing filter for IR spectral curves, is applied to the all spectra [145]. Then the Gaussian fitting was performed for peak decomposition. Before collecting IR absorbance spectrum background scanning was performed with a reference sample, described in the sample preparation section. Thus, the effects of the substrate and air are eliminated from the spectrum, only the spectrum due to the grown layers remains.

ANADOLU ÜNİVERSİTESİ

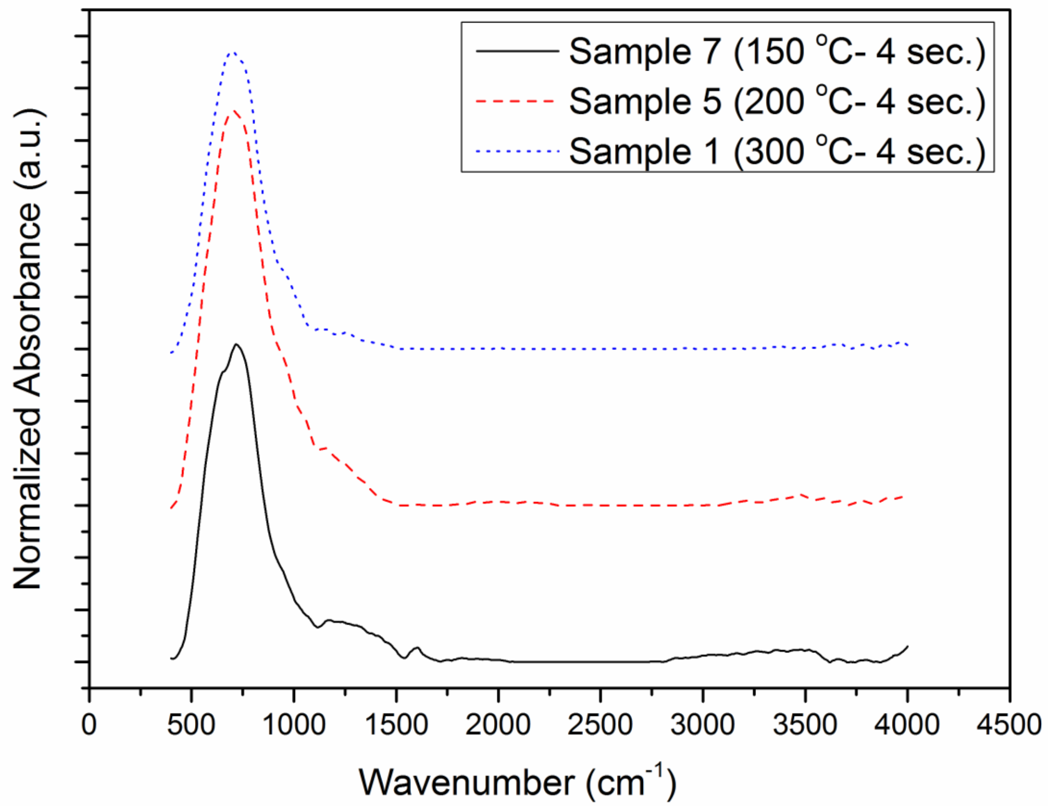

Figure 3.22 FTIR absorbance results of 300 ºC with purge time of 4 seconds (Sample 1), 200 ºC with purge time of 4 seconds (Sample 5) and 150 ºC with purge time of 4 seconds (Sample 7)

Measured FTIR spectra of selected samples is given in Figure 3.22. Consistent with the thicknesses of the deposited films which were given in Table 3.3, "Sample 5" which is the thick sample has maximum absorbance [146]. Moreover, all samples shows dominant character at the range of ~ 400 to 1000 cm^{-1} which is assigned to the characteristic absorption band of amorphous Al_2O_3 [146]. This strong and board absorption band consists of several peaks possibly that are $Al\text{-}O_6$ (octahedra vibrations), $Al\text{-}O_4$ (tetrahedra vibrations), Al-O (LO stretching) [147]. Furthermore, it must be mentioned that OH and carboxyl group contamination decreases with increasing the growth temperature.

ANADOLU ÜNİVERSİTESİ

Table 3.8 FTIR absorbance vibrations observed in the selected samples

Vibrations	Peak Frequency (cm^{-1})			Ref.
	Sample 1	Sample 5	Sample 7	
(1) Al-O_6 (octahedra bending)	480	483	485	[148]
(2) Al-O_6 (octahedra stretching)	601	582	587	[148, 149]
(3) Al-O_4 (tetrahedra bending)	742	731	735	[149]
(4) Al-O (LO stretching)	971	960	962	[147]
(5) Al-O_4 (tetrahedra stretching)	1141	1160	1165	[149]
(6) Al-OH (bending)	1260	1194	1238	[150]
(7) CH_2 (bending)	-	-	1423	[151]
(8) O-H (bending)	-	-	1602	[152]
(9) C-O (stretching)	-	-	~ 1800 to 2100	[153, 154]
(10) CH_2 (stretching)	-	-	~ 2700 to 3100	[146, 154, 155]
(11) O-H (stretching)	~ 3000 to 3700			[146, 147, 152, 155]

Table 3.7 lists the identified absorbance peaks. The most relevant being: the characteristic absorption band of Al_2O_3 which possibly contain the modes of (1) Al-O_6 (octahedra bending) at 480 - 485 cm^{-1} [148], (2) Al-O_6 (octahedra stretching) at 582 - 601 cm^{-1} [148, 149], (3) Al-O_4 (tetrahedra bending) at 731 - 742 cm^{-1} [149], (4) Al-O (LO stretching) at 960 – 971 cm^{-1} [142], (5) Al-O_4 (tetrahedra stretching) at 1041 - 1065 cm^{-1}, [149], (6) Al-OH (bending) at 1194 – 1260 cm^{-1} [150], (7) CH_2 (bending) at 1423 cm^{-1} [151], (8) O-H (bending) at 1604 cm^{-1} , [151], (9) C-O

ANADOLU ÜNİVERSİTESİ

(stretching) ~1800 to 2100 cm^{-1} [153, 154], (10) CH_2 (stretching) at ~2700 to 3100 cm^{-1} [146, 154, 155], lastly (11) O-H (stretching) at ~ 3000 to 3700 cm^{-1} [146, 147, 152, 155] common for all selected samples.

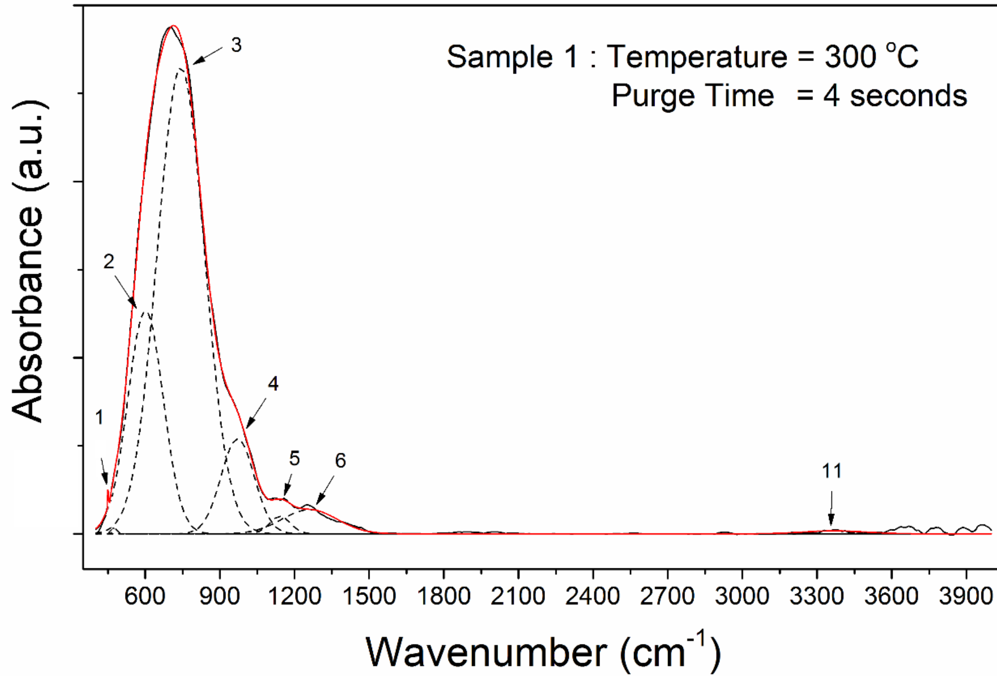

Figure 3.23 FTIR absorbance results of Al_2O_3 layers and fitted peaks of Sample 1

Figure 3.23 shows the spectrum of “Sample 1”. Absorbance was normalized according to thickness value of “Sample 1”. The peak of 480, 601, 742, 971, 1141 and 1260 cm^{-1} can be assigned to (1) Al-O_6 (octahedra bending), (2) Al-O_6 (octahedra stretching), (3) Al-O_4 (tetrahedra bending), (4) Al-O (LO stretching) and (5) Al-O_4 (tetrahedra stretching) (6) Al-OH (bending) at the range of 400 to 1300 cm^{-1}, respectively. Broad peak at 3000 to 3700 cm^{-1} indicates the presence of (11) O-H (stretching) vibrations.

ANADOLU ÜNİVERSİTESİ

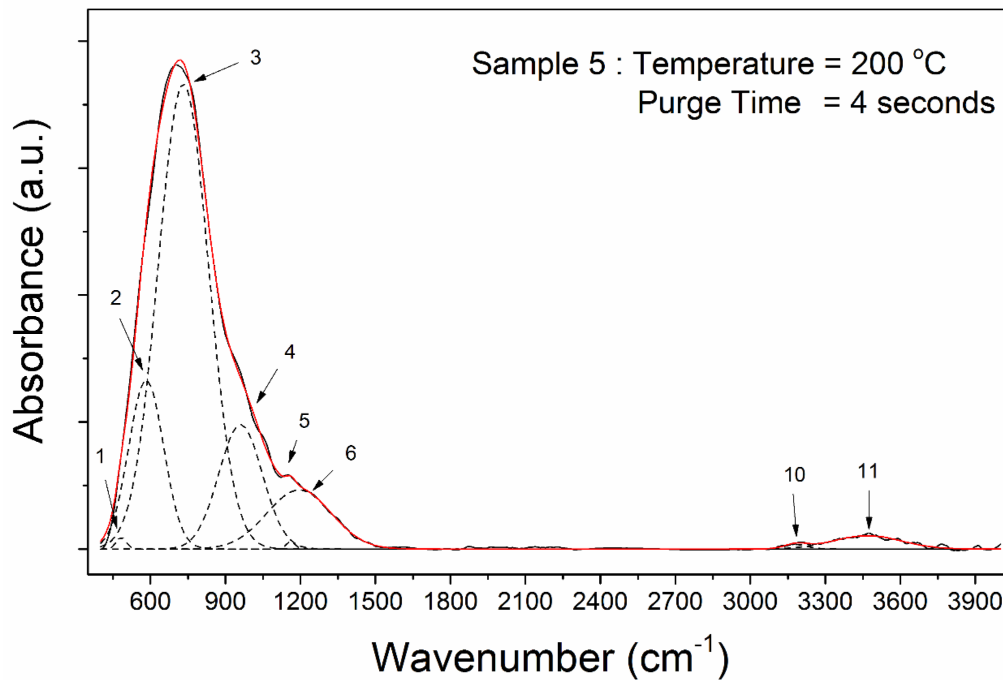

Figure 3.24 FTIR absorbance results of Al_2O_3 layers and fitted peaks of Sample 5

The IR spectrum of "Sample 5" is given in Figure 3.23. Substrate and air effect are eliminated by subtracting the background scan and thickness normalization is applied according to "Sample 5". The integrated area of (11) O-H (stretching) increases and (10) CH_2 (stretching) appears. This observation means that the impurity level is high compare with "Sample 1". The other peaks can be correlated with same vibrational modes of "Sample 1", although slightly offset at peaks points.

In Figure 3.25, IR spectra of "Sample 7" is given. Compare with the "Sample 1" and "Sample 5", the peaks of (7) CH_2 (bending) at 1423 cm^{-1}, (8) O-H (bending) at 1602 cm^{-1}, (9) C-O (stretching) at ~1800 to 2100 cm^{-1} and (10) CH_2 (stretching) at 2700 to 3100 cm^{-1} appears. (7) and (10) possibly occurs due to the activation energy of TMA. It is explained at the beginning of the section in detail. Moreover, the appearance of the (9) possibly due to the FTIR detector. Moreover, the integrated area of (8) O-H (stretching) at 1602 cm^{-1} and (11) O-H (stretching) increased. These observation means that the impurity level is high compare with "Sample 1" and "Sample 5". The other peaks can be correlated with same vibrational modes of "Sample 1" and "Sample 5", although slightly offset at peak points.

ANADOLU ÜNİVERSİTESİ

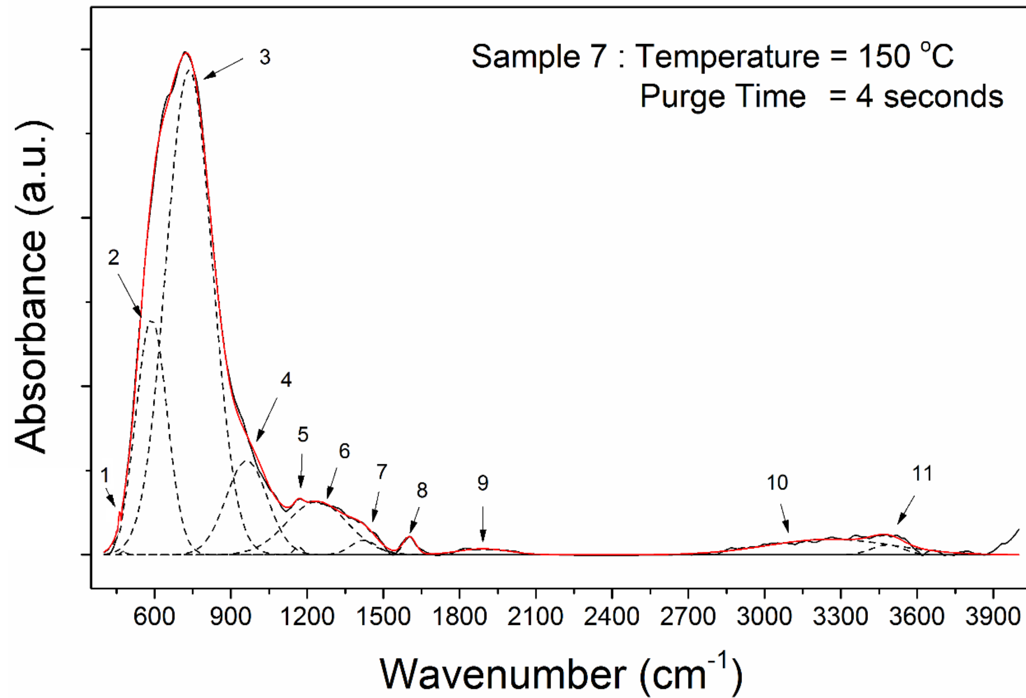

Figure 3.25 FTIR absorbance results of Al_2O_3 layers and fitted peaks of Sample 7

In micro-Raman results, the radiation is coming from the substrate and the grown Al_2O_3 restricts the radiation. Thus, the thick sample (Sample 5) had low intensity. In FTIR results, the substrate effect is subtracted from the spectrum and only grown layer is analyzed. In direct proportion with this, the integrated area of the vibrations is increasing with increasing the thickness. This trend can be clearly seen in Figure 3.27 which contains the integrated area of relevant Al-O vibration common to “Sample 1”, “Sample 5” and Sample 7. In all vibration integrated area, “Sample 5” (200 C purge time of 4 seconds) has the largest area because it is the thick sample compare with “Sample 1” and Sample 7. Another common trend is “Sample 1” has the lowest integrated area for given vibration in Figure 3.27. It again occurs because of the thickness of “Sample 1”.For O-H (stretching) vibrations, the case is different. Although the “Sample 5” have the maximum thickness, Sample 7 has the highest integrated area of O-H (stretching) vibrations. The grown layers possibly has more OH contamination at low temperature. This also explains the behavior of the samples which grown at low temperatures has high thickness.

ANADOLU ÜNİVERSİTESİ

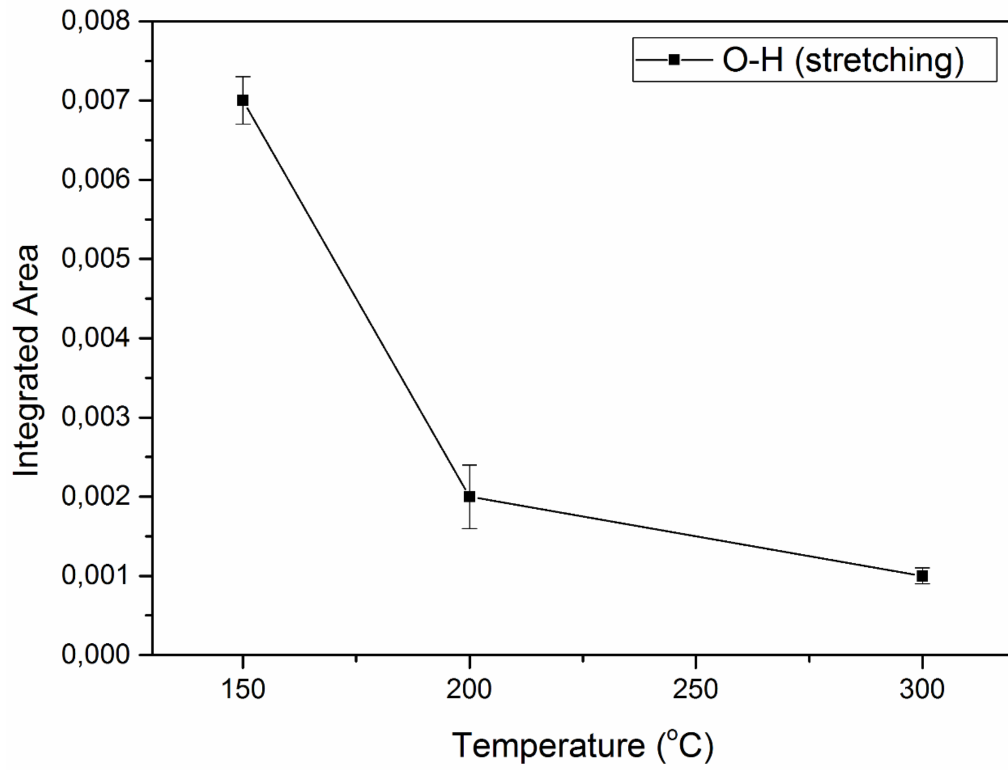

Figure 3.26 The integrated area of O-H (stretching) vibration of selected samples

As a result, unlike Micro-Raman results, modes of Al_2O_3 is clearly observable in IR spectroscopy at range of 400 to 1000 cm^{-1}. In agreement with the thicknesses, intensity variation of IR spectra of each sample is emphasized. Moreover, OH and carboxyl groups which are basis of optical losses decreased with increasing the growth temperature.

ANADOLU ÜNİVERSİTESİ

Figure 3.27 The integrated area of Al-O vibrations common to selected samples

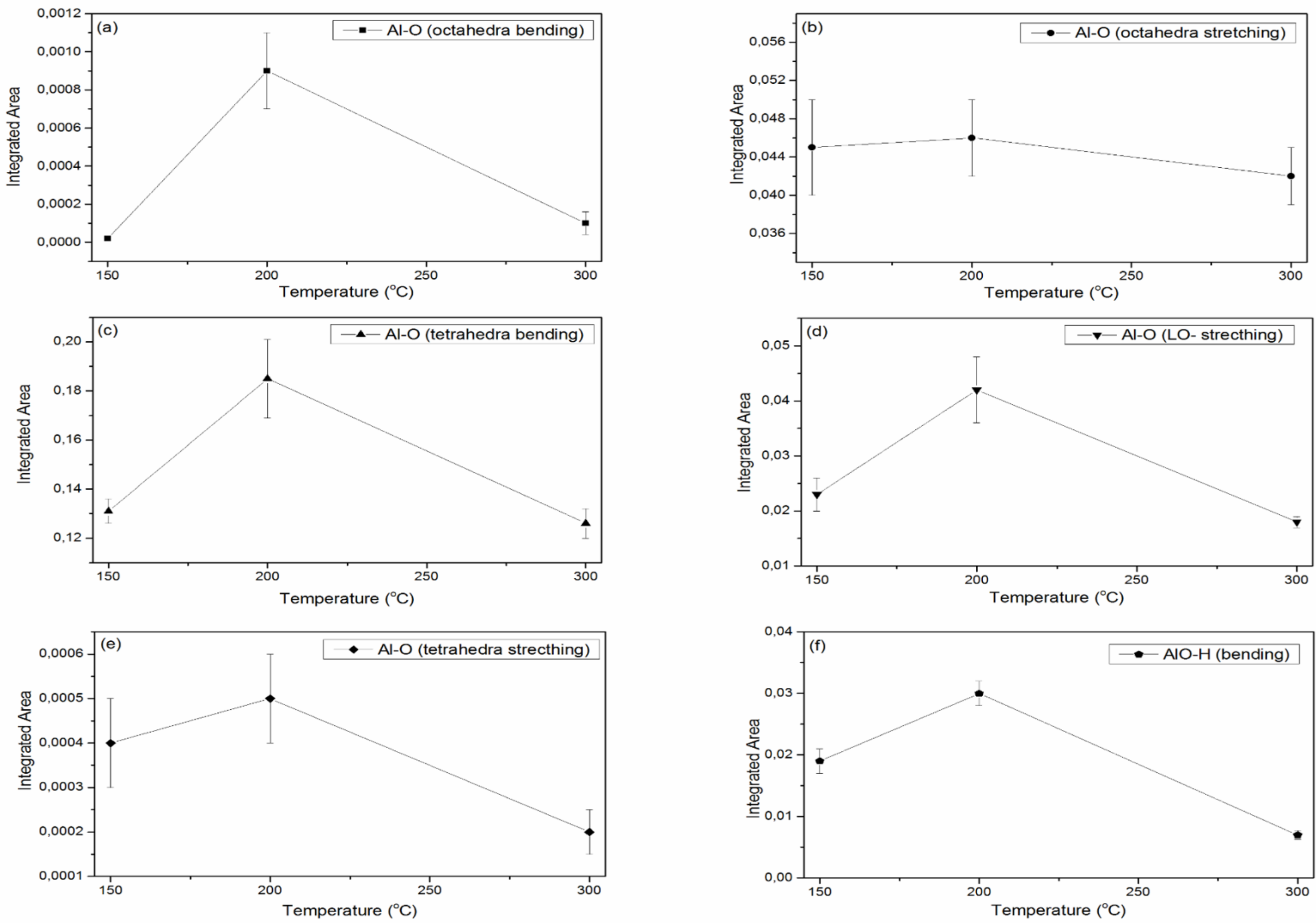

Table 3.9 Fitting results of selected samples

Vibration Peaks		***Center Peak Position***			***FWHM***			***Integrated Area***		
		Sample 1	***Sample 5***	***Sample 7***	***Sample 1***	***Sample 5***	***Sample 7***	***Sample 1***	***Sample 5***	***Sample 7***
Peak (1)	$Al\text{-}O_6$ (bending)	480.0 ± 3.4	483.0 ± 2.1	485.0 ± 6.3	21.6 ± 9.4	45.7 ± 7.8	7.4 ± 1.5	1E-4 ± 6E-5	9E-4 ± 2E-4	2E-5 ± 0.3E-5
Peak (2)	$Al\text{-}O_6$ (stretching)	601.1 ± 3.5	582.7 ± 4.6	587.6 ± 1.9	167.8 ± 3.7	164.4 ± 7.6	144.5 ± 2.6	0.042 ± 0.005	0.046 ± 0.011	0.045 ± 0.003
Peak (3)	$Al\text{-}O_4$ (bending)	742.9 ± 3.8	731.2 ± 4.0	735.6 ± 1.5	223.9 ± 7.4	238.2 ± 14.4	213.9 ± 7.1	0.126 ± 0.006	0.185 ± 0.016	0.131 ± 0.005
Peak (4)	Al-O (stretching)	971.1 ± 2.6	960.1 ± 6.9	962.0 ± 4.8	157.2 ± 5.1	205.3 ± 12.5	192.4 ± 16.0	0.018 ± 0.001	0.042 ± 0.006	0.023 ± 0.003
Peak (5)	$Al\text{-}O_4$ (stretching)	1141.2 ± 3.4	1160.5 ± 3.36	1165.7 ± 4.1	97.7 ± 12.0	42.7 ± 10.3	41.2 ± 12.3	2E-4± 5E-5	5E-4 ± 1E-4	4E-4 ± 1E-4
Peak (6)	Al-OH(bending)	1260.0 ± 13.1	1194.3 ± 10.3	1238.6 ± 7.9	260.0 ± 20.0	303.7 ± 12.5	281.5 ± 43.5	0.007 ± 7E-4	0.030 ± 0.002	0.019 ± 0.002
Peak (7)	CH_2 (bending)	-	-	1423.2 ± 6.0	-	-	123.8 ± 28.9	-	-	0.002 ± 0.001
Peak (8)	O-H(stretching)	-	-	1602.3 ± 2.1	-	-	59.2 ± 5.3	-	-	0.001 ± 1E-4
Peak (9)	C-O(stretching)	-	-	1893.0 ± 11.9	-	-	237.6 ± 28.7	-	-	0.001 ± 1E-4
Peak (10)	CH_2(stretching)	-	3250 ± 8.46	3258.9 ± 11.9	-	103.2 ± 1.73	577.6 ± 19.6	-	7E-4 ± 1E-4	0.016 ± 4E-4
Peak (11)	O-H (stretching)	3370.0 ± 21.5	3483.0 ± 6.0	3467.3 ± 5.5	300.0 ± 49.5	145.4 ± 17.9	322.1 ± 14.6	0.001 ± 1E-4	0.002 ± 3E-4	0.007 ± 2E-4

3.6. X-Ray Photoelectron Spectroscopy Results (XPS)

3.6.1. Basic Theory

The last complementary characterization technique is X-Ray Photoelectron Spectroscopy (or electron spectroscopy for chemical analysis - ESCA) which is widely used to investigate chemical composition of samples [156]. The principle of the technique relies on the photoelectric effect [157] and is highly surface specific due to the short range of the photoelectrons that are excited from the solid. Figure 3.26 shows the basic diagram of typical XPS instrument. The incoming light with a fixed photon energy impinges the sample and excites the electrons from their bound states into free electrons with a kinetic energy that is smaller for formerly stronger bound electrons. These electrons are collected by a lens system and then detected by an energy analyzer. With an energy analyzer electrons of specific kinetic energy can be selected and counted by the detector and this gives a spectrum with a series of photoelectron peaks. The binding energy of the peaks is characteristic of each element. The peak areas can be used to determine the composition of the material's surface. The shape of each peak and the binding energy can be slightly altered by the chemical state of the emitting atom. Thus XPS can provide chemical bonding information as well [158, 159].

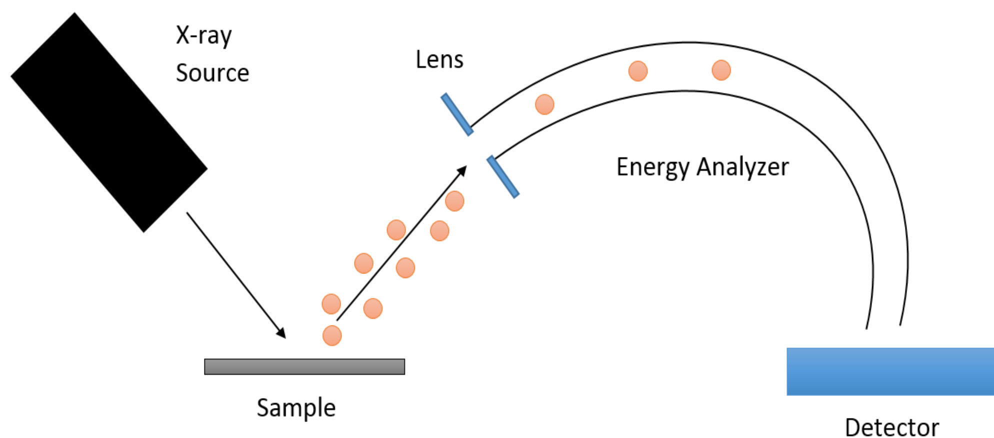

Figure 3.28 Basic Diagram of typical photoelectron instrument used in XPS

XPS is not sensitive to hydrogen or helium, but can detect almost all other elements. The binding energy for H or He is in the range of MeV whereas the other

ANADOLU ÜNİVERSİTESİ

atoms have corresponding energies in the order of eVs [158]. Ultra-high vacuum (UHV) condition is needed for XPS experiment. Moreover, XPS is a semi quantitative method because it is surface sensitive technique and the photoelectrons generally have low kinetic energies [156].

3.6.2. Experimental Setup and Method

XPS is not only suitable for surface analysis, but also for depth profiling of the samples. In depth profile method, the accelerated Ar^+ ions etch the sample surface at specific point with specific time, then we measure the chemical composition at that etch point. This method is a destructive method. By using this process, atomic mixing, knock on implantation, bond breaking, charging and preferential sputtering can possibly occur. In order to eliminate these effects, high mass ions with low energy can be used. On the other hand, it's superior method for multi-layer structure analysis [160].

Table 3.10 Detailed acquisition parameters

Total acquisition time	5.0 sec.
Number of frames	5
Source Gun Type	Al K-Alpha
Spot Size	400 μm
Lens Mode	Standard
Energy Step Size	0.151 eV
Analyzer Mode	CAE: Pass Energy 151.2 eV

Thermo Scientific K-Alpha - Monochromated high-performance XPS spectrometer was used to analyze depth profile chemical composition of the selected samples. The surface layer was etched with Ar^+ ions and the measurements were taken every 10 seconds by using Al K-Alpha as the excitation source. Thus, the percentage of elements is observed in different etch depth. The measurements were performed with an energy step.

Figure 3.27 shows Al 2p peak position of the Sample 7 for surface and after 10 seconds etching. The surface binding energy of Al 2p has low and shift binding energy. It can be correlated with contamination of the surface due to the

ANADOLU ÜNİVERSİTESİ

environment. The peak position of Al 2p binding energy is ~75.3 eV under the surface. It can be associated with third oxidation state of Al [161]. The same shift trend is observed for O 1s. The photoelectron spectrum of O 1s illustrates a typical O 1s peak of metal oxide at 532.0 eV. The data of XPS shows that stoichiometric Al_2O_3 layers of Al-O chemical binding state grown by ALD [94]. After observing the binding energy of Al 2p and O 1s is correlated with Al_2O_3 state. In order to calculate the stoichiometry of Al_2O_3, the atomic concentration is needed both Al 2p and O 1s. The XPS instrument gives the atomic percentage of both elements at every etch point. By using the peak area, atomic percentage of each elements can be also calculated. Detailed acquisition parameters are given in Table 3.10.

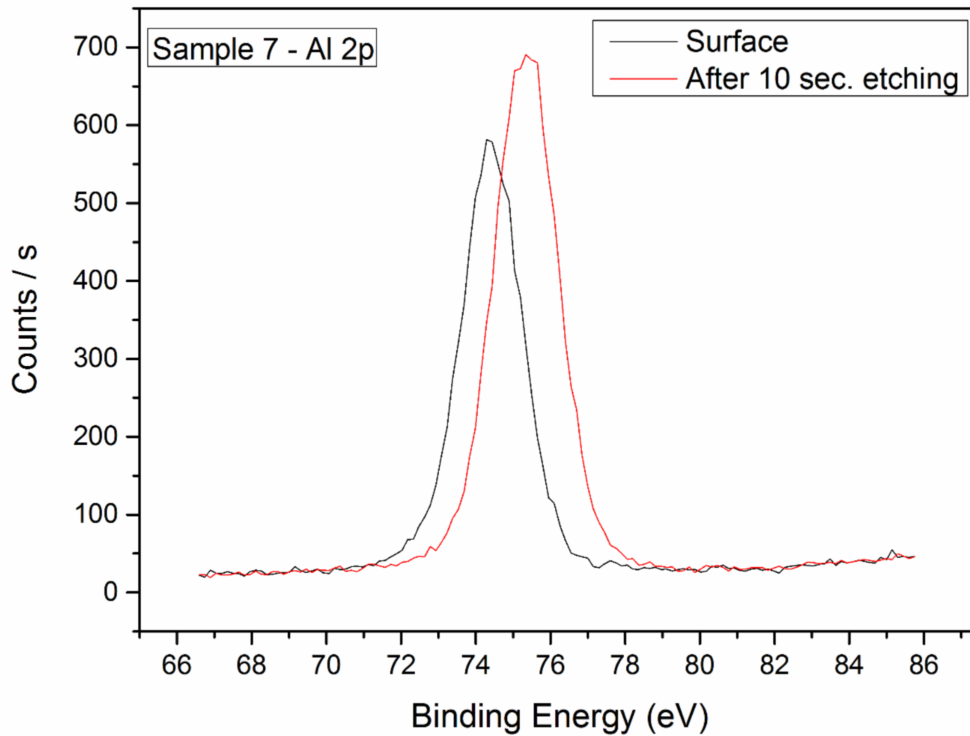

Figure 3.29 Al 2p peak position of Sample 7 for surface and after 10 seconds etching

3.6.3. Experimental Results and Discussion

The stoichiometry analysis of Al_2O_3 of the selected samples is calculated as a function of etch depth. The percentage of each element is used to calculate the stoichiometry of Al_2O_3 [162]. Afterwards, the average of Al_2O_3 stoichiometry for selected samples is calculated and given in Table 3.11. C 1s peak completely disappears after first 10 seconds etching. It may have reduced below the detection

ANADOLU ÜNİVERSİTESİ

limit of the XPS (detection limit < 0.1%). Si 2p is detected ~1% or below for each etch step. The "Sample 1" with a stoichiometry of $Al_2O_{(3.02 \pm 0.15)}$ has the desired Al/O ratio.

Table 3.11 Stoichiometry of Al_2O_3 for selected samples

Samples	Stoichiometry
Sample 1 (Temperature: 300 C & Purge Time: 4 sec.)	$Al_2O_{(3.02 \pm 0.15)}$
Sample 5 (Temperature: 200 C & Purge Time: 4 sec.)	$Al_2O_{(2.70 \pm 0.19)}$
Sample 7 (Temperature: 150 C & Purge Time: 4 sec.)	$Al_2O_{(2.58 \pm 0.16)}$

The percentage change of "Sample 1", "Sample 5" and Sample 7 are shown in Figure 3.28. The etch rate of each sample can be interpreted by observing the time of sudden increase in the percentage of Si 2p. For "Sample 5" and Sample 7, increase of silicon percentage starts approximately at range of 600-650 seconds etch time. However, increase of silicon percentage for "Sample 1" starts approximately at range of 950-100 seconds etch time. The etch process continues up to 2000 seconds but the percentage of Si 2p reach only level of ~ 47 %. As a comment, it occurs due to high density of "Sample 1" or associated with used measurement method.

ANADOLU ÜNİVERSİTESİ

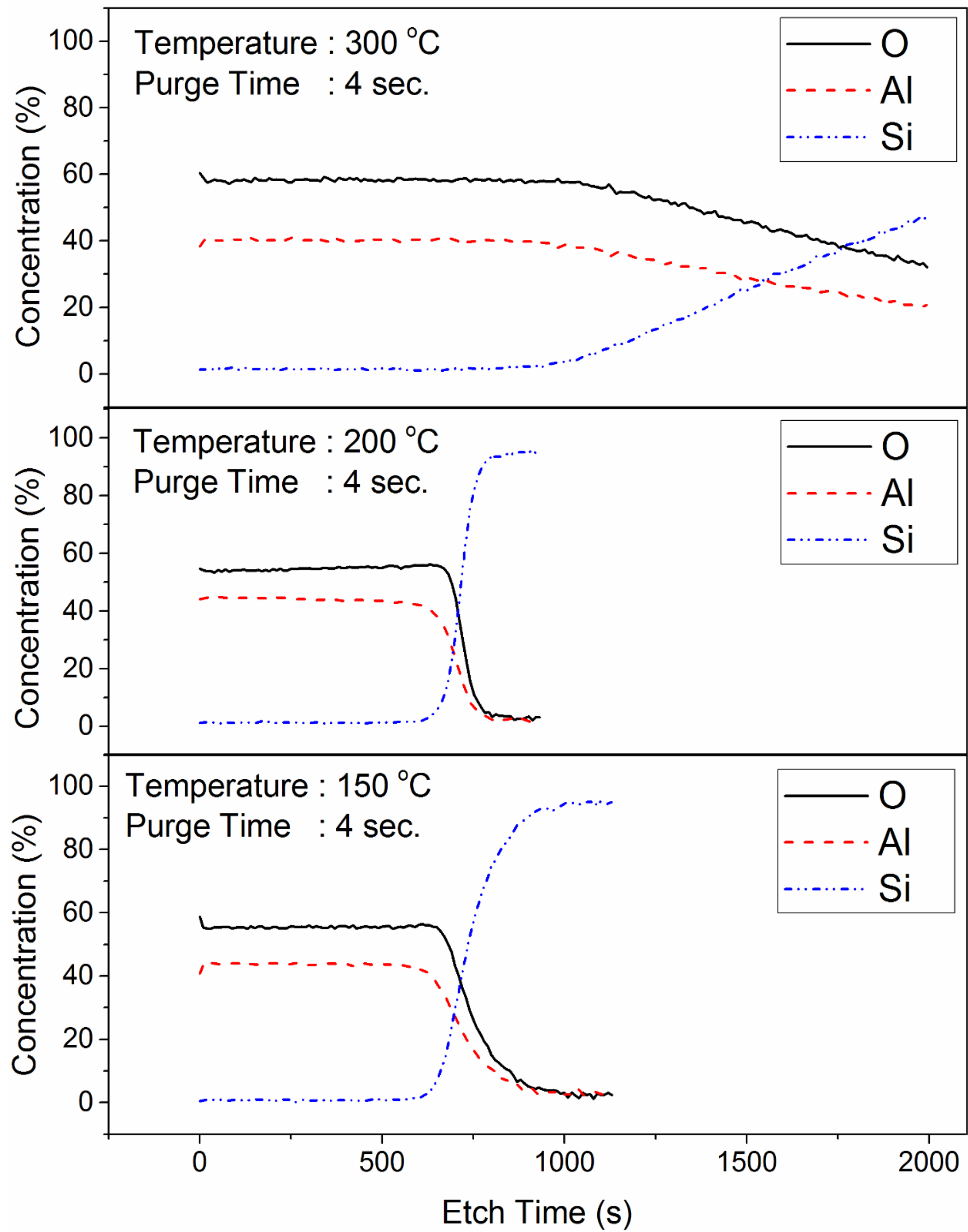

Figure 3.30 The atomic concentration variation of O, Al, and Si as a function of etch time for three samples grown at 300 °C with 4 seconds purge time, 200 °C with 4 seconds purge time and 150 °C with 4 seconds purge time.

ANADOLU ÜNİVERSİTESİ

4. POLARIZATION INSENSITIVE SINGLE MODE AL_2O_3 RIB/RIDGE WAVEGUIDE DESIGN

In integrated optics optical ridge/rib waveguide structure is widely used in waveguide applications for active and passive optoelectronic devices. For most of the applications in photonics, the optical waveguides operate at single mode condition. In general, in order to fulfill this requirement, ridge waveguides are employed and designed with different numerical methods such as mode matching method [163], beam propagation method (BPM) [164], finite element method [165] and effective index method [166]. In particular, important information which is missing in the literature [163, 164, 165, 166]is the optimization of waveguide structure with wavelength, mode size and polarization characteristics. In addition, limited number of studies on a-Al_2O_3 do not provide the key design parameters for single-mode ridge waveguide [109, 104, 167]. Therefore, after the determination of optimum ALD growth parameters and film composition that was characterized with Ellipsometer, XRD, Micro-Raman, FTIR and XPS, a design approach should be developed and performed before the experimental realization of the ridge waveguide. To achieve this design goal one needs to take into account full aspects of the ridge waveguide that includes both passive and active, single mode, wavelength and polarization insensitive design of Al_2O_3 rib waveguides on SiO_2 substrate. BPM is a valid tool to investigate influence of the waveguide height, etch depth, waveguide width and operation wavelength to the mode number, mode size, birefringence and polarization sensitivity. Design parameters for targeted properties are computed for the waveguide width ranging from 0 to 10 μm, and for etch depth ranging from 0 to 0.5 μm for fixed waveguide height of 0.5 μm. A design window suggested as fixed width of 3.5 μm and etches depth of 0.325 to 0.375 μm for single mode, wavelength and polarization insensitive Al_2O_3 waveguides on thermal oxide. In addition to achieved design parameters, we proposed a novel rib TE mode selective filter design as an output of the numerical simulations.

4.1. Simulation Structure and Parameters

The dimensions of the ridge waveguide structure investigated in this part of the thesis are given in Figure 4.1. Al_2O_3 rib waveguide is on SiO_2 substrate. The

ANADOLU ÜNİVERSİTESİ

refractive index value of amorphous Al_2O_3 at wavelength (λ) = 1.55 µm is known to be n=1.64 [168] and that of SiO_2 is 1.44 [169]. W represents the width of the waveguide, H is the total thickness, D is the etch depth and SH is the slab height of the rib waveguide. Since H is fixed to 0.5 µm, D is defined as (0.5 – SH).

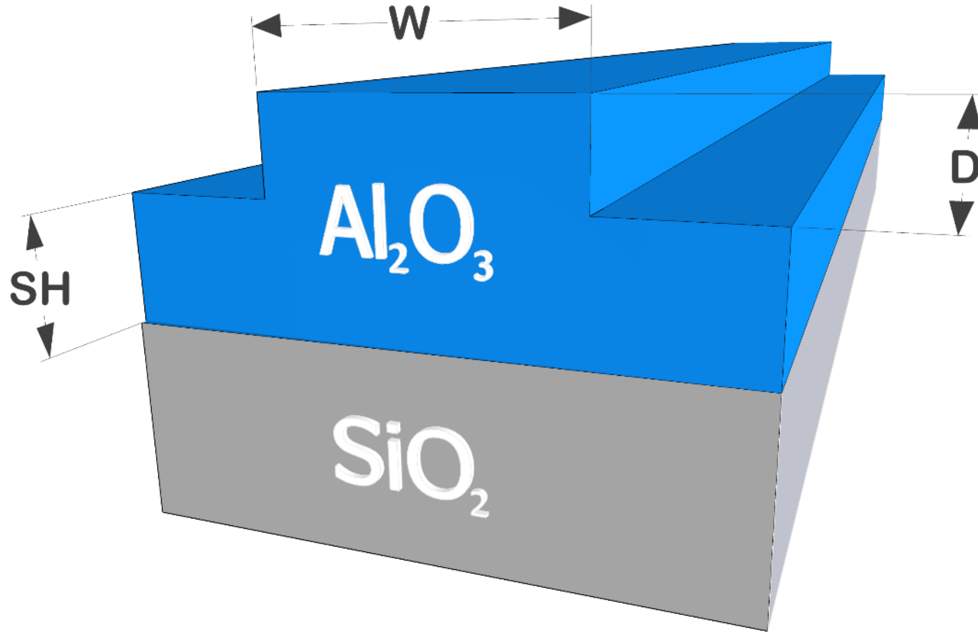

Figure 4.1 Simulated rib waveguide on SiO_2 substrate. D, W and SH represents etch depth, waveguide width and slab height, respectively.

Total thickness of the rib waveguide was determined according to the ALD growth time and thickness limitation as explained in the third part of the thesis. Width is scanned from 0 to 10 µm with 0.2 µm increments. 0.2 µm was chosen as it represents the lateral resolution limitation of a general photolithography process. D is scanned between 0 to 0.5 µm with 25 nm increments. Zero D indicates a slab waveguide geometry with a SH of 0.5 µm. 0.5 µm D indicates photonic wire geometry.

Computation was performed with semi-vectorial BPM. In this technique, exact wave equation is approximated for monochromatic waves and then it's numerically solved for guided wave problem by the BPM algorithm. One can find excellent reviews in the literature for the details of the technique and its variations [170, 171, 172].

To perform BPM, a simulation window of -50 µm to +50 µm in lateral direction, and -8 µm to +2 µm in vertical direction, and 5 mm waveguide length to

ANADOLU ÜNİVERSİTESİ

satisfy convergence of the iterative mode solver was used. To prevent artificial back reflection of light incident on the boundary, Transparent Boundary Condition is used (TBC). Details of the TBC can be found elsewhere [173]. The position of the launched tilted fiber mode was adjusted as half of the width used in each run of the computation to excite possible higher order modes.

Birefringence resulting from the effective index change due to the Transverse Electric (TE) and Transverse Magnetic (TM) polarizations was calculated for three wavelengths of 1.48, 1.53, and 1.55 μm. Birefringence caused by group index (n_g) was also studied by using Equation (4.1) [174],

$$n_g = n_{eff} - \lambda \times \frac{\partial n_{eff}}{\partial \lambda}, \tag{4.1}$$

where n_{eff} is the effective index at wavelength λ.

4.2. Simulation Results

In this section, analysis of one of the geometrical limits, i.e. the slab waveguide, will be discussed first. After obtaining required data from the slab waveguide, results of the rib waveguide are presented. Analyzed aspects of the rib waveguide includes single mode zone of the rib waveguide at different wavelengths, mode size of the selected rib waveguides and calculated birefringence of the selected rib waveguides.

4.2.1. a-Al_2O_3 Slab Waveguide

The aim of the slab waveguide analysis is to determine the thickness, SH, where the slab waveguide does not support any mode. This information is also used to support rib waveguide analysis. Investigated wavelengths are 1.48 μm excitation wavelength of Er doped amplifier, 1.53 and 1.55 μm emission wavelengths of the amplifier. 1.61 μm at the border of third communication window also selected for simulation to see how far we can engineer the mode profile variation or to see the wavelength dependence of the single mode region of the waveguide.

ANADOLU ÜNİVERSİTESİ

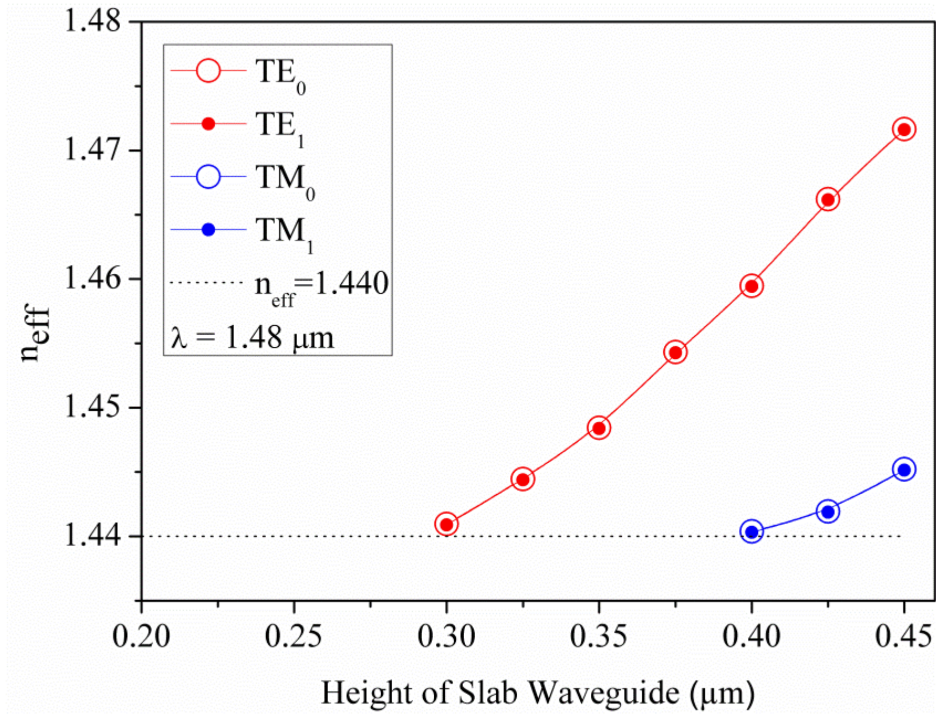

Figure 4.2 Change of effective index (n_{eff}) with respect to slab height of the waveguide at λ = 1.48 μm Fundamental and higher order modes were represented by open and filled circles, respectively. Red indicates TE polarization, and blue represents TM polarization. Dashed line indicates effective index value equal to substrate's (SiO_2) refractive index.

The results of the numerical analysis of the slab waveguide are plotted in Figure 4.2. The graph demonstrates effective index (n_{eff}) values of both TE and TM polarizations at λ = 1.48 μm for different slab heights (SH). Dashed line indicates substrate's (SiO_2) refractive index. It is well known that when the effective index of the waveguide decreases below the substrate's refractive index, waveguide doesn't support any mode [175]. This fact can be observed in Figure 4.2. The minimum SH that support a mode is 0.30 μm for TE polarization and 0.40 μm for TM polarization. SH smaller than these values corresponds to n_{eff} values below the dashed line in Figure 4.2.

4.2.2. Mode Analysis of Rib/Ridge Waveguide

The rib waveguide mode analysis was performed for λ = 1.48, 1.53, 1.55 and 1.61 μm to identify the region where with single mode propagation only. Each in Figure 4.3 represents a special geometry for four different wavelength where mode character of the rib waveguide changes. Depending on the geometry of the waveguide n_{eff} changes. As explained in previous section, n_{eff} values smaller than

ANADOLU ÜNİVERSİTESİ

substrate refractive index result no light propagation. For example, for TE polarization at λ = 1.48 μm red square with cross frame points in Figure 4.3(a) corresponds to these rib geometries where this transition, no propagation to single mode propagation, occurs. As an example, D = 0.25 and W = 1 μm is one of these geometries and supports only single mode. If we keep D constant and change the width of the rib waveguide to 0.8 μm, we end up with a waveguide that has no guiding. Therefore, these square with cross frame points can be considered as elements of a line separating two regions as single mode region and no propagation region in Figure 4.3(a), which also applies to TM polarization in same figure.

For a specific geometry the waveguide starts to support not only single mode but more than one mode. Consider the point representing D = 0. 25 μm and W = 1 μm in Figure 4.3.a. If we increase the width of the waveguide, it conserves its single mode character up to a point where it starts to support TE_1. This special point is 3.2 μm for D = 0.25 μm, indicated by red filled square in Figure 4.3(a). Rest of the red filled square in Figure 4.3(a) correspond to a rib geometry where we have TE_0 and TE_1 simultaneously propagating in the waveguide. These points form a line that separates multi-mode region and single mode region. Same applies to in the same figure for TM polarization (black square with cross frame).

It is apparent from Figure 4.3(a) that there exist a range of width values for the fixed etch depth where the waveguide has single mode character. When combined, these ranges of width values form a single mode zone. Dashed red region in Figure 4.3(a) is the single mode region of TE mode and dashed black region is single mode region for TM.

Beside the horizontal separation lines in Figure 4.3(a), rib waveguides show a very interesting property that reveals itself by dashed vertical lines in same figures. Position of the vertical dashed lines are at D = 0.2 μm (0.3 μm slab height) and D = 0.1 μm (0.4 μm slab height) for TE and TM polarizations, respectively. Left hand side of the dashed lines indicates an area where one can always find a mode. We labeled this region as “slab-like character” in Figure 4.3(a).

ANADOLU ÜNİVERSİTESİ

Table 4.1 Combination of mode profiles of TE and TM polarizations designate nine different regions that demonstrate "character" of the waveguide of which two of them (number 2 and 3) are technologically important. Please note that region number 3 in bold is the single mode region for both polarizations.

Region Number	**Waveguide Character**
1	No propagation zone for both polarizations.
2	**Single mode propagation for TE and no propagation for TM.**
3	**Single mode region for both polarizations.**
4	Single mode for TM and multi-mode for TE.
5	Multi-mode for both polarizations.
6	Slab-like character for only TE and no propagation for TM.
7	Single mode for TM and slab like character for TE mode.
8	Multi-mode for TM and slab like character for TE mode.
9	Slab-like character for both polarizations.

Slab waveguide analysis in previous section helps us to understand the slab-like character of the rib waveguide. When D goes to zero, etch depth of the waveguide gets smaller and slab height start to dominate the character of the rib waveguide. We found that a rib waveguide with slab height of 0.3 μm for TE and 0.4 μm for TM polarization behaves like a slab waveguide. Please note that exactly same slab thicknesses also found in slab waveguide analysis in previous section demonstrating guiding geometry above these critical thicknesses. In the case of slab waveguide these thicknesses are found to be critical. Below these thicknesses there was no mode for the slab waveguide. However, for thicker slab dimensions multi-mode character is observed. In the rib waveguide case, above these slab thicknesses waveguide has multi-mode character without any width dependence. The interesting point here is that this change of the behavior from rib to slab propagation is very sharp.

ANADOLU ÜNİVERSİTESİ

Simulations have been carried out to find a region where we have single mode character for both polarizations. It is possible to obtain this region by combining the data of two polarizations. When combined together, Figure 4.3(a) is obtained. Combination has resulted in 9 different regions that are identified and designated in Table 4.1.

ANADOLU ÜNİVERSİTESİ

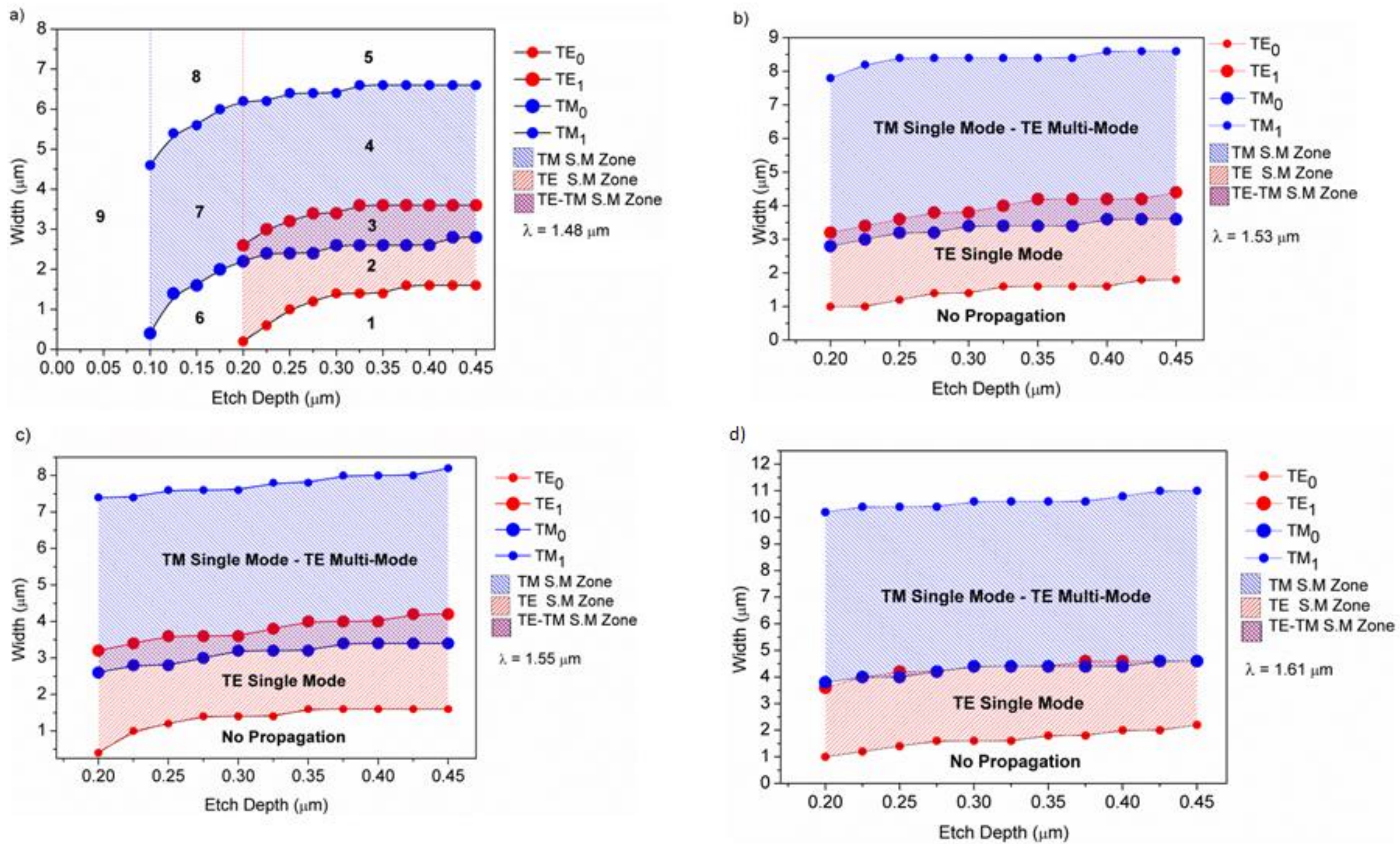

Figure 4.3 Mode regions for the third optical communication window at a) λ=1.48 μm b) λ=1.53 μm c) λ=1.55 μm d) λ=1.61 μm . S.Z.M. in the legends is acronym for “Single Mode Zone”

The mode regions of ridge waveguide as a function of width and etch depth at λ=1.48, 1.53, 1.55 and 1.61 μm is shown in Figure 4.3(a), Figure 4.3(b), Figure 4.3(c) and Figure 4.3(d). Figure 4.3(a) which is the combination of TE and TM single mode zone at λ=1.48 μm demonstrates the flexibility of a rib waveguide that gives many important technological features by just changing two simple and easily achievable parameters, D and W with photolithographic processes. In Figure 4.3(a) we have nine regions. These regions are labeled from 1 to 9 in Figure 4.3(a). Numbers are explained in Table 4.1. Two of them are technologically important. Importance of single mode region (region number 3) was explained in the beginning of the Chapter 4. There is an additional region that is labeled with 2. Rib waveguide geometry that falls into this area does not allow TM polarization to propagate but guides TE polarization only. Therefore, this region filters out the incident TM polarization and hence transmits only the TE polarization. Such a waveguide can be used as a TE mode selective filter**.** Mode selective filters are basic devices for communication and optical sensing applications [176]. To the best of our knowledge, there is no report on such a simple rib waveguide filter device in literature. Most of the TE mode selective filters fabricated have much more complex structures than demonstrated in this article. For instance, one waveguide structure that filters the TM mode uses metal claddings and hence called as metal-clad optical waveguides [177]. It benefits the higher loss of TM mode in metal cladding [177, 178]. There are also waveguides that benefit from anisotropy of the materials for filtering [179]. A device that benefits from such effects requires additional layers or [180] different materials that are hardly compatible with each other making integration and fabrication process complicated. Here we suggest a possible TE mode selective filter using amorphous Al_2O_3 rib waveguide that has no metal claddings, no additional buffer layers [180] to leak TM mode or has no anisotropy due to the amorphous nature. The only requirement is that both the waveguide width and etch depth of the rib structure must be selected from TE single mode region of Figure 4.3(a). W and D can be easily adjusted with well-known standard photolithography process. The idea of the rib waveguide mode selective filter can be generalized for amorphous oxide materials that have total thickness

ANADOLU ÜNİVERSİTESİ

less than operation wavelength with a moderate refractive index change (Δn), which is around 0.2.

The idea of identifying a polarization insensitive single mode region for the rest of the wavelengths was also tested. It must be noted that the cross section of the TE and TM single mode region gives technologically important area only above D = 0.2 µm. Therefore, the data including regions 6 to 9 that was labeled in Figure 4.3(a) and explained in Table 4.1 was omitted for the rest of the wavelengths.

Inspection of Figure 4.3 indicates that increase of the wavelength results in shrinkage of the polarization insensitive region. At 1.61 µm the region collapses to a line. In principle, simulations suggest that it's still possible to work in a single mode region, if W and D are selected exactly on this line, however it may not be practical due to the resolution of lithography process and fabrication tolerance limits.

In addition to polarization insensitive single mode region, we can identify a region that is also wavelength insensitive. This can be done by merging graphs of Figure 4.3(a), Figure 4.3(b), Figure 4.3(c) and Figure 4.3(d). Figure 4.4(a) gives the resulting zone.

Combination of mode profiles of all wavelengths including polarization effects do not provide a polarization and wavelength single mode insensitive region for 1.61 µm, but ensures the targeted characteristics for the rest of the wavelengths as depicted in Figure 4.4(a). On the other hand, the geometries in shaded gray area in Figure 4.4(b) can be used for Erbium doped Al_2O_3 optical amplifiers, which are pumped at 1.48 µm and have an emission wavelength of 1.53 and 1.55 µm [181, 182].

ANADOLU ÜNİVERSİTESİ

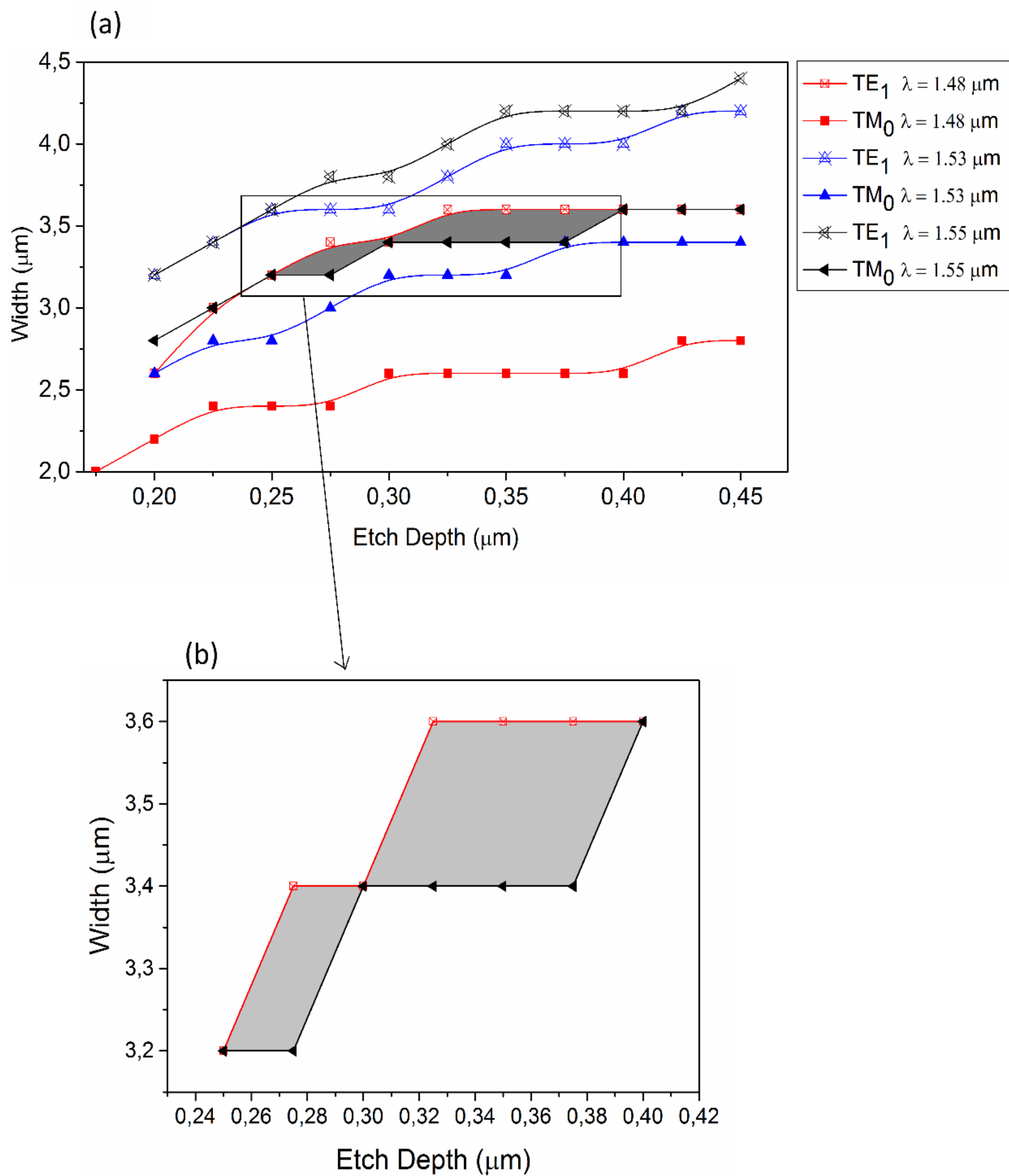

Figure 4.4 (a) Single mode region at different polarization and wavelengths as λ=1.48, 1.55 and 1.61 μm (b) Gray filled area demonstrates the region where indicated wavelengths are single mode without any polarization dependence. Solid lines are to guide the eye.

All single mode region at different wavelengths and different polarization state is shown in Figure 4.4(a). Figure 4.4(b) is the zoomed version of Figure 4.4(a) for showing special region. The gray filled area in Figure 4.4(b) shows the region which is independent from wavelength and polarization of the rib waveguide. Once again by selecting W and D properly, one can design a rib waveguide that supports three wavelengths or a range of wavelengths from 1.48 μm to 1.55 μm ensuring single mode propagation without any polarization restriction. Considering the fabrication tolerances of the photolithography fabrication process the suggested

ANADOLU ÜNİVERSİTESİ

target dimensions range is between a ridge width of 3.5 μm and D of 325 nm to 375 nm.

4.2.3. Mode Size of Rib/Ridge Waveguide

Mode sizes of the selected rib waveguides were investigated. Mode size in this investigation is defined as the width that corresponds to 1/e of the peak intensity at both x and y direction, labeled as W_x and W_y, respectively. Here we use mode area concept that gives rough but better evaluation of the confinement. Mode area is defined by simple multiplication of W_x and W_y. Geometry selection criteria depend on the limitation of the lithography process. A set of data points that forms

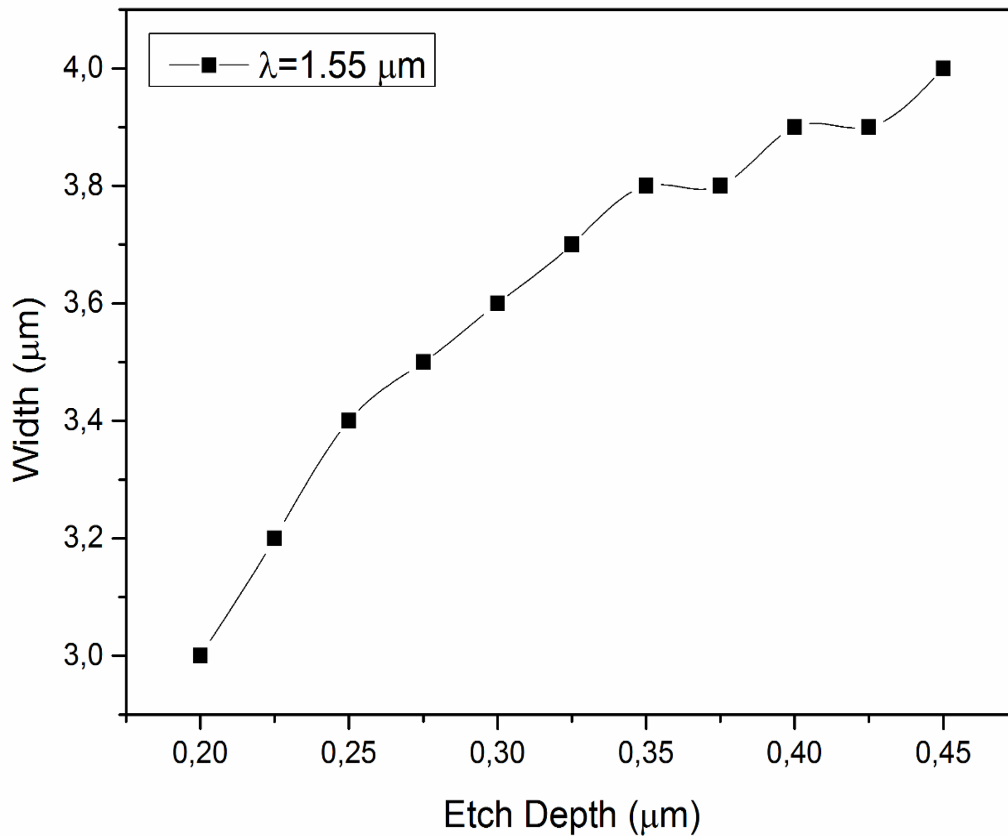

Figure 4.5 Selected width and etch depth dimensions for mode size investigation at 1.55 μm

a line at half of the single mode region are selected. These geometries are given in Figure 4.5 only for the wavelength of 1.55 μm. Because the emission of Er^{3+} ions are expected at 1.55 μm.

Mode area is given for different polarizations at wavelength of 1.55 μm Figure 4.6(a) and Figure 4.6 (b) shows the results of mode area for TE and TM

ANADOLU ÜNİVERSİTESİ

polarization at wavelength of 1.55 μm, respectively. Inspection of the Figure 4.6 for the geometries of interest leads to the following observations:

i. TM polarization always gives bigger mode area than TE polarization.
ii. Mode area slightly decrease when etch depth gets deeper and width gets wider.

Mode area can be thought as an indication of the confinement. It is apparent that frequency of the longer wavelength would be relatively close to cutoff frequency with respect to shorter ones. As we approach to cutoff frequency, mode confinement at the Al_2O_3 layer decreases and evanescent field expands. This expansion corresponds to bigger mode area.

In the BPM method that we use, we always monitor electric field profile. Electric field is along X direction (vertical direction) for TE polarization. In this direction, maximum boundary dimension that field encounters is the total waveguide height which is 0.5 μm thick. In the case of TM polarization, electric field is along Y direction (lateral direction). Lateral direction includes width, which is 5 to 6 times larger than total height. We have also an extended slab thickness of the rib waveguide in this direction. Therefore, the electric field of TM polarization is much larger than TE and to fulfill boundary conditions mode size has to be larger than TE polarization. Effective index method was also used to reach the same conclusion. Confinement of the single mode region was also evaluated for 1.55 μm due to the importance of this wavelength. It is also done to evaluate our observation on the general mode area trend as given above. Confinement was calculated by numerically integrating the total area of the three dimensional mode intensity on X-Y plane. Result can be seen in Figure 4.7(a).

ANADOLU ÜNİVERSİTESİ

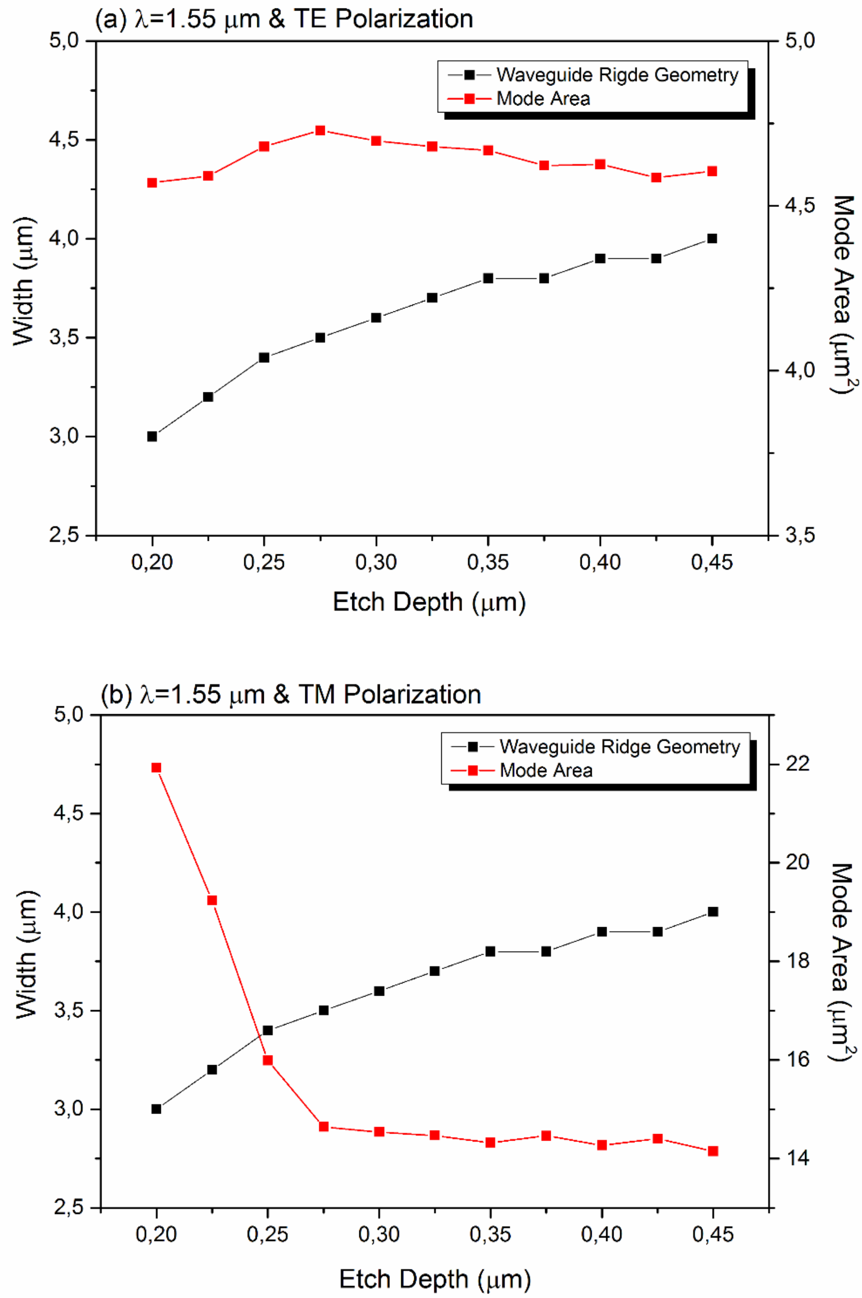

Figure 4.6 Mode areas of the wavelength of 1.55 μm as a function of rib geometries a) TE polarization b) TM polarization

ANADOLU ÜNİVERSİTESİ

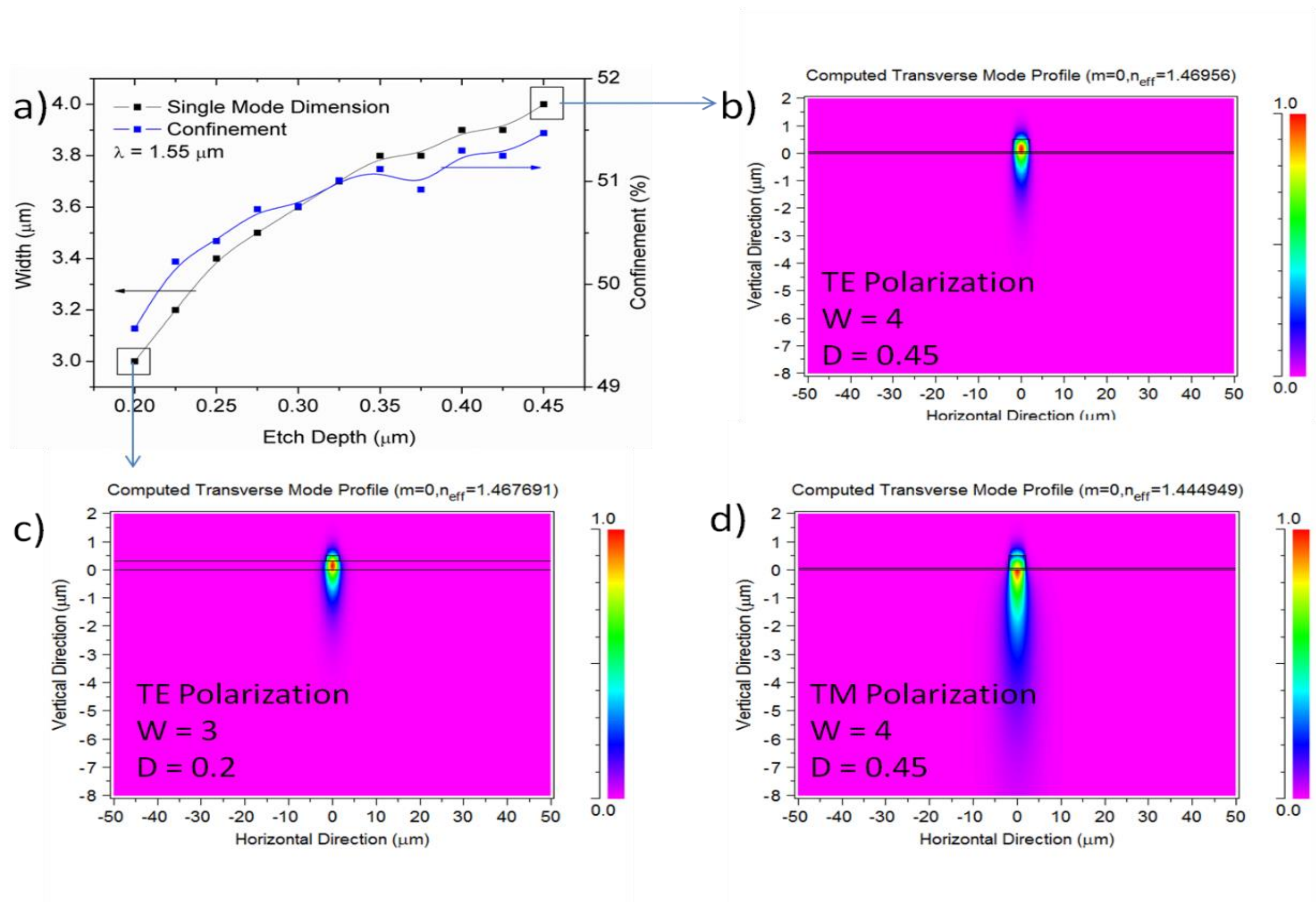

Figure 4.7 Single mode confinement of the rib waveguide with respect to W and D at λ=1.55 μm. a) Confinement factor for different geometries, b) TE mode field profile at W=3 μm D=0.2 μm, c) TE mode field profile at W=4 μm and D=0.45 μm, d) TM mode field profile at same dimension with c

TE confinement starts from 49.57% for smallest single mode dimension and increases up to 51.47% as D and W both gets larger. Relatively low confinement factor can be assigned to the small ridge height with respect to launched wavelength.

Mode profiles were also given in Figure 4.7. Figure 4.7(b) and 4.7(c) depicts electric field profiles for TE polarization and Figure 4.7(d) gives electric field profile for TM polarization. The rib waveguide reported in Figure 4.7(c) has W = 3 μm and D = 0.2 μm with a slab height of 0.3 μm. The rib waveguide at Figure 4.7(b) has W = 4 μm and D = 0.45 μm with a very thin slab thickness of 0.05 μm. Close inspection of Figure 4.7(b) and 4.7(c) gives important aspects for possible active waveguide applications. Location of the peak intensity is important for the excitation of all the active ions. The location of the peak of the electric field intensity is just above the 50 nm thick slab of the rib waveguide. Therefore it's inside the ridge for the Figure 4.8(b) whereas the peak position of the electric field intensity is inside the 300 nm slab part of the rib waveguide for the geometry depicted in Figure 4.7(c). Although the two structure have almost the same confinement factors, larger width and deeper etch depth is much preferable for amplification application due to the mode intensity distribution profile. In the case of TM polarization, field profile looks much wider than TE as shown and explained in Figure 4.6. Finally, the horizontal field spread both for TE and TM polarization is observed to be limited.

4.2.4. Rib/Ridge Waveguide Birefringence

For the shaded area indicated in Figure 4.4(b), there exists no zero birefringence rib waveguide geometry. The birefringence calculation for Δn_{eff} and Δn_g are given in Figure 4.8(a) and Figure 4.8(b), respectively. For a fixed width birefringence decreases with increasing etch depth for Δn_{eff} (Figure 4.8(a)) and it makes a minimum at D = 0.33 μm for Δn_g (Figure 4.8(b)). This is due to the fact that TE is well confined within the investigated geometries, which means effective index of the TE mode is quite higher than substrate index (around 1.47). This better support of TE modes can be also seen in mode area in Figure 4.6(a) and mode confinement in Figure 4.7 for wavelength of 1.55 μm. On the other hand, TM is

ANADOLU ÜNİVERSİTESİ

barely supported by the geometries where we have one single mode and wavelength independence. In addition, much larger mode area indicates a lower effective index. Effective indexes of these geometries are 1.444 for TM polarization. These relatively large split between effective indexes results exclusion of zero birefringence character of the waveguide in the range of simulated wavelength and polarization insensitive design geometries.

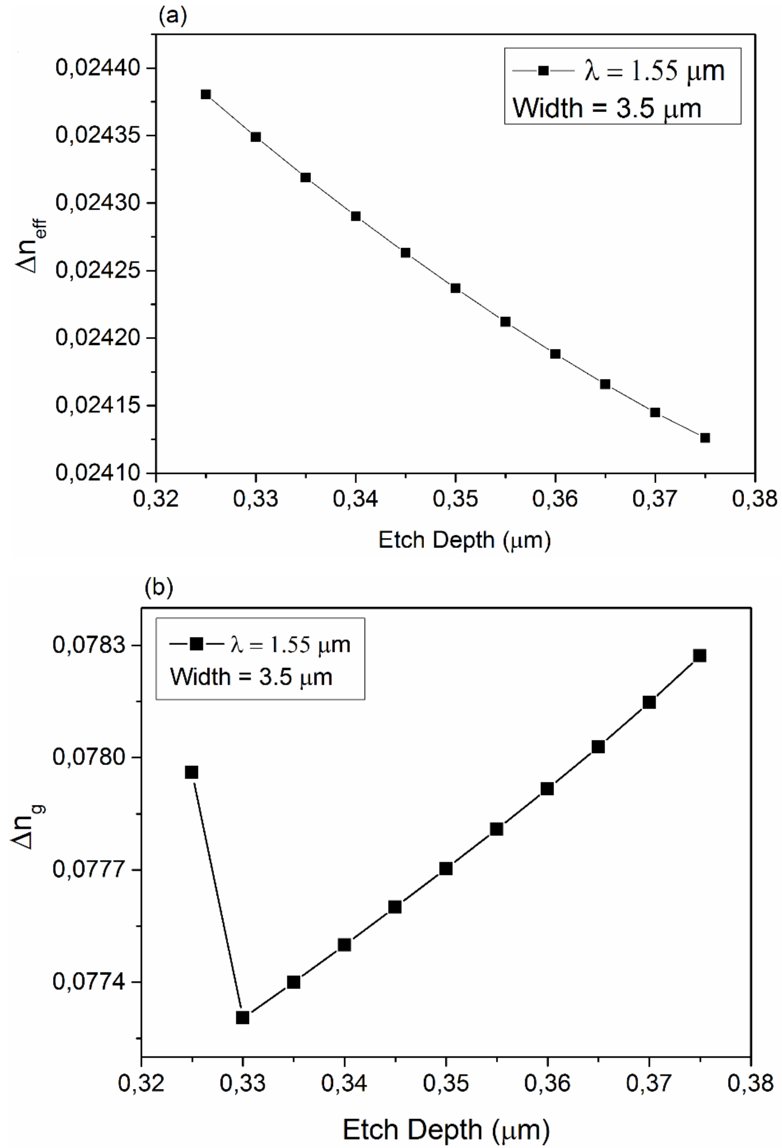

Figure 4.8 Δn_{eff} and Δn_g calculated for the shaded area in Figure 4.4 as a function of etch depth.

ANADOLU ÜNİVERSİTESİ

4.3. Discussion

Polarization insensitive single mode design of rib waveguide has been presented for four wavelengths of 1.48, 1.53, 1.55 and 1.61 µm. Numerical simulations suggested use of a design window of 3.5 µm ridge width with 325 nm to 375 nm etch depth for wavelength insensitive single mode rib waveguides for the wavelengths of 1.55 µm.

It is suggested to use deeply etched profiles and wide width rib waveguides to achieve better confinement and to have a useful mode intensity distribution for amplification applications. I was found that there is no zero birefringence observed for the given narrow range of dimension for wavelength insensitive region and it's not possible to compensate birefringence by changing geometry of the rib waveguide in this range. Numerical simulations suggested a possible rib waveguide TE mode selective filter. Novelty of this filter is its simplicity in fabrication over its counterparts. Filtering mechanism depends only on the etch depth and width of the rib waveguide.

ANADOLU ÜNİVERSİTESİ

5. OPTICAL LOSS CHARACTERIZATION

The propagation loss characteristics of fabricated waveguides are of utmost importance and constitute an essential step in optical waveguide characterization. It is important to confirm that the fabricated waveguides perform as designed. By using loss characteristics, design and fabrication process can be revisited, thus the waveguide performance can be improved. In this chapter, propagation loss characteristics of $Si/SiO_2/Al_2O_3$ planar waveguides are considered.

Thicknesses of SiO_2 and ALD grown Al_2O_3 are ~7μm and ~550 nm, respectively. The planar waveguide is highly multimode at a wavelength of 632.8 nm. The cut off thicknesses are determined by using BPM technique which is described in Chapter 4 in detail. Cut off height values are 75 nm and 125 nm for TE and TM polarization, respectively. The results are shown in Figure 5.1.

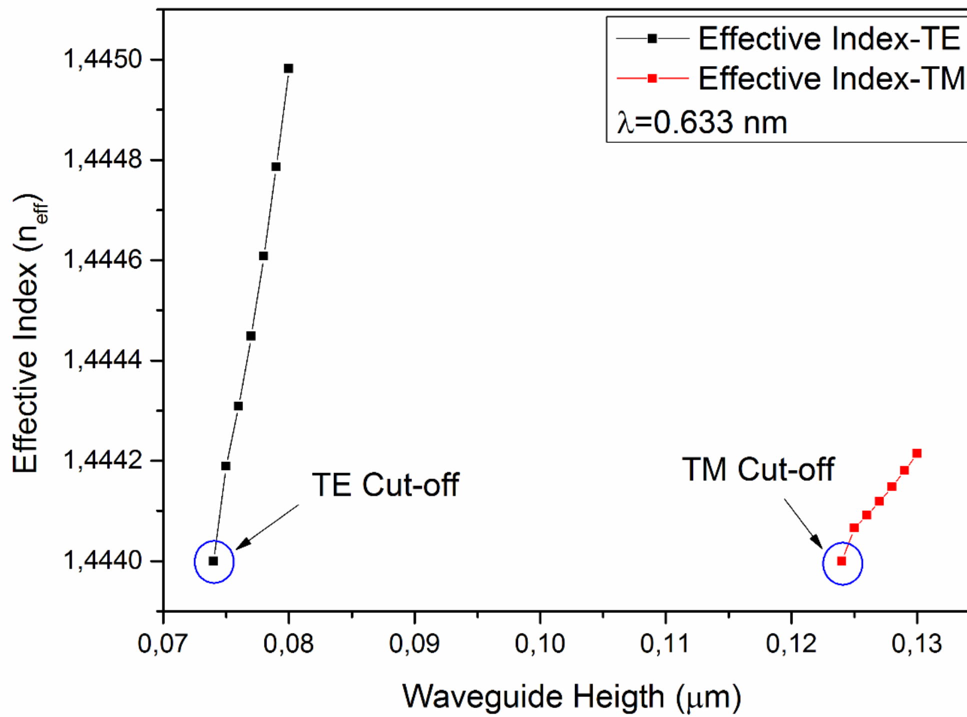

Figure 5.1 $Si/SiO_2/Al_2O_3$ planar waveguide cut off analysis for different polarization

5.1. Method and Experimental Setup

The fabricated waveguide is designed for a telecommunication wavelength range, however, the infrared experimental setup was not accessible for the duration of the thesis. Because of this fact, we describe another method for having general

ANADOLU ÜNİVERSİTESİ

idea of propagation losses at visible wavelengths, instead. The used method, which is nondestructive and real-time technique, is based on the measurement of scattered light from the waveguide surface as a function of propagation length.

In this method, a complementary metal–oxide–semiconductor (CMOS) camera is used for imaging the excited modes in the planar waveguide. In literature, charge coupled devices (CCD) is more commonly reported [183, 184, 185, 186] for optical waveguide loss measurement. However, CMOS cameras have a main advantage of weaker blooming effects for overloaded light intensities [187, 188]. Moreover, this method can be used for both planar and rib/ridge type waveguides.

A He-Ne (632.8 nm) laser has been used as a source and a silicon detector was used for optical power measurement. The images are taken by using Nikon D7000 (CMOS camera) professional camera with 50 mm lens. The camera has been chosen since it has a linear response at raw images. The ambient light was turned off, day light and all other light sources were eliminated as much as possible. A schematic illustration and the experimental loss measurement setup is shown in Figure 5.1 and Figure 5.2.

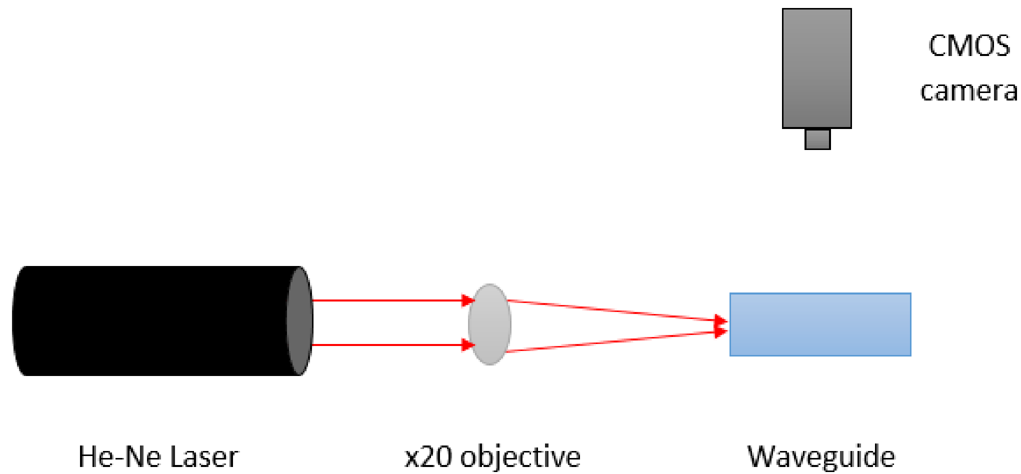

Figure 5.2 Schematic mechanism of Waveguide loss measurement setup

The He-Ne laser is focused through x20 objective having a focal length of approximately 1.5 cm. By using xyz stage, onto which the waveguide is placed, the laser is coupled into the waveguide. The image is taken with a CMOS camera which is placed perpendicularly to the waveguide propagation direction. Long exposure times were used in order to get sufficient intensity of the light for photographing.

ANADOLU ÜNİVERSİTESİ

Moreover, the distance between camera and substrate is important because the image must be focused to the waveguide which depends on the lens which is mounted on the camera.

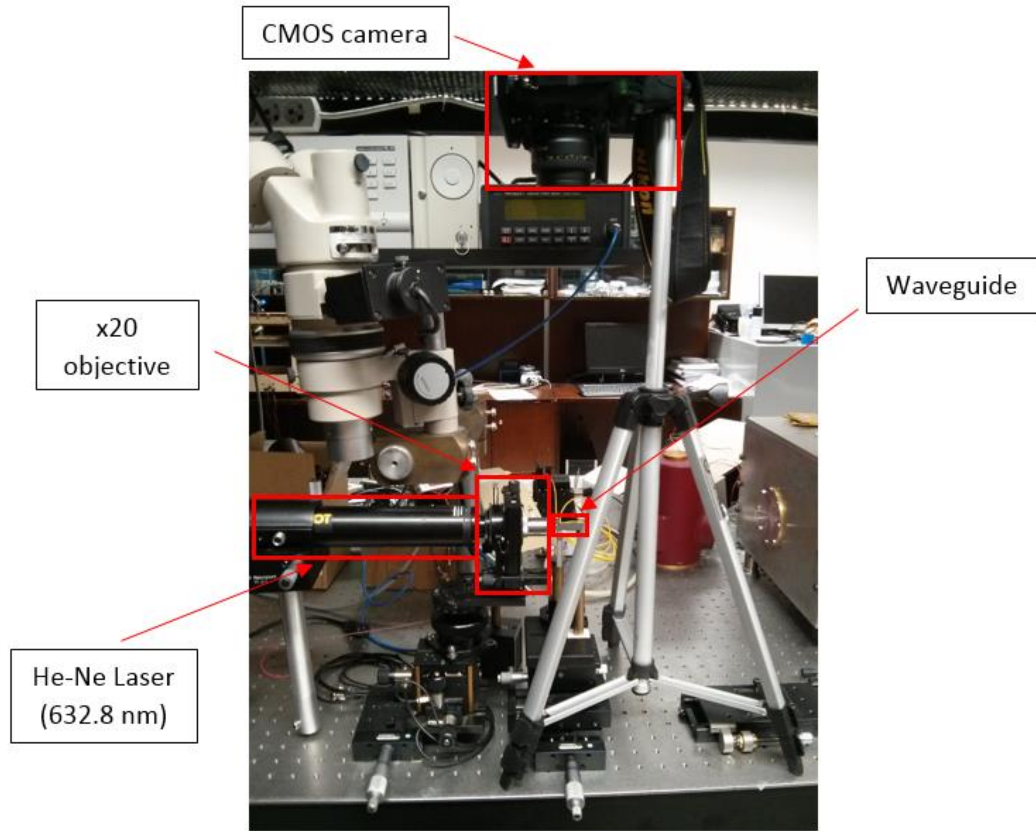

Figure 5.3 A photograph of experimental waveguide loss measurement setup

5.2. Linear Response Test of CMOS Camera

The camera must have linear response in order to get accurate results for evaluating light intensity variation with waveguide length, i.e. the optical loss. If the camera has nonlinear response. In order to test the linearity of the optical response off the camera, a novel technique based on digital image processing in MATLAB platform was used. Linearity response test technique of CMOS camera has two main steps. In first step, focused laser power is measured by using a calibrated power meter (silicon detector). Next, randomly selected optical filters are placed between the focused laser and laser power is measured by using the silicon detector. By changing the filters, two more measurement are done. Finally, all results are normalized at the range of 1 to 0. In the second step, the CMOS camera is directly

ANADOLU ÜNİVERSİTESİ

placed in front of the focused laser. The images are captured with no filter and same filters in step one. Digital image processing is applied to all raw images in a MATLAB platform. The images are read and converted to matrix. After, the summation of all red-green-blue (RGB) matrix values are calculated. Finally, all results are normalized at the range of 1 to 0.

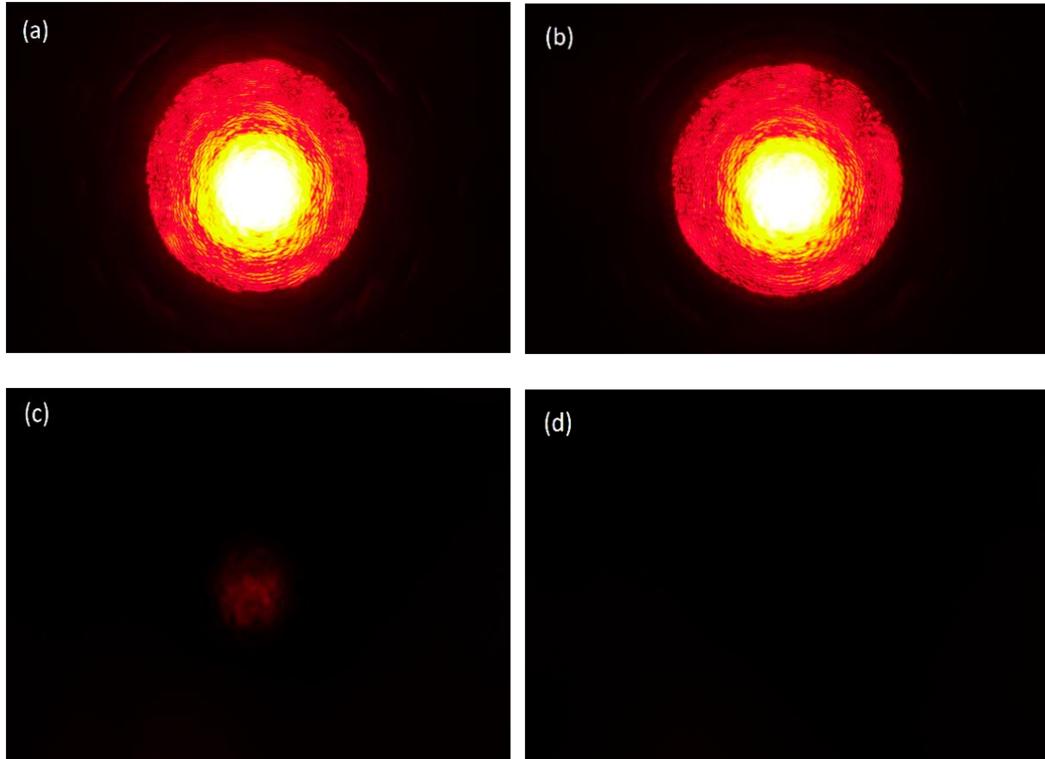

Figure 5.4 Different filter responses of CMOS camera (a) filter 0 (no filter), (b) filter 1 (c) filter 2 (d) filter 3

The response of CMOS camera for no filtering (filter 0), filter 1, filter 2 and filter 3 are given in Figure 5.3(a), Figure 5.3(b), Figure 5.3(c) and Figure 5.3(d), respectively. It must be mentioned that Figure 5.3(d) appears completely dark. It occurs because of limited perception of the human eye [189]. In fact, it contains a color code which is detected by CMOS camera. This is also valid for Figure 5.3(a), Figure 5.3(b) and Figure 5.3(c). The comparison of the normalized optical power and camera response at different optical filters is shown in Figure 5.4. The used filters which are long pass colored glass filters are manufactured from of Schott glass. For testing the linearity of CMOS camera different intensity is needed. Because of that the filters which have different transmission characteristics are

ANADOLU ÜNİVERSİTESİ

used. Figure 5.3(b), Figure 5.3(c) and Figure 5.3(d) are captured by using the Ø25 mm colored glass filters with 385 nm (filter 1), 721nm (filter 2) and 780 nm (filter 3) transmission characteristics, respectively.

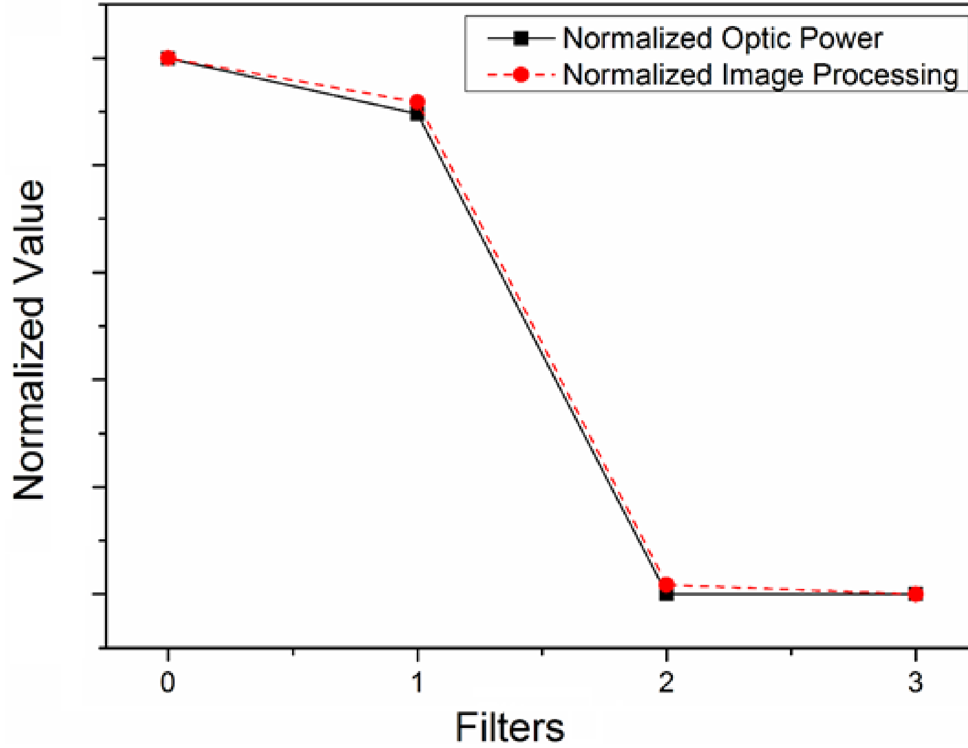

Figure 5.5 The comparison of normalized optic power and camera response for different filters

It must be mentioned that images are captured by using constant aperture (f/1.8) and focal length as given in Figure 5.3 and Figure 5.4. The exposure time of the each image is different because of optimum photo sensor value of CMOS camera. Moreover, we also tested constant aperture, focal length and exposure time. Both results show that the CMOS camera exhibits linear response for raw images.

5.3. Results

Light from a He-Ne laser (λ=632.8 nm) with an optical power of 1 mW and linearly polarized (TEM_0) is used a laser source. For coupling and focus the laser, x20 objective is used. A relatively clear image is captured by adjusting the CMOS camera system as shown in Figure 5.5. The constant aperture, focal length and exposure time of CMOS camera system used are f/1.8, 50 mm and 1/6 seconds, respectively. The length of the measured slab waveguide is ~3.2 cm.

ANADOLU ÜNİVERSİTESİ

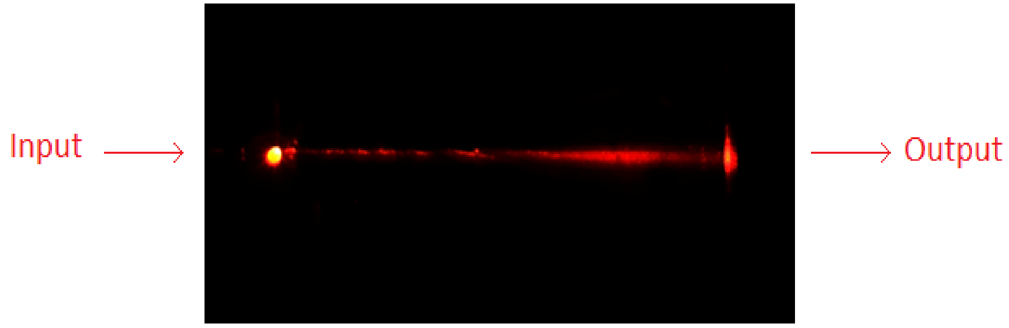

Figure 5.6 The captured image from CMOS camera of highly multimode planar waveguide

The loss analysis is performed by converting the captured 2-D image which includes scattered light along the propagation direction from the planar waveguide to the matrix in MATLAB platform. The captured raw image was imported to the MATLAB by using "*imread*" command which reads a grayscale or color image and converts the matrix. This matrix which has output class of "uint8" is format of *row x column x 3*. It must be mentioned that if the imported image is in color, MATLAB transfers it in RGB matrix. It means that the imported image converted to sum of 3 different matrix. Sum of these 3 matrix gives total relative intensity value of image which captured by CMOS camera. If you import grayscale image, again MATLAB program output format is same as *row x column x 3*. However, RGB matrix values are same. These matrix values are converted linearly 0 to 1 gray scale by MATLAB. For calculating the propagation loss, first, RGB matrices are summed then all column values are summed. Thus 1-D array is obtained. The relative intensity of each propagation point is calculated. By using the loss definition which is given in Equation (5.1), the logarithm of the relative scattered power versus the each propagation point is plotted. The relation between scattered light intensity and propagation loss can be expressed as the following [183]:

$$I_{d_1} = (I_{d0})\, exp(-\alpha(d_1 - d_2)) \tag{5.1}$$

where I_{d0} and I_{d_1} are the intensity of the scattered light, d_1 and d_2 are any points throughout the propagation length and α being the loss coefficient.

However, the captured images are not suitable for digital image processing because of high noise level. The reliable result cannot be obtained. Although three step cleaning process is applied repeatedly, a contamination of the substrate resulted

ANADOLU ÜNİVERSİTESİ

in unwanted regional scattering in the waveguide. This noise which possibly comes from the SiO_2/Al_2O_3 interface contamination. Nevertheless, the difference between input and output intensity did not seem relatively high. According to characterization results, the grown layers are expected to have good optical performance. It can also be inferred from the captured images that the propagation losses are actually. Based on this information, we can comment that ALD grown $Si/SiO_2/Al_2O_3$ planar waveguide have low loss.

ANADOLU ÜNİVERSİTESİ

6. CONCLUSION

In accordance with the aim of this study, i.e. utilization of aluminum oxide for silicon based photonics technology and its optimization for active and passive optical waveguide applications in integrated optics, the compositional and optical properties of these structures have been investigated.

ALD technique was used for growth of the Al_2O_3 films. The optimization of the growth process for optical waveguide application was performed. The Al_2O_3 films were deposited by varying the growth temperature between 150 and 300 °C in steps of 50 °C for purge times of 4 and 20 seconds, keeping N_2 flow rate constant at 20 sccm and number of the cycle at 500. The refractive index of the grown films varied between ~1.63 and 1.64 at a wavelength of 1550 nm. Moreover, the thicknesses of the films varied between ~54 and 60 nm, resulting at a growth rate of ~1.09 and 1.22 A/cycle.

Several characterization techniques were employed in order to get the structural analysis of the selected samples. The crystallinity investigation was done with X-ray Diffraction technique. The XRD observations showed that the ALD growth process of Al_2O_3 resulted in amorphous structure for all the samples. The structural properties of the layers were investigated via Fourier transform infrared transmission spectroscopy (FTIR). Unlike micro-Raman results, Al-O vibration modes were clearly observable in the IR spectrum between 400 and 1000 cm-1. Moreover, OH and carboxyl groups, which are basis of optical losses, decreased with increasing growth temperature. The Al_2O_3 layers grown at higher temperatures and low purge times possibly results in denser film and lower a-C:H bond concentrations. XPS was used in order to investigate the chemical structure of the layers. Depth profile measurements were done in order to get accurate results. The concentration of Al 2p, O 1s and Si 2p is observed as a function of etch depth. Using the concentration of the elements the stoichiometry of Al_2O_3 was calculated. The sample grown at 300 ºC with a purge time of 4 seconds had a stoichiometry of $Al_2O_{(3.02 \pm 0.15)}$, i.e. the desired Al/O ratio.

Design of $Si/SiO_2/Al_2O_3$ rib waveguides was investigated for both passive and active Applications. A “fabrication safe” parameter zone identified. The structural analysis was correlated with the growth process, thus the optimum growth

ANADOLU ÜNİVERSİTESİ

recipe was used for the design of the waveguides. Accordingly, the sample grown at 300 °C and purge time 4 seconds was chosen as a core material for planar and ridge waveguides. The refractive index of the chosen sample was n=1.645 and n= 1.639 at wavelengths of 633 and 1550 nm, respectively. The planar waveguide was realized according to the design. Light propagation was demonstrated in the slab waveguide at a wavelength of 632.8 nm.

6.1. Future Prospects and Suggestion

For ALD process, the pressure and pulse time of each precursor was keep constant at 500-600 mTorr (20 sccm) and 0.015 seconds. The effect of pressure and pulse time of each precursor can be investigated in order to further tune and optimize both growth rate and optical quality of the films, simultaneously. The high process pressure and pulse time can increase density of the film and growth of the process. Moreover, purge time effect was investigated at constant value for pulsing each precursor. It can be also analyzed for different purge time after pulsing each precursor. For waveguide fabrication, the passive ridge type waveguide should be fabricated in accordance with the design of this study. For optical loss measurement, the propagation loss measurement of passive waveguide should be completed for planar waveguides at 633 and 1550 nm. Moreover, The Al_2O_3 core ridge type waveguide should be measured for telecommunication wavelength. It must be mentioned that the cleaning process is crucial.

Besides all of them, our ultimate goal in the future is to obtain nanostructured active devices with superior performance based on ALD grown Al_2O_3. Because, large amount of rare earth ions can be homogeneously distributed into Al_2O_3 by using ALD compare with the other growth techniques. Thus, a better signal enhancement can be obtain compared with the other active devices which are published in the literature.

ANADOLU ÜNİVERSİTESİ

REFERENCES

[1] R. Hunsperger, Integrated Optics: Theory and Technology, Newark: Springer, 2002.

[2] Anonymous, Photonik Branchenreport, Spectaris, Vdma, Zvei, BMBF, Berlin, Frankfurt, 2013.

[3] M. Khan, Analysis of Metal-Clad TM Pass Polarizers using the Method of Lines, Dhahran: King Fahd University of Petroleum and Minerals, 2001.

[4] G. Reed ve A. Knights, Silicon Photonics: An Introduction, West Sussex: John Wiley & Sons, Ltd., 2004.

[5] K. Okamoto, Fundamentals of Optical Waveguides, California: Academic Press, 1992.

[6] C. Pollock ve M. Lipson, Integrated Optics, Boston, Dordrecht, London: Kluwer Academic, 2004.

[7] P. Persans, F. Huang, N. Agarwal, S. Ponoth ve J. Plawsky, Dielectric materials in optical waveguide applications, *Interlayer Dielectrics for Semiconductor Technologies,* pp. 349-389, 2003.

[8] Y. Naru ve H. Hayami, Replicated Polymer Optical Waveguides, *Proceedings of SPIE,* cilt 5246, pp. 103-111, 2003.

[9] H. Ma, K. Alex, Y. Jen ve L. Dalton, Polymer-Based Optical Waveguides: MAterials, Processing and Devices, *Advanced Materials,* pp. 1339-1365, 2002.

[10] R. Ulrich ve H. Weber, Solution-Deposited Thin Films as Passive and Active Light-Guides, *Applied Optics,* p. No.2, 1972.

[11] T. Van Eck, D. Girton, J. Valley, S. Ermer, A. Ticknor, G. Lipscomb ve R. Lytel, Chip-to-chip interconnects using poled polymer integrated optics transmitter networks, *SPIE Optoelectronics Interconnects,* cilt 1849, pp. 27-35, 1993.

[12] Y. Liu, . H. Cole, J. Bristow ve Y. Liu, Polymer-based Optical Interconnect Technology - A Route to Low-cost Optoelectronic Packaging and Interconnect, *SPIE Vol.2400,* pp. 80-88, 1995.

[13] M. Usui, M. Hikita, T. Watanabe, M. Amano, S. Sugarawa, S. Hayashida ve S. Imamura, Low-Loss Passive Polymer Optical Waveguides with High Environmental Stability, *Journal Of Lightwave Technology,* cilt 14, pp. 2338- 2343, 1996.

[14] K. Jang-Joo ve K. Jae-Wook, Thermally stable optical waveguide using polycarbonate, *SPIE Conference on Linear Optical Properties of Wavequides and Fibers,* p. Vol.3799, 1999.

[15] K. Glukh, J. Lipian, R. Mimna, S. Phillip, S. Neal, R. Ravikiran, L. F. Rhodes, R. A. Shick ve X. Zhao, High-performance polymeric materials for waveguide applications, *SPIE Linear, Nonlinear, and Power-Limtting Organics,* cilt 4106, pp. 43-53, 2000.

[16] M. Zhou, Low-loss polymeric materials for passive waveguide components in fiber optical telecommunication, *Opt. Eng. 41(7),* p. 1631–1643, 2002.

ANADOLU ÜNİVERSİTESİ

[17] K. Tamaki, H. Takase, Y. Eriyama ve T. Ukachi, Recent Progress on Polymer Waveguide Materials, *Jour. of Photopolymer Sci. and Tech.,* pp. 639-648, 2003.

[18] S. Imamura, Polymeric optical waveguides [materials, packaging and applications], *Broadband Optical Networks and Technologies,* pp. 35-36, 1998.

[19] A. Mekis, J. C. Chen, I. Kurland, S. Fan, P. R. Villeneuve ve J. D. Joannopoulos, High Transmission through Sharp Bends in Photonic Crystal Waveguides, *Physical Revıew Letters,* cilt 77, pp. 3787-3790, 1996.

[20] B. Temelkuran ve E. Ozbay, Experimental demonstration of photonic crystal based waveguides, *Applied Physics Letters,* cilt 74, pp. 486-488, 1999.

[21] P. Tien ve R. Ulrich, Theory of Prism-Film Coupler and Thin-Film Light Guides, *Journal of the Optical Society of America,* pp. 1325-1337, 1970.

[22] P. Tien, Light Waves in Thin Films and Integrated Optics, *Applied Optics,* pp. 2395-2413, 1971.

[23] R. Deri ve E. Kapon, Low-loss III–V semiconductor optical waveguides, *IEEE J. Quant. Electron. 27,* p. 626–640, 1991.

[24] D. Fluck, F. Fleuster, R. Irmscher, P. Gunter ve C. Buchal, Formation of planar and strip waveguides in KNbO3 by He ion implantation, *Mater. Res. Soc. Symp. Proc. 244,* p. 331–336, 1992.

[25] B. Bae, W. Lee, K. No, D. Yoon ve S. Kim, Optical properties of sol–gel (Pb,La)TiO3 thin films for waveguide application, *Mater. Res. Soc. Symp. Proc. 392,* p. 279–285, 1995.

[26] M. Seto ve e. al, GaAs/AlGaAs single-mode optical waveguides with low propagation loss and strong optical confinement, *App. Phy. Letters,* cilt 56, p. 990, 1990.

[27] A. D. Ferguson ve e. al, Low-loss, single-mode GaAs/AlGaAs waveguides, *IEE Proc.-Optoelectron.,* cilt 153, pp. 51-56, 2006.

[28] Y. T. Byun ve e. al, Single-mode GaAs/AlGaAs W waveguides with a low propagation loss, *App. Optics,* cilt 35, no. 6, pp. 928-933, 1996.

[29] P. Mcllroy ve e. al, Low-loss single-mode InP/InGaAsP waveguides grown by MOVPE, *Electronics Letters,* cilt 23, no. 13, pp. 701-703, 1987.

[30] M. Pospiech ve S. Liu, Laser Diodes an Introduction, University of Hannover,, Hannover, Germany, 2004.

[31] J. Bradley, F. Ay, K. WöRhoff ve M. Pollnau, Fabrication of low-loss channel waveguides in Al2O3 and Y2O3 layers by inductively coupled, *Appl. Phys. B 89,* p. 311–318, 2007.

[32] A. Polman, J. Appl. Phys., *J. Appl. Phys.,* p. 82, 1997.

[33] J. Bradley, D. Geskus, T. Blauwendraat, F. Ay, K. Wörhoff ve M. Pollnau, Optimized Deposition and Structuring of Reactively Co-Sputtered Al2O3:Er Waveguide Layers with Net Optical Gain, *12th Annual Symposium IEEE/LEOS Benelux,* pp. 107-110, 2007.

ANADOLU ÜNİVERSİTESİ

[34] X. Du, T. Touam, L. Degachi, J. Guibault, M. Andrews ve S. Najafi, Sol-gel waveguide fabrication parameters: an experimental investigation, *Opt. Eng. 37(4),* pp. 1101-1104, 1998.

[35] K. Wörhoff, B. Offrein, P. Lambeck, G. Bona ve A. Driessen, Birefringence Compensation Applying Double-Core Waveguiding Structures, *IEEE Photonics Technology Letters,* pp. 206-208, 1999.

[36] T. Miya, Silica-Based Planar Lightwave Circuits: Passive and Thermally Active Devices, *IEEE Journal of Selected Topics in Quantum Electronics,* pp. 38-45, 2000.

[37] A. Kilian, J. Kirchhof, B. Kuhlow, G. Przyrembel ve W. Wischmann, Birefringence Free Planar Optical Waveguide Made by Flame Hydrolysis Deposition (FHD) Through Tailoring of the Overcladding, *Journal of Lightwave Technology,* pp. 193-198, 2000.

[38] S. Selvaraja, E. Sleeckx, M. Schaekers, W. Bogaerts, D. Thourhout, P. Dumon ve R. Baets, Low-loss amorphous silicon-on-insulator technology for photonic integrated circuitry, *Optics Communications,* pp. 1767-1770, 2009.

[39] L. Binh, . R. Netterfield ve P. Martin, Low loss waveguiding in ion-assisted deposited thin films, *Appl. Surf. Sci.,* p. 1995, 22-23.

[40] Anonymous, Rare Earth Elements: A Review of Production, Processing, Recycling, and Associated Environmental Issues, EPA, Cincinnati, OH, 2012.

[41] J. Yang, Neodymium-doped Waveguide Amplifiers and Lasers for Integrated Optical Applications, PhD, The Netherlands: University of Twente, 2010.

[42] P. Kik ve A. Polman, Erbium doped optical waveguide amplifiers on silicon, *MRS Bulletin 23(4),* p. 48, 1998.

[43] J. Bradley, Al2O3:Er3+ as a Gain Platform for Integrated Optics, PhD, The Netherlands: University of Twente, 2009.

[44] G. Pieter, Energy transfer in erbium doped optical waveguides based on silicon, The Nertherlands: University of Utrecht, 2000.

[45] Y. Yan, Optical Waveguide Amplifiers Based on Er-doped Phosphate Glasses, PhD, The Nertherlands: Technic University of Eindhoven, 1999.

[46] S. Qhumayo, R. Manuel ve J. M. Kaboko , A Multi-wavelength Erbium Doped Fiber Laser for Free Space Optical Communication link, *2. Core Network Tech. (SATNAC),* pp. 1-5, 2012.

[47] G. Keiser, Optical Fiber Communications, 3rd dü., Singapure: McGraw-Hill Higher Education, 2000.

[48] H. Kim, S. Yun, H. Kim, N. Park ve B. Kim, Actively gainflattened Erbium-Doped Fiber Amplifier over 35 nm by using all fiber Acoustooptic tunable filters, *IEEE Photonics Tech. Letters,* cilt 10, pp. 790-792, 1998.

[49] V. Wongpaibool, Effect of dispersion on spectrum-sliced WDM systems, Virginia : Virginia Polytechnic Ins. and State University, 1998.

ANADOLU ÜNİVERSİTESİ

[50] J. D. B. Bradley, R. Stoffer, L. Agazzi, F. Ay, K. Wörhoff ve M. Pollnau, Integrated Al2O3:Er3+ ring lasers on silicon with wide wavelength selectivity, *Optics Letters,* cilt 35, no. 1, pp. 73-75, 2010.

[51] W. Sohler, Erbium-Doped Lithium Niobate Waveguide Laser, *Lasers and Electro-Optics Europe,* p. 380, 2000.

[52] Y. C. Yan, A. J. Faber, H. de Waal, P. G. Kik ve A. Polman, Erbium-doped phosphate glass waveguide on silicon with 4.1 dB/cm gain at 1.535 um, *Appl. Phys. Lett. 71,* p. 20, 1997.

[53] M. Waldmann, R. Caspary, D. Esser, D. Wortmann, J. Gottmann ve W. Kowalsky, Erbium-doped fluoride glass waveguides, *Transparent Optical Networks,* cilt 3, pp. 219-222, 2008.

[54] J. I. Mackenzie, G. S. Murugan, T. Suzuki, Y. Ohishi, A. Yu ve J. Abshire, Er-doped Tellurite glasses for planar waveguide power amplifier with extended gain bandwidth, *SPIE Solid State Lasers XXI: Technology and Devices,* 2012.

[55] K. Wörhoff, J. D. B. Bradley, F. Ay, D. Geskus, T. P. Blauwendraat ve M. Pollnau, Reliable Low-Cost Fabrication of Low-Loss Al2O3:Er3+ Waveguides With 5.4-dB Optical Gain, *IEEE Journal Of Quantum Electronics,* cilt 45, pp. 454-461, 2009.

[56] T. Hoekstra, P. Lambeck, H. Albers ve T. Popma, Sputter-deposited erbium-doped Y2O3 active optical waveguides, *Electronics Letters,* pp. 581-583, 1993.

[57] K. Van Dalfsen, Nd:Al2O3 as a gain material for integrated devices, The Netherlands: University of Twente, 1986.

[58] M. Smit, G. Acket ve C. van der Laan, Al2O3 films for integrated optics, *Thin Solid Films,* pp. 171-181, 1986.

[59] G. N. van den Hoven, E. Snoeks, . A. Polman, J. W. M. van Uffelen, Y. S. Oei ve M. K. Smit, Photoluminescence characterization of Er-implanted A1203 films, *Appl. Phys. Lett.,* pp. 3065-3067, 1993.

[60] S. Li, C. Song, Q. J. Xiong ve B. Ran, A numerical analysis of gain characteristics of Er-doped Al2O3 waveguide amplifiers, *Optical and Quantum Electronics,* p. 859–866, 2002.

[61] P. G. Kik ve A. Polman, Cooperative upconversion as the gain-limiting factor in Er doped miniature Al2O3 optical waveguide amplifiers, *Journal Of Applıed Physıcs,* cilt 93, 2003.

[62] J. D. B. Bradley ve M. Pollnau, Erbium-doped integrated waveguide amplifiers and lasers, *Laser Photonics,* p. 368–403, 2011.

[63] J. D. B. Bradley, L. Agazzi, D. Geskus, F. Ay, K. Wörhoff ve M. Pollnau, Gain bandwidth of 80 nm and 2 dB/cm peak gain in Al2O3:Er3+ optical amplifiers on silicon, *J. Opt. Soc. Am. B,* cilt 27, pp. 187-196, 1020.

[64] K. Hattori, T. Kitagawa, K. Shuto, M. Oguma ve Y. Ohmori, Optical and structural properties of Er3+-doped P2O5–SiO2 and Al203–SiO2 planar waveguides, *Materials Science and Engineering,* p. 15–17, 1998.

ANADOLU ÜNİVERSİTESİ

[65] Q. Xiang, Y. Zhou, B. Ooi, Y. Lam, Y. Chan ve C. Kam, Optical properties of Er31-doped SiO2-GeO2-Al2O3 planar waveguide fabricated by sol-gel processes, *Thin Solid Films,* pp. 243-247, 2000.

[66] P. Camy, J. E. Roman, F. W. Willems, M. Hempstead, J. C. vanderPlaats, C. Prel, A. Beguin, A. M. J. Koonen, J. S. Wilkinson ve C. Lerminiaux, Ionexchanged planar lossless splitter at 1.5 µm, *Electronics Letters,* cilt 32, pp. 321-323, 1996.

[67] Z. He, Y. G. Li, Y. W. Zhang, D. X. Li, L. Y. Liu ve L. Xu, Er3+/Yb3+ codoped waveguide amplifier and lossless power splitter fabricated by a two-step ion exchange on a commercial phosphate glass, *Journal of the Korean Physical Society,* cilt 49, pp. 2159-2163, 2006.

[68] M. W. Sckerl, S. Guldberg-Kjær, C. Laurent-Lund ve M. R. Poulsen, Lossless planar waveguide 1:4 power splitter at 1550 nm, *presented at Proceedings of ECOC,* 1999.

[69] Y. Jaouën, L. du Mouza, D. Barbier, J. Delavaux ve P. Bruno, Eightwavelength Er-Yb doped amplifier: combiner/splitter planar integrated module, *IEEE Photonics Technology Letters,* cilt 11, pp. 1105-1107, 1999.

[70] P. M. Peters, . D. S. Funk, A. P. Peskin, D. L. Veasey, N. A. Sanford, S. N. Houde-Walter ve J. S. Hayden, Ion-exchanged waveguide lasers in Er3+/Yb3+ codoped silicate glass, *Applied Optics,* cilt 38, pp. 6879-6886, 1999.

[71] D. L. Veasey, D. S. Funk, N. A. Sanford ve J. S. Hayden, Arrays of distributed-Bragg-reflector waveguide lasers at 1536 nm in Yb/Er codoped phosphate glass, *Applied Physics Letters,* cilt 74, pp. 789-791, 1999.

[72] G. Sorbello, S. Taccheo, P. Laporta, O. Svelto, E. Cianci, V. Foglietti, S. Jiang ve N. Peyghambarian, Singlemode Er:Yb waveguide laser array at 1.5 µm, *Electronics Letters,* cilt 37, pp. 1014-1015, 2001.

[73] T. Feuchter, E. K. Mwarania, J. Wang, L. Reekie ve J. S. Wilkinson, Erbiumdoped ion-exchanged waveguide lasers in Bk-7 glass, *IEEE Photonics Technology Letters,* cilt 4, pp. 542-544, 1992.

[74] K. P. Almtoft, Structural Characterization of Nanocrystalline Thin Films Grown by Magnetron Sputtering, PhD Thesis, University of Aarhus, Denmark, 2006.

[75] A. J. G. Schellingerhout, Advanced Electron Beam Evaporation, PhD Thesis, 1988.

[76] R. J. O'Haire, Growth by Pulsed Laser Deposition and Characterisation of Zinc Oxide Thin Films and Nanostructures, PhD Thesis, Dublin City University, Dublin, 2009.

[77] R. F. C. Farrow, Molecular Beam Epitaxy: Applications to Key Materials, Elsevier Science, 2012.

[78] L. Yang, Fabrication and Characterization of Microlasers by the Solgel Method, PhD Thesis, California, 2005.

[79] H. J. Scheel, Introduction to Liquid Phase Epitaxy, %1 içinde *Liquid Phase Epitaxy of Electronic, Optical and Optoelectronic Materials*, John Wiley & Sons Ltd., 2007, pp. 1-17.

ANADOLU ÜNİVERSİTESİ

[80] G. A. Luurtsema, Spin coating for rectangular substrates, California: Electronics Research Laboratory, University of California, 1997.

[81] A. C. Jones ve M. L. Hitchman, Chemical Vapour Deposition : Precursors, Processes and Applications, RSC Publishing, 2009.

[82] T. Kaariainen, D. Cameron, M. Kaariainen ve A. Sherman, Atomic Layer Deposition: Principles, Characteristics, and Nanotechnology Applicatons, 2nd Edition, John Wiley & Sons, 2013.

[83] N. Pinna ve M. Knez, Atomic Layer Deposition of Nanostructured Materials, John Wiley & Sons, 2011.

[84] K. Wasa, Handbook of Sputter Deposition Technology, William Andrew, 2012.

[85] D. M. Mattox, Handbook of Physical Vapor, William Andrew, 2010.

[86] T. Raimondo, S. Puckett ve T. J. Webster, Greater osteoblast and endothelial cell adhesion on nanostructured polyethylene and titanium, *International Journal of Nanomedicine,* cilt 5, pp. 647-652, 2010.

[87] A. Garg, Growth and Characterization of Epitaxial Oxide Thin Films, PhD thesis, , Cambridge, 2001.

[88] C. C. Uhuegbu, Growth and characterization of ternary chalcogenide thin films for efficient solar cells and possible industrial applications, PhD Thesis, Ota Ogun State, 2007.

[89] J.-H. Park ve T. S. Sudarshan, Chemical Vapor Deposition, %1 içinde *Introduction to Chemical Vapor Deposition (CVD)*, ASM International, 2001, pp. 1-11.

[90] T. Blanquart, Atomic Layer Deposition of Groups 4 and 5 Transition Metal Oxide Thin Films: Focus on Heteroleptic Precursors., PhD Thesis, Helsinki, 2013.

[91] G. A. Baker, Advanced Materials, Weinheim: WILEY-VCH Verlag GmbH & Co., 2004.

[92] D. L. Heineman, Optimization of ald grown titania thin films for the infiltration of silica photonic crystals, MSc Thesis, Georgia Institute of Technology, Georgia, 2004.

[93] G. Higashi ve C. G. Fleming, Sequential surface chemical reaction limited growth of high quality Al2O3 dielectrics, *Applied Physics Letters,* cilt 55, no. 19, pp. 1963-1965, 1989.

[94] S. Yun ve a. et, Dependence of atomic layer-deposited Al2O3 films characteristics on growth temperature and Al precursors of Al(CH3)3 and AlCl3, *Journal of Vacuum Science & Technology A,* cilt 15, pp. 2993-2997, 1997.

[95] J. F. Fan ve K. Toyoda, Growth-Temperature Dependence of the Quality of Al2O3 Prepared by Sequential Surface Chemical Reaction of Trimethylaluminum and H2O2, *J. Appl. Phys.,* cilt 32, pp. 1349-1351, 1993.

[96] J. Fan, K. Sugika ve K. Toyoda, Low-Temperature Growth of Thin Films of Al2O3 by Sequential Surface Chemical Reaction of trimethylaluminum and H2O2, *Japanese J. of App. Phy.,* cilt 30, pp. 1139-1141, 1991.

ANADOLU ÜNİVERSİTESİ

[97] M. D. Groner, F. H. Fabreguette, J. W. Elam ve S. M. George, Low-Temperature Al2O3 Atomic Layer Deposition, *Chem. Mater.,* cilt 16, pp. 639-645, 2004.

[98] A. W. Ott, K. C. McCarley, J. W. Klaus, J. D. Way ve S. M. George, Atomic layer controlled deposition of A1203 films using binary reaction sequence chemistry, *Applied Surface Science,* cilt 107, pp. 128-136, 1996.

[99] M. Leskela ve M. Ritala, Atomic layer deposition (ALD): from precursors to thin film structures, *Thin Solid Films,* cilt 409, p. 138–146, 2002.

[100] A. R. Barron, Atomic Layer Deposition, Rice University, 2009.

[101] G. He ve Z. Sun, High-k Gate Dielectrics for CMOS Technology, Wiley-VCH Verlag GmbH & Co., 2012.

[102] E. M. Yeatman, K. Pita ve M. M. Ahmad, Strip-Loaded High-Confinement Waveguides for Photonic Applications, *Journal of Sol-Gel Science and Technology,* cilt 13, pp. 517-521, 1998.

[103] M. Melchiorri ve e. all, Propagation losses of silicon nitride waveguides in the near-infrared range, *App. Phy. Letters,* cilt 86, p. 121111, 2005.

[104] H. Moshe ve Y. Mastai, Atomic Layer Deposition on Self-Assembled-Monolayers, %1 içinde *Materials Science - Advanced Topics*, Intech, 2013, pp. 63-84.

[105] R. Matero, Atomic Layer Deposition of Oxide Films – Growth, Characterisation and Reaction Mechanism Studies, PhD Thesis, 2004.

[106] G. Este ve D. Westwood, *J. Vac. Sci. Technol. A,* cilt 2, pp. 1238-1247, 1984.

[107] M. Mahnke, S. Wiechmann, H. Heider, O. Blume ve J. Muller, Aluminum oxide doped with erbium, titanium and chromium for active integrated optical applications, *AEU-Int. J. of Elec. and Comm.,* cilt 55, no. 5, pp. 342-348, 2001.

[108] A. Suarez-Garcia, J. Gonzalo ve C. Afonso, Low-loss Al2O3 waveguides produced by pulsed laser deposition at room temperature, *Appl. Phys. A 77,* p. 779–783, 2003.

[109] M. M. Aslan, N. A. Webster, C. L. Byard, M. B. Pereira, C. M. Hayes, R. S. Wiederkehr ve S. B. Mendes, Low-Loss Optical Waveguides for the Near Ultra-Violet and Visible Spectral Regions with Al2O3 Thin Films from Atomic Layer Deposition, *Thin Solid Films,* cilt 518, no. 17, p. 4935–4940, 2010.

[110] T. Motooka, S. Gorbatkin ve e. al, Mechanisms of Al film growth by ultraviolet laser photolysis of trimethylaluminum, *J. Vac. Sci. Technol.,* cilt 6, pp. 3146-3152, 1986.

[111] Anonymous, Camb. Savannah 100&200 ALD System User Manual, Cambridge NanoTech Inc., Cambridge, 2007.

[112] W. Yuan, Variable-Angle Spectroscopic Ellipsometry Of InAlP Native Oxide Gate Dielectric Layers For GaAs Mosfet Applications, MSc Thesis, Notre Dame, Indiana, 2009.

[113] Anonymous, Guide to using Wvase Spectroscopic Ellipsometry Data Acquisition and Analysis Software, J.A. Wooloam Co., Inc., Lincoln, 2012.

ANADOLU ÜNİVERSİTESİ

[114] C. L. Waxler, Ellipsometric Analysis of Silicon Nanoparticles Formed by Thermal Annealling, MSc Thesis, San Marcos, Texas, 2013.

[115] S. M. George, A. W. Ott and J. Klaus, Surface Chemistry for Atomic Layer Growth, *J. Phys. Chem.,* vol. 100, pp. 13121-13131, 1996.

[116] A. C. Dillon, A. W. Ott, J. D. Way ve S. M. George, Surface chemistry of Al2O3 deposition using Al(CH3)3 and H2O in a binary reaction sequence, *Surface Science,* cilt 322, pp. 230-242, 1995.

[117] L. T. Zhuravlev, The surface chemistry of amorphous silica. Zhuravlev model, *Colloids and Surfaces,* cilt 173, pp. 1-38, 2000.

[118] G. Liu, X-ray Diffraction from Thin Film Structures:Characterization and Modeling, PhD Thesis, San Diego, 2007.

[119] A. E. Muhsin, Chemical Vapor Deposition of Aluminium Oxide (Al2O3) and Beta Iron Disilicide (β-FeSi2) Thin Films, PhD Thesis, Zliten / Libyen, 2007.

[120] J. I. Ramadan, Settlement of Dry Cohesionless Soil Deposits Under Earthquake Induced Loading, PhD Thesis, California, 2007.

[121] S. Tatumi, A. Ventieri, J. Bitencourt, K. Gonçalves, J. Mittani, R. Rocca ve S. Camargo, Effects of Heat Treatments on the Thermoluminescence and Optically Stimulated Luminescence of Nanostructured Aluminate Doped with Rare-Earth and Semi-Metal Chemical Element, %1 içinde *Heat Treatment - Conventional and Novel Applications*, InTech, 2012, pp. 177-196.

[122] T. Teng, Y. Hung, T.-C. Teng ve J. Chen, Performance evaluation on an air-cooled heat exchanger for alumina nanofluid under laminar flow, *Nanoscale Research Letters,* cilt 6, pp. 1-11, 2011.

[123] S. López, J. Rodríguez ve S. Sueyoshi, Low-Temperature Formation of Alpha Alumina Powders via Metal Organic Synthesis, *The Azo Journal of Materials Online,* cilt 2, 2006.

[124] M. R. Abel, Thermal Metrology of Poltsilicon Mems Using Raman Spectroscopy, MSc Thesis, Georgia, 2005.

[125] Anonymous, WITec Control Scanning and Data Acquisition Software- User Manual, WITec Wissenschaftliche Instrumente und Technologie GmbH, Ulm, 2007.

[126] I. E. Wachs, Raman and IR studies of surface metal oxide species on oxide supports: Supported metal oxide catalysts, *Catalysis Today,* cilt 27, pp. 437-455, 1996.

[127] J. E. Villarreal-Barajas, L. Escobar-Alarcón, E. Camps, P. González, E. Villagrán ve M. Barboza-Flores, Thermoluminescence response of aluminum oxide thin films to beta-particle and UV radiation, *Superficies y Vacío,* cilt 13, pp. 126-129, 2001.

[128] J.-Y. Lee, B.-C. Kang, D.-Y. Jung ve J.-H. Boo, Selective growth of iron oxide thin films using the combined method of metal-organic chemical vapor deposition and microcontact printing, *Microelectronics and Nanometer Structures,* pp. 1516-1519, 2007.

ANADOLU ÜNİVERSİTESİ

[129] J. E. Villarreal-Barajas, L. Escobar-Alarcón, E. Camps, P. González, E. Villagrán ve M. Barboza-Flores, Thermoluminescence properties of aluminum oxide thin films obtained by pulsed laser deposition, *Radiation Measurements,* cilt 35, p. 355 – 359, 2002.

[130] M. Kadleikova, J. Breza ve M. Vesely, Raman spectra od synthetic sapphire, *Microelectrnics Journal,* cilt 32, pp. 955-958, 2001.

[131] S. Trusso, C. Vasi, F. Barreca ve F. Neri, Micro-Raman study of reactive pulsed laser ablation deposited silicon carbon alloy films, *J. Vac. Sci. Technol.,* cilt 5, pp. 3020-3024, 1998.

[132] P. Borowicz, A. Taube, W. Rzodkiewicz, M. Latek ve S. GieraBtowska, Raman Spectra of High-κ Dielectric Layers Investigated with Micro-Raman Spectroscopy Comparison with Silicon Dioxide, *The ScientificWorld Journal,* cilt 2013, pp. 1-6, 2013.

[133] E. Quiroga-Gonzalez, J. Carstensen, C. Glynn, C. O'Dwyer ve H. Föll, Pore size modulation in electrochemically etched macroporous p-type silicon monitored by FFT impedance spectroscopy and Raman scattering, *Royal Society of Chemistry,* cilt 16, pp. 255-263, 2014.

[134] A. Zwick ve R. Carles, Multiple-order Raman scattering in crystalline and amorphous silicon, *Physical Review,* cilt 48, pp. 6024-6032, 1993.

[135] S. Mestanza, J. Swart , I. Doi ve N. Frateschi, Synthesis of Ge Nanocrystals Grown by Ion Implantation and Subsequent Annealing, *International Caribbean Conference on Devices, Circuits and Systems,* pp. 151-155, 2006.

[136] G. Jovanovski, P. Makreski, B. Kaitner ve B. Boev, Silicate Minerals from Macedonia Complementary Use of Vibrational Spectroscopy and X-ray Powder Diffraction for Identification and Detection Purposes, *Croat. Chem. Acta,* cilt 82, p. 363–386, 2009.

[137] J. Schwan, S. Ulrich, V. Batori, H. Ehrhardt ve S. P. Silva, Raman spectroscopy on amorphous carbon films, *J. Appl. Phys.,* cilt 80, pp. 440-447, 1996.

[138] M. Marton, M. Vojs, E. Zdravecká, M. Himmerlich, T. Haensel, S. Krischok, M. Kotlár, P. Michniak, M. Veselý ve R. Redhammer, Raman Spectroscopy of Amorphous Carbon Prepared by Pulsed Arc Discharge in Various Gas Mixtures, *Journal of Spectroscopy,* cilt 2013, pp. 1-6, 2013.

[139] G. Sarau, A. Bochmann, R. Lewandowska ve S. Christiansen, From Micro– to Macro–Raman Spectroscopy: Solar Silicon for a Case Study, *Advanced Aspects of Spectroscopy*, Intech, 2012, pp. 221-246.

[140] B. Stuart, Infrared Spectroscopy: Fundamentals and Applications, John Wiley & Sons, Ltd, 2004.

[141] U. o. Colorado, Infrared Spectroscopy: Theory, 2002, pp. 155-163.

[142] F. Ay, Silicon Oxynitride Layers for Applications in Optical Waveguides, Msc Thesis, Ankara, 2000.

[143] W. M. Linhart, Electron accumulation and doping in InN and InGaN alloys, PhD Thesis, 2012.

[144] M. C. Schmittdiel, Talkactive Control of a Diffraction Grating Interferometer for Microscale Devices, MSc Thesis, 2004.

ANADOLU ÜNİVERSİTESİ

[145] B. Ivanova ve T. Kolev, Linearly Polarized IR Spectroscopy: Theory and Applications for Structural Analysis, CRC Press, 2011.

[146] Z. Ghezelbash, D. Ashouri, S. Mousavian, A. H. Ghandi ve Y. Rahnama, Surface modified Al2O3 in fluorinated polyimide/Al2O3 nanocomposites: Synthesis and characterization, *Bull. Mater. Sci.,* cilt 35, no. 6, pp. 925-931, 2012.

[147] J. M. Reyes, B. M. P. Ramos, C. Z. Islas, W. C. Arriaga, P. R. Quintero ve A. T. Jacome, Chemical and Morphological Characteristics of ALD Al2O3 Thin-Film Surfaces after Immersion in pH Buffer Solutions, *Journal of The Electrochemical Society,* cilt 160, no. 10, pp. B201-B206, 2013.

[148] D. Voll, P. Angerer, A. Beran ve H. Schneider, A new assignment of IR vibrational modes in mullite, *Vibrational Spectroscopy,* cilt 30, p. 237–243, 2002.

[149] K. J. D. MacKenzie, Infrared Frequency Calculations for Ideal Mullite (3A1,03-2Si0, *Journal of The American Ceramic Society,* cilt 55, no. 2, pp. 68-71, 1972.

[150] K. H. Tan, Principles of Soil Chemistry- Fourth Edition, CRC Press, 2011.

[151] F. Carrillo, X. Colom, J. J. Sunol ve J. Saurina, Structural FTIR analysis and thermal characterisation of lyocell and viscose-type fibres, *European Polymer Journal,* cilt 40, p. 2229–2234, 2004.

[152] A. Rajaeiyan ve M. M. Bagheri-Mohagheghi, Comparison of sol-gel and co-precipitation methods on the structural properties and phase transformation of c and a-Al2O3 nanoparticles, *Adv. Manuf.,* p. 176–182, 2013.

[153] W. G. Golden, S. Douglas, C. E. Pavlik ve J. Overend, The observation of the 1875 cm-1 band in the IR spectrum of CO on polycrystalline Pt, *J. Chem. Phys. ,* cilt 70, no. 9, p. 4426, 1979.

[154] F. Mathey, Transition Metal Organometallic Chemistry, Springer, 2013.

[155] B. Gong ve G. N. Parsons, Quantitative in situ infrared analysis of reactions between trimethylaluminum and polymers during Al2O3 atomic layer deposition, *Journal of Materials Chemistry,* cilt 22, pp. 15672-15682, 2012.

[156] C. S. Fadley, Basic Consecpts of X-ray Photoelectron Spectroscopy,*Electron Spectroscopy Theory, Techniques and Applications*, Academic Press, 1978, pp. 2-145.

[157] E. Willet, The Basics of Quantum Physics, The Rosen Publishing Group, 2004.

[158] S. Thiruvengadam, Characterization and Analysis of Hybrid Electronic Materials for Molecular Based Devices, MSc Thesis, India, 2007.

[159] M. Borasio, Polarization Modulation Infrared Reflection Absorption Spectroscopy on Pd Model Catalysts at Elevated Pressure, PhD Thesis, Berlin, 2006.

[160] İ. Doğan, Fabrıcation And Characterization Of Aluminum Oxide And Silicon/Aluminum Oxıde Films with Si Nanocrystals Formed by Magnetron Co-Sputtering Technique, MSc Thesis, METU, Ankara, 2008.

ANADOLU ÜNİVERSİTESİ

[161] A. A. Pradhan, I. Shah ve K. M. Unruh, Reactive sputter deposition of alumina thin films using a hollow cathode sputtering source, *Rev. Sci. Instrum.,* cilt 73, p. 3841, 2002.

[162] C. J. Park, Y. H. Kwon ve e. al, "Origin of luminescence from Si-implanted (1-102) Al2O3, *Appl. Phys. Lett.,* cilt 84, pp. 2667-2669, 2004.

[163] R. A. Soref, J. Schmidtchen ve K. Petermann, Large Single-Mode Rib Waveguides in GeSi-Si and Si-on-SiO2, *IEEE Journal of Quantum Electronics,* cilt 27, no. 8, pp. 1971-1974, 1991.

[164] N. M. Kassim, A. B. Mohammad, A. S. M. Supa'at, M. H. Ibrahim ve S. Y. Gang, Single Mode Rib Optical Waveguide Modeling Techniques, *RF and Microwave Conference*, Subang, Selangor, 2004.

[165] M. de Laurentis, A. Irace ve G. Breglio, Determination of single mode condition in dielectric rib waveguide with large cross section by finite element analysis, *J. Comput. Electron,* cilt 6, p. 285–287, 2007.

[166] J. Duan, J. Wang, B. Zhang ve Y. Ren, Optimizing Design of a Single-Mode Optical Rib Waveguide, *Advanced Materials Research,* cilt 710, pp. 464-468, 2013.

[167] K. Solehmainen, M. Kapulainen, P. Heimala ve K. Polamo, Erbium-Doped Waveguides Fabricated With Atomic Layer Deposition Method, *IEEE Photonics Technology Letters,* cilt 16, no. 1, pp. 194-196, 2004.

[168] M. Demirtaş, A. Özden ve F. Ay, Optimization of ALD grown Al2O3 Host Material for Use in Integrated Optical Circuits,*Nanotr10*, Istanbul, 2014.

[169] M. Bass, C. DeCusatis ve e. al, Handbook of optics. 3rd Edition, McGraw Hill Professional, 2009.

[170] R. Scarmozzino, A. Gopinath ve e. al, Numerical techniques for 4 modeling guided-wave photonic devices, *IEEE J. Sel. Topics Quantum Electron,* cilt 6, pp. 150-162, 2000.

[171] D. Yevick, A guide to electric-field propagation techniques for guided-wave optics, *Opt. Quant. Electron.,* cilt 26, pp. 185-197, 1994.

[172] K. S. Chiang, Review of numerical and approximate methods for the modal 9 analysis of general optical dielectric waveguides, *Opt. Quant. Electron.,* cilt 26, pp. 133-134, 1994.

[173] G. Hadley, Transparent boundary condition for the beam propagation method, *J. 12 Quantum Electron.,* cilt 28, pp. 363-370, 1992.

[174] L. Vivien, S. Laval ve e. al, Polarization independent single-mode rib waveguides on silicon-on-insulator for telecommunication wavelengths, *Opt Commun.,* cilt 210, pp. 43-49, 2002.

[175] C. Pollock, Fundamentals of Optoelectronics, Richard D Irwin Inc., 1994.

[176] O. Watanabe, M. Tsuchimori ve e. al, Mode selective polymer channel 18 waveguide defined by the photoinduced change in birefringence, *Appl. Phys. Lett.,* cilt 70, pp. 750-752, 1997.

[177] S. Ohke, T. Umeda ve e. al, TM-mode selective filter using leaky waveguide 21 structure, *Electron. Comm.,* cilt 85, pp. 1241-1246, 2002.

ANADOLU ÜNİVERSİTESİ

[178] Y. Suematsu, M. Hakuta ve e. al, Fundamental transverse electric field (TEo) mode selection for thin-film asymmetric light guides, *Appl. Phys. Lett.,* cilt 21, pp. 291-293, 1972.

[179] Y. Okamaru, S. Yamamoto ve e. al, Wave propagation in semileaky-type anisotropic thin-film optical waveguides., *J. Opt. Soc. Am.,* cilt 67, pp. 539-545, 1977.

[180] A. Agapov, A. Gorobetz ve e. al, Efficient TM-pass multilayer planar optical waveguide polarizer., *Electronics Letters,* cilt 27, pp. 1804-1805, 2012.

[181] G. N. V. D. Hoven, R. J. I. M. Koper ve e. al, Net optical gain at 1.53 μm in Er- doped Al2O3waveguides on silicon, *Appl. Phys. Lett.,* cilt 64, pp. 1886-1888, 1996.

[182] L. Agazzi, J. D. Bradley ve e. al, Monolithic integration of erbium-doped amplifiers with silicon-on-insulator waveguides., *Optics express.,* cilt 18, pp. 27703-27711, 2010.

[183] F. Wang, F. Liu ve e. al, Precision measurements for propagation properties of high-definition polymer waveguides by imaging of scattered light, *Optical Engineering,* cilt 47, no. 2, pp. 024602-1, 2008.

[184] T. A. Strasser ve M. C. Gupta, Optical loss measurement of low-loss thin-film waveguides by photographic analysis, *Applied Optics,* cilt 31, no. 12, pp. 2041-2046, 1992.

[185] J. Chen, T. Zhang ve a. et, Low-Loss Planar Optical Waveguides Fabricated From Polycarbonate, *Polymer Engineering and Science,* pp. 2015-2019, 2009.

[186] J. Ctyroky, J. Janta ve e. al, Diagnostic Methods for Planar Optical Waveguides, *Radio engineering,* cilt 3, no. 4, pp. 5-8, 1994.

[187] M. Bigas, E. Cabruja ve e. al, Review of CMOS image sensors, *Microelectronics Journal,* cilt 37, pp. 433-451, 2007.

[188] M. Hillebrand, N. Stevanovic ve e. al, High Speed Camera System Using a CMOS Image Sensor, *IEEE Intelligent Vehicles Symposium*, Dearborn, 2000.

[189] J. Prekeges, Nuclear Medicine Instrumentation, Jones & Bartlett Publishers, 2013.

ANADOLU ÜNİVERSİTESİ